Vertical-cavity surface-emitting lasers for medical diagnosis

Thor Ansbæk
PhD Thesis
August 2012

DTU Fotonik
Department of Photonics Engineering

Vertical-cavity surface-emitting lasers for medical diagnosis

PhD Dissertation

Submitted to the Department of Photonics Engineering
at The Technical University of Denmark
in partial fulfillment
for the degree of philosophiae doctor

Thor Ansbæk
2013
Kgs. Lyngby

Preface

This dissertation has been submitted to the Department of Photonics Engineering at The Technical University of Denmark (DTU) for the partial fulfillment of the degree of philosophiae doctor (ph.d.). The main supervisor has been Associate Professor Kresten Yvind. I gratefully acknowledge the PhD Scholarship funded by DTU. Part of the thesis work has been funded by the NanoNose project and the support from the Danish Agency for Science and Technology's Program Commision on Nanoscience Biotechnology and IT (NABIIT) is acknowledged.

The motivation of the work has been to combine Vertical-Cavity Surface-Emitting Lasers with Micro-Opto-Electro-Mechanical Systems in order to advance the field of Optical Coherence Tomography (OCT). It has been a highly motivating subject to work on and I would like to thank my main supervisor Kresten Yvind for giving me this opportunity and supporting my project in every manner. A cornerstone in the project has been the use of the novel High-index Contrast subwavelength Grating (HCG) and to this aim I would like to thank Il-Sug Chung for his supervision into this for me completely new field. Last but not least I would like to thank David Larsson for his supervision on the Volatile Organic Compound (VOC) sensor.

The initial part of the PhD was spent on getting acquainted with Vertical-Cavity Surface-Emitting Laser (VCSEL) processing by the fabrication of bottom emitting VCSELs. Simultaneously, experiments where done coating an off-the-shelf VCSEL with polystyrene and measurering the response to Acetone vapour. I would like to thank Claus Højgård Nielsen for doing the plasma polymerization of the polystyrene coatings and Søren Dohn for giving me access to his environmetal chamber for performing the experiments.

The second part of the PhD project has been spent on the fab-

rication of a tunable Fabry-Pérot filter with a HCG top mirror. I would like to thank Jong-Min Kim for his initial work on growing epitaxial wafers with InGaP and AlInP. In order to fabricate subwavelength gratings dry etching was a neccesity and I would like to acknowledge the efforts of Martin Schubert and Jin Liu on the GaAs dry etching using Reactive Ion Etching (RIE) and Inductively Coupled Plasma (ICP), respectively. The aim was to use the tunable filters as part of a Fourier Domain Mode-Locked (FDML) swept source and I would like to thank Sebastian Marschall for discussion on tunable filters for OCT and his help on setting up a swept laser for characterization of the filters. The main part of the characterization of the filters was done using a fiber-based transmission setup and I would like to thank Radu Malureanu for his help and guidance.

The last year of the PhD has been a race to develop a tunable VCSEL. I would like to thank Elizaveta Semenova for shedding light on the art of epitaxial growth. I greatly appreaciated the help of Nadezda Kuznetsova and Sara Ek on the micro photoluminescene setup which was instrumental in measuring non-lasing VCSELs. Thanks go to Martin Schubert for setting up the characterization setup. Silvan Schmid is thankfully acknowledged for his help with laser Doppler vibrometer measurements on the mechanical properties of the VCSELs. Ole Hansen and Erik V. Thomsen are both thanked for their supervision on the Micro-Electro-Mechanical Systems (MEMS).

Having been associated to DTU Fotonik and the adjacent DTU Nanotech for almost 7 years I have had the pleasure to work along a long list of friendly collegues and students. I have greatly appreciated the helpful environment. In particular I would like to thank Troels Suhr Skovgård, Sara Ek, Rózȧ Shirazi and Andrei Andryieuski for the cheerfull atmosphere upheld in our office - plastered with cake pictures. Lastly I would like to thank my family for their support - in particular my girl friend Benedicte Ersted Jensen who has supported me all the way and made sure that life went on as usual outside the world of research.

This thesis is dedicated to my grandmother Jutta Ursula Elisabeth Christensen.

Errata

I would like to thank the examiners for their comments on my thesis. Based on these comments the print version of the thesis has been corrected for grammar errors. Furthermore errors in the bibliography has been corrected. These technical changes are not accounted for here. This version deviates from the original version submitted in advance of the defence and published on the internet in that the format is B5 (or almost..., it is 17x24 cm) and not A4.

For the print version the following appendices has been added: B) Fabry-Perot Process Flow C) HCG-VCSEL Process Flow. The VCSEL process flow is identical to what is taught in the course 34057 Fabrication of Nanophotonic Devices and can be found elsewhere.

pp. 4 & 5[1]. The relative **repetitive** tuning range has been corrected to 2.1%.
pp. 26. "‘A reflectance above 99.9% is required..."’ has been changed to "‘A reflectance above 99.5% is required..."’.
pp. 42 Eq. (2.47). In the denominator on the right side 1 has exchanged to ω_0^2.
pp. 43 Eq. (2.49). In the denominator Q has been changed to ω_0^2.
pp. 43 Fig. 2.19. The title has been removed.

Thor Ansbæk

September 25, 2013

Supervisors:
Kresten Yvind
Il-Sug Chung
David Larsson
Department of Photonics Engineering
Technical University of Denmark
Ørsted Plads 344
2800 Kgs. Lyngby

[1]Page numbers refers to the thesis as published on the Internet

Abstract

This thesis deals with the design and fabrication of tunable Vertical-Cavity Surface-Emitting Lasers (VCSELs). The focus has been the application of tunable VCSELs in medical diagnostics, specifically OCT. VCSELs are candidates as light sources for swept-source OCT where their high sweep rate, wide sweep range and high degree of coherence enable deep probing of tissue at acquisition rates that will eliminate the effects of rapid involuntary eye movements.

The main achievement of the dissertation work has been the development of an electro-statically tunable VCSEL at 1060 nm with wide tuning range and high tuning rate. The VCSEL is highly single-mode and inherently polarization stable due to the use of a High-index Contrast subwavelength Grating (HCG). HCG VCSELs are presented with 2.1% relative tuning range at a tuning rate of 850 kHz.

The thesis reports on the analysis of narrow linewidth Fabry-Pérot filters with dissimilar mirrors and the design of such Fabry-Pérot cavities for VCSELs. Fabrication of InGaAs multiple quantum wells with GaAsP strain balancing layers is covered together with the growth and wet chemical etching of InAlP. The fabrication of the proposed Fabry-Pérot filters and VCSELs is outlined and the results on their characterization reported.

Danish Resumé

Denne afhandling omhandler design og fremstilling af overfladeemitterende vertikal kavitets lasere med variabel resonansbølgelængde. Disse lasere udvikles med henblik på brug indenfor medicinsk diagnostik, nærmere bestemt optisk kohærens tomografi. Denne type laser er oplagt som lyskilde til optisk kohærens tomografi hvor den høje repetitionsrate, brede bølgelængde tunbarhed og høje grad af kohærens muliggør dybdeafbildning af øjets lagstruktur uden tab af opløsning på grund af ufrivillige øjenbevægelser.

Hovedresultatet i afhandlingen er udviklingen af en overfladeemitterende vertikal kavitets laser ved 1060 nm hvor bølgelængden ændres hurtigt i et bredt område ved elektro-statisk kraft. Denne type laser udmærker sig endvidere ved at være monokromatisk og lineært polariseret. Denne polariseringsbestemthed er opnået ved brug af et optisk gitter med en periode mindre end lysets bølgelængde og et brydningsindeks meget højere end det omgivende materiale (luft). Med denne type laser demonstreres en relativ bølgelængdeændring på 2.1% af centerbølgelængden ved en repetitionsrate på 850 kHz.

I afhandlingen gennemgås teorien for et Fabry-Pérot optisk filter med smal optisk båndbredde hvor filterets to spejle er af forskellig type. Teorien for et Fabry-Pérot filter udvides til at gælde for overfladeemitterende lasere og de relevante designovervejelser for lasere, der kan dække et bredt spektralt område, gennemgås. Afhandlingens andet store resultat er udviklingen af fremstillingsprocessen til at lave disse Fabry-Pérot filtre og lasere med InGaAs kvantebrønde under tøjning. For at kunne danne et tomrum som muliggør ændring af bølgelængden ved elektro-statisk kraft er offeræts af InAlP undersøgt. På baggrund af de valgte designs fremstilles Fabry-Pérot optiske filtre og overfladeemitterende vertikal kavitets lasere, og deres elektro-optiske egenskaber undersøges eksperimentelt.

Contents

1 Introduction **15**
1.1 Optical coherence tomography 15
1.2 Tunable semiconductor lasers 18
1.3 State of the art 21
1.4 Thesis outline 25

2 Theory and design **27**
2.1 Fabry-Pérot etalon 27
2.2 Mirrors 29
2.2.1 Method 29
2.2.2 HCG 31
2.3 Fabry-Pérot filter 36
2.3.1 Resonance wavelength 36
2.3.2 Transmission 38
2.4 HCG-VCSEL 42
2.4.1 Lasing condition 44
2.4.2 Method 46
2.4.3 Two mirror Fabry-Pérot cavity 47
2.4.4 Three mirror Fabry-Pérot cavity 52
2.4.5 Summary 54
2.5 Electro-static actuation 56
2.5.1 Static operation 57
2.5.2 Dynamic operation 59

3 Device fabrication **63**
3.1 Epitaxial growth 63
3.1.1 InGaAs MQW 65
3.1.2 VCSEL 68
3.1.3 InAlP 70

3.2 Sacrificial release etch 72
3.2.1 General considerations 73
3.2.2 InAlP sacrificial etch 74
3.2.3 Results 75
3.3 Grating pattern transfer 77
3.3.1 Si_3N_4 mask 78
3.3.2 ZEP mask 79
3.3.3 HSQ mask 81
3.4 HCG Fabry-Pérot filter 82
3.5 VCSEL processing 82
3.6 HCG-VCSEL processing 83
3.7 Summary 85

4 Fabry-Pérot filter results 87
4.1 Transmission measurements 87
4.1.1 Fiber-based setup 88
4.1.2 Filter transmission 89
4.2 Discussion 90

5 VCSEL results 91
5.1 Experimental setup 91
5.2 VCSEL 92
5.2.1 Device structure 92
5.2.2 Laser characterization 93
5.2.3 Discussion 94
5.3 HCG VCSEL 97
5.3.1 Device structure 97
5.3.2 Laser characterization 98
5.3.3 Static wavelength tuning 101
5.3.4 Swept wavelength tuning 102
5.3.5 Mechanical characterization 104
5.3.6 Discussion 104

6 Conclusion 107

A Fabry-Pérot Interferometer 111

B Fabry-Pérot Filter Process 115

C HCG-VCSEL Process 121

Acronyms **129**

List of publications **133**

Bibliography **134**

Chapter 1

Introduction

In this chapter an introduction to the field of research and the motivating application is given. A popular account of Optical Coherence Tomography (OCT) and the use of swept sources is given in Sec. 1.1 to motivate the work. Here it is described why semiconductor lasers are interesting for swept source OCT. This is followed up in Sec. 1.2 by a short review on methods for making semiconductor based tunable lasers. We focus on a particular type of semiconductor laser, namely the VCSEL, which we argue is a good candidate light source for swept-source OCT systems. The state-of-the-art in tunable VCSELs is discussed in Sec. 1.3. The chapter ends with an outline of the thesis, covered in Sec. 1.4.

1.1 Optical coherence tomography

Light sources, covering parts of the electromagnetic spectrum, are used extensively to determine how light is reflected or absorbed by matter. Spectroscopy finds its application in various fields such as medical diagnostics, environmental sensing and material inspection. The requirements on such light sources vary widely depending on the application. In Optical Coherence Tomography (OCT) there is an expressed need for fast tunable lasers that can speed up the image acquisition rate, providing the physician with a real-time diagnostic tool. The focus of this thesis has been to investigate whether a monolithic semiconductor optical filter can provide a rapidly tunable light source covering a wide wavelength range use-

full for OCT[1].

The analysis of cross-sectional images of tissue is an important diagnostic tool within medicine. These cross-section images, or slices, show the cellular structure of the tissue and are in particular used in the diagnostics of malignant tissue. There are two distinct methods to obtains such a slice. The traditional method is by taking a biopsy[2], which is an *invasive* procedure also known as histology. In many areas *non-invasive* techniques are preferred and the use of penetrating waves for this purpose is referred to as tomography. Imaging modalities range from tomography using x-rays and visible light to ultrasound. OCT is a technique by which a depth-resolved image of the tissue is acquired with micrometer resolution using near-infrared light. This is particularly usefull in the diagnoses of eye diseases where the diagnostic tool must be *non-invasive*. The depth-resolved image is acquired by sampling the interference between two identical light beams - one reflected by a mirror, the other reflected from the tissue - in a Michelson-type interferometer. By varying the phase delay of one arm, the reflections at different depths in the tissue for which the phase delay matches can be measured. In OCT the light source must emit within the optical window (also referred to as the therapeutic window) which is the wavelength range within which the light has the largest penetration depth.

There are two major absorbing components of tissue that determine the optical window. These are hemoglobin (red blood cells, Hb) and water. Fig. 1.1 shows the absorbance of these two components together with the absorption of melanin in the retina and skin. The eye mainly consist of water, or more precisely vitreous humor, which the light must propagate through to reach the retina. Above 1300 nm light is mainly aborbed by water, while below 650 nm oxygenated and deoxygenated hemoglobin (HbO_2/Hb) absorbs the light. Hence OCT is mainly done in the wavelength range of 600-1300 nm with the current standard being 850 nm for ophthalmology and 1300 nm for dermatology. This makes direct bandgap semiconductor materials from the group III and V of the periodic table a good choice as light source. In particular III-V light sources made

[1] Rapidly refers to > 100 kHz sweep rate and widely to > 50 nm.

[2] In a biopsy a small amount of tissue is removed from the patient. This is then sliced, stained (colored) and inspected by microscopy.

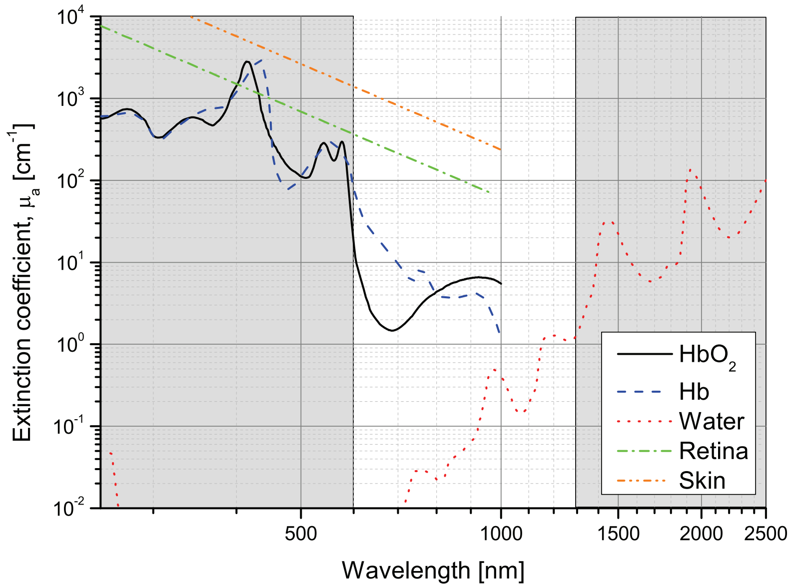

Figure 1.1: Extinction coefficient of typical tissue constituents encountered in OCT. The white region is referred to as the optical window since it is the optimum trade-off between water and blood absorption (courtesy of http://omlc.ogi.edu/spectra/).

from AlInGaAs grown on GaAs-substrates will be able to cover the full range from 850-1300 nm. Currently the dominant technology is Spectral-Domain OCT (SD-OCT) where super-luminescent diodes are used as light sources together with grating-based spectrometers for obtaining the resulting interference scan in the Fourier domain. Depending on the wavelength either complementary metal-oxide-semiconductor (CMOS) or InGaAs line scan sensors can be used with scan rates of 142 kHz and 91 kHz, respectively[3]. Within the OCT research community there is a technology push towards Swept Source OCT (SS-OCT) where a tunable light source is used together with a photodetector. It is believed that SS-OCT will improve imaging depth and speed, enabling both the anterior and

[3]The values are for the top-end models from `http://www.baslerweb.com/`Basler (CMOS) and `http://www.goodrich.com/Goodrich`Goodrich (InGaAs).

retina to be imaged at video-rate in one instrument with reduced motion artifacts [1, 2, 3]. Tunable semiconductor lasers have been attracting increasing attention within the field of OCT where they hold the promise of 3D eye scans acquisition on a time scale that will make motion artifacts negligible.

1.2 Tunable semiconductor lasers

The laser started out as a technology without a clear-cut application, but has become ubiquitous with applications ranging from surgery to DVD players. Semiconductor diode lasers offer a well-established mass-production platform as well as great diversity in wavelength span and functionality. One prominent functionality is wavelength tunability, which allows dynamic control of the emission wavelength.

In 1917 Albert Einstein introduced the concept of spontaneous and stimulated emission of radiation with energy $E_m - E_n$, from a molecule going from an higher energy state E_m to a lower energy state E_n[4]. However it was not until 40 years later when Charles H. Townes *et al.* published their article on the theory of the Microwave Amplification by Stimulated Emission of Radiation (maser), with the idea of applying feedback to the amplifcation of radiation, that the the field took off [5]. Simultaneously with Townes, Gordon Gould had sketched his ideas on the Light Amplification by Stimulated Emission of Radiation (laser) in his laboratory notebook [6]. Gordon Gould recognized that a Fabry-Pérot interferometer could be used to provide the feedback of the stimulated emission required for lasing. Shortly thereafter, the semiconductor diode laser was demonstrated for both GaAs and GaAsP semiconductor diodes [7, 8]. The present work relates directly to this effort - with the research field having moved to more advanced electro-optical design made possible by continuing improvements in fabrication technology. With the advent of broadband internet and semiconductor lasers during the late 90's there has been a great deal of both commercial and scientific interest in advancing the field of telecommunication. Optical fibers based on silicon oxide have largely replaced traditional copper wires as they enable longer transmission distances and transmission of multiple signals by Wavelength Di-

vision Multiplexing (WDM). Using wavelength multiplexing the electronic data are encoded at different wavelengths all carried by a single fiber. This provides a straight-forward route of expanding the capacity of fiber optic networks. Instead of needing one laser assigned to each wavelength, a significant cost advantage and flexibility could be achieved by using a tunable laser that could dynamically address different wavelengths. A great deal of commercial effort was put into developing such light sources in the years preceeding the dot-com bubble in 2000.

The laser consists of an optical gain medium with feedback provided by an optical resonator. The optical resonator, known as the Fabry-Pérot interferometer, consists of two opposing mirrors. The cavity mode for such an interferometer is given by [9]

$$\lambda_m = \frac{2nL}{m}, m \in \mathbb{N}^* \tag{1.1}$$

where m is the mode number, n the refractive index of the cavity and L the cavity length. The longitudinal lasing mode(s) are determined by Eq. (1.1) together with the gain and mirror reflectance spectrum. Lasing occurs at the modes for which the gain exceeds the mirror and cavity loss. From Eq. (1.1) it follows that tuning can be achieved by changing the refractive index of the cavity (n), the cavity length (L) or the lasing mode (m).

The technological implementation of tunable semiconductor lasers mainly falls into three categories, namely the:

- External Cavity Laser (ECL).
- Edge-emitting Distributed Bragg Reflector (DBR) laser.
- VCSEL.

Tunable external cavity lasers are widely used as this implementation offer great flexibility, exploit the full gain spectrum of the Semiconductor Optical Amplifier (SOA) and can make use of multiple optical components for wavelength selective feedback. The majority of widely tunable ECLs are either of the Littrow, Littmann-Metcalf or Fabry-Pérot configuration. The advantage of the ECL is that high single-mode output powers can be achieved together with a wide tuning range, only limited by the gain medium [10].

In both the Littrow and Littman-Metcalf configuration a diffraction grating is used as the wavelength selective feedback to the SOA. The weak link in the Littrow and Littman-Metcalf configurations is the electro-mechanical tuning of the bulky diffraction grating and reflector, respectively. Miniaturization of the diffraction grating and reflector has been researched, but the tuning rate is still limited to kHz from size constraints [11, 12]. Using the fast angular rotation of polygon scanners to control the incident angle onto the grating in a Littrow configuration tuning rates up to 50 kHz have been shown [13, 14]. In the Fabry-Pérot configuration a Fabry-Pérot filter is used for wavelength selection, suppressing all other nearby wavelengths. Wide and rapid tuning can be achieved by Micro-Electro-Mechanical Systems (MEMS) Fabry-Pérot filters. Kuznetsov *et al.* have demonstrated 10% relative tuning at 100 kHz using the MEMS Fabry-Pérot filter as reflector [15].

Tunable edge-emitting DBR lasers were originally developed to target telecommunications. For Sampled Grating DBR (SGDBR) wavelength tuning is achieved by tuning the reflection spectrum of the two cavity mirrors to coincide while tuning a phase section to match the propagation phase. Wide discontinuous wavelength tuning can be achieved with the added benefit that a SOA can be monolithically integrated to boost the power output. Recently DBR lasers have been proposed for SS-OCT by Insight Photonic Solutions which has achieved 100 nm tuning range at 200 kHz [16]. Fast Digital Signal Processing (DSP) are required in order to control the four electrodes of the laser diode that are controlling the wavelength tunability [17, 18]. The DSP must control the input currents according to a look-up-table that must be acquired by full calibration. Long-term drift in such devices is likely to lead to over-lapping wavelength scans and artifacts in OCT.

Tunable VCSELs are favoured for commercial use due to the ability to conduct wafer-level testing, which leads to significant cost-reduction during packaging. Tunable VCSELs will be reviewed in the following section. In the tunable VCSEL it is the Fabry-Pérot cavity length that is directly modulated. Due to their small size VCSELs allow tunability in the MHz range [19]. The power output is lower than tunable SGDBR lasers and ECLs for electrically pumped versions. Praevium Research has demonstrated a tunable optically pumped VCSEL with 100 nm tuning range at 1310 with

tuning rates of 500 kHz [20]. While optically pumped VCSELs allows greater output power, their packaging is complicated by the requirement of an external laser diode.

Widely tunable semiconductor lasers were originally developed for WDM systems in telecommunication, but recently focus has shifted toward other applications such as gas-sensing and medical imaging. In particular within SS-OCT there is an on-going race to establish tunable semiconductor lasers as the dominant technology. Emphasis has been put on external cavity lasers by companies such as Axsun, Santec, Exalos and Micron Optics - the best results showing 100 nm tuning range at hundreds of kHz. The competitors Thorlabs and Insigth Photonic Solutions are focusing on optically pumped VCSELs and SGDBR lasers, respectively.

1.3 State of the art

Tunable VCSELs have been researched for more than two decades. The vertical-cavity optical design lends itself to a straight-forward implementation of mechanical tuning from a conceptual point of view. From Eq. (1.1) it follows that incorporating a variable air-gap as part of the cavity L the cavity-mode can be directly modulated. The idea to form a variable air-gap in a semicondutor device by sacrificial etching was already introduced in 1967 when Nathanson *et al.* presented the fabrication of resonant gate transistors [21]. In 1979 the first VCSEL was introduced by Ivars Melngailis and the research group of Kenichi Iga continued to present the first Continous Wave (CW) operation at room temperature in 1989 with mW output power and 35 dB Side-Mode Suppression Ratio (SMSR) [22, 23, 24]. Less than a decade later, in 1995, the first electro-mechanically tunable VCSEL was introduced, demonstrating 10 nm tuning range [25]. The tuning range was improved shortly after by a factor of two, achieving a 2% relative tuning range at kHz frequencies [26, 27]. In recent years even better results have been shown - approaching the limitation from the wide free-spectral range of VCSELs. Gierl *et al.* have demonstrated 6.6% relative tuning range at DC thermal large-signal tuning [28]. Zhou *et al.* have demonstrated MHz electro-static small-signal tuning with relative tuning ranges below 0.5% [29]. Currently the state-of-the-art

within VCSELs, both rapidly and widely tunable, are hundreds of kHz with 3% relative tuning range at 1550 nm [30, 31]. Table 1.1 provides a summary of notable achievements of tunable VCSELs in chronological order. Currently tunable VCSELs at 750, 850, 980 and 1550 nm have been presented covering the tuning schemes of electro-static, piezo-electric and thermal (bimorph) actuation.

Year	QW	λ_0 [nm]	$\frac{\Delta\lambda}{\lambda_0}$ [%]	SMSR [dB]	$P_{\max}$ [mW]	f_0 [kHz]	Type	Ref. *et al.*
1997	InGaAs	980	1.2	30	0.150	300	E	Vail [26]
1997	InGaAs	970	2.0	24	0.002	(500)	E	Sugihwo[27]
2004	AlGaInAs	1550	2.6	32	0.100	DC	T	Riemenschneider [32]
2007	GaAs	850	0.4	40	1.200	20	P	Huang [33]
2008	AlGaAs	750	3.0	MM	0.012	700	E	Cole [34]
2008	GaAs	850	0.4	45	2.000	3000	E	Zhou [29]
2009	AlGaInAs	1550	2.6	60	3.500	350	E	Yano [30]
2010	GaAs	850	2.2	40	0.170	DC	E	Davani[35]
2011	AlGaInAs	1550	5.6	45	3.500	DC	T	Gierl [28]
2011	AlGaInAs	1550	3.0	40	1.800	215	E	Gierl [31]

Table 1.1: Summary of the research within tunable electrically-pumped VCSELs, λ_0 is the center wavelength, $\Lambda\lambda$ is the dynamic bandwidth, SMSR is the single-mode suppresion ratio, $P_{\max}$ is the maximum power and f_0 the resonance frequency. Different actuation methods have been used; E = electro-static actuation, T = thermal (bimorph) actuation and P = piezo-electric actuation. Further MM = multi-mode lasing and DC = direct-current modulation.

The fabrication of high-performance tunable VCSELs remains a challenge in the regard that both process development, cavity electro-optical design and the mechanical actuation must be optimized together. The best result to date have been presented by Gierl *et al.* who have used the optimized long-wavelength epitaxial structure of Amann *et al.* together with a micromachined electromechanical DBR top mirror to achieve 40 nm tuning range at 215 kHz [31]. The distinct advantage of the optical design of Gierl *et al.* is the highly stable single-mode plano-concave Fabry-Pérot cavity and high-index contrast DBRs. The high-index contrast DBRs provide the wide-band ultra-high reflectance ($> 99.9\%$) needed for lasing. Promising result have also been shown by Huang *et al.* who have demonstrated MHz tuning rates by using a HCG top mirror. The distinct advantage of the optical design of Huang *et al.* is their use of the highly single-mode and polarization stable HCG. Through careful design and fabrication the HCG mirror provides wide-band ultra-high reflectance. Figure 1.2 shows a comparison between tunable VCSELs, ECLs and DBR laser diodes with regard to output power, tuning rate and range. The ECLs and DBR lasers outperform the VCSELs in terms of output power and tuning range. This is at the expense of complicated packaging for the ECLs and the need for DSP for control of the DBR laser. VCSELs are currently unique in realizing MHz tuning rates. There is still room for significant improvement in the relative tuning range and the power output can be boosted using SOAs.

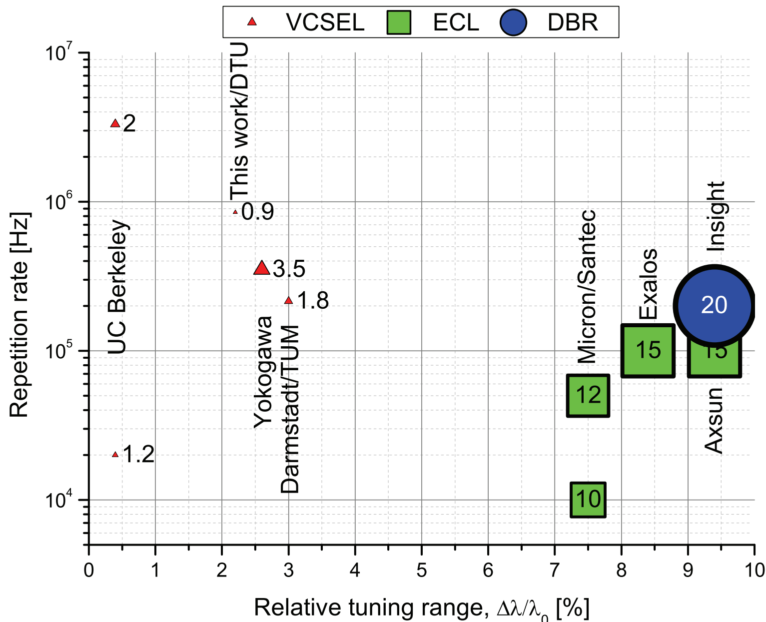

Figure 1.2: Bubble plot of the state-of-the art within tunable semiconductor lasers (VCSELs = red triangle, ECLs = green square, DBR = blue circle). The plot shows the mechanical resonance frequency versus the relative tuning range (the data label is maximum output power in mW). Data are taken from Tab. 1.1.

1.4 Thesis outline

Tunable semiconductor lasers continue to be of research interest throughout the world due to their favorable cost-structure and high performance-to-size ratio. The focus of the thesis has been to make a widely and rapidly tunable electrically-pumped 1060 nm VCSEL. We have targeted $>$ 50 nm tunability at MHz scan rates. Towards this aim ultra-high reflectivity mirrors have been fabricated in the form of DBRs and HCGs. Furthermore the epitaxial growth of optical gain material for the 1060 nm wavelength has been developed.

Chapter 2 covers the analytical and numerical framework established for the design of Fabry-Pérot filters and VCSELs with HCG and DBR reflectors. Design rules for high finesse Fabry-Pérot filters are presented based on the application of an effective mirror

model [36]. The influence of the mirror reflectance on the filter linewidth and transmission is discussed in the context of high finesse filters. Furthermore the optical cavity design of VCSELs is discussed with emphasis being put on how to increase the tuning efficiency of the VCSEL by reducing the cavity length and introducing an anti-reflective coating to the air-semiconductor interface to reduce the parasitic reflection. Lastly the electro-mechanical design of the suspended top mirror is discussed and the inherent trade-off in achieving both high scanning speed and wide wavelength tunability is presented. Both relate to the use of electro-static tuning.

Chapter 3 goes through the process development that has been necessary to fabricate HCG VCSELs. The major contribution to the research field lies in the demonstration of a possible route to realize the monolithic integration of an anti-reflective coating into the epitaxial structure. To that aim the use of InAlP for sacrificial release has been investigated for the first time.

Chap. 4 presents the results on a HCG Fabry-Pérot filter made in the GaAs material system. Chap. 5 shows the first demonstration of a VCSEL with an air-cladded HCG mirror substituted for the top p-DBR. The performance is presented in terms of the light-current-voltage characteristics and the optical spectrum.

Chapter 2

Theory and design

In this chapter the optical and electro-mechanical design of Fabry-Pérot filters and VCSELs is covered. The focus is on the Fabry-Pérot resonance effect, the threshold for lasing and the electro-static tuning of the cavity length. In Sec. 2.1 the key metric of the Fabry-Pérot etalon is briefly revisisted as this forms the basis for monochromaticity. In Sec. 2.2 the reflection properties of the High-index Contrast subwavelength Grating (HCG) is investigated. In Sec. 2.3 the design of Fabry-Pérot interferometers made up of dissimilar reflectors is analyzed and it is shown how a difference in reflectance is detrimental to the properties of the interferometer. Section 2.4 gives a walkthrough of the optical cavity design for VCSELs that have been fabricated with attention to achieving high tuning efficiency. Section 2.5 deals with the design of the Micro-Electro-Mechanical Systems (MEMS) for electro-static actuation.

2.1 Fabry-Pérot etalon

The Fabry-Pérot etalon is an example of an optical resonator. The etalon is a plate of fixed thickness L with index of refraction n (the surrounding medium has index of refraction n_0). For a normal incidence beam of light the transmission spectrum has a maximum at the wavelength [9]

$$\lambda_m = \frac{2nL}{m}, m \in \mathbb{N}^* \tag{2.1}$$

with a finesse

$$\mathcal{F} = \frac{\text{FSR}}{\text{FWHM}} = \frac{\pi\sqrt{R}}{1-R} \tag{2.2}$$

where R is the power reflectance of the two mirrors making up the optical resonator. The finesse is the ratio of distance to the neighbouring peaks, the Free Spectral Range (FSR), to the Full-Width at Half-Maximum (FWHM). Hence the higher the finesse, the better the Fabry-Pérot etalon is at picking out a particular wavelength. The distance between each peak, the FSR, can be derived to be

$$\Delta\lambda = \lambda_m - \lambda_{m+1} = \frac{\lambda_m^2}{2Ln_g} \tag{2.3}$$

where n_g is the group index

$$\frac{1}{n_g} = \frac{1}{n}\left(1 - \frac{\lambda_m}{n}\frac{\partial n}{\partial \lambda_m}\right)^{-1} \tag{2.4}$$

The group index can be taken to be n when the wavelength dependence of the refractive index is negligible.

An example of an etalon is a GaAs wafer. For a 350 μm thick GaAs etalon the FSR is 0.45 nm at $\lambda = 1060$ nm. The field reflection coefficient at the semiconductor-air interface will be

$$r = \frac{n_2 - n_1}{n_2 + n_1} = \frac{3.5-1}{3.5+1} = 0.55 \tag{2.5}$$

and hence the power reflectance will be 31%. This is enough that modulation in the transmission spectrum can show up, which is commonly referred to as Fabry-Pérot fringes. The finesse of such a cavity is only 2.5 which means that the FWHM is comparable to the FSR.

The two reflecting surfaces of the etalon can also be exchanged with two highly reflecting mirrors. The resulting Fabry-Pérot interferometer can be made tunable by changing the distance between the two mirrors. The focus here will be on monolithic vertical-cavity Fabry-Pérot interferometers. For an electro-statically tunable interferometer to require reasonable tuning voltage and at the same time have a very high mechanical resonance-frequency the cavity length must be small. For a $\lambda/2$-cavity the FSR will be the same as the interferometer wavelength and thus a high finesse is required to have a narrow FWHM. It follows from Eq. (2.2) that the mirrors must have an ultra-high reflectance, R.

2.2 Mirrors

The high finesse Fabry-Pérot filter and the VCSEL have in common the requirement of high reflectance mirrors. Metal mirrors can provide very high reflectance on the order of 98-99 % over a broad range. In fact the first demonstrations of the VCSEL was made using Au reflectors [22, 23]. High reflectance mirrors can also be fashioned by depositing a number N of $\frac{\lambda_0}{4n_L}/\frac{\lambda_0}{4n_H}$ thin film pairs of different low and high refractive index n_L and n_H. DBRs are an embodiment of such high reflectance mirrors and are either deposited dielectric mirrors or epitaxially grown semiconductor mirrors. For the first demonstration of room-temperature lasing of a VCSEL a 5-pair SiO_2/TiO_2 stack was used as the output mirror, having a reflectance maximum of 99.2%. It was early recognized that a very high reflectance, as well as large gain to cavity length ratio, was necessary in order to reduce the threshold current [37]. The AlGaAs/GaAs mirror pair has proven an ideal high-reflectance mirror for VCSELs. The lattice-matching of AlGaAs to GaAs enables very thick atomically abrupt layers to be grown making high quality mirrors of reflectance above 99.5%. Increasing the number of mirror pairs beyond 25 99.9 % reflectivity is routinely obtained only limited by free-carrier absorption. An advantage of the AlGaAs/GaAs DBR is that the reflectivity is easily scalable and that the stopband is well-behaved.

Recently a new class of broadband ultra-high reflectance mirrors has been demonstrated, the HCG [38]. These results expand on the narrowband ultra-high reflectance grating mirrors that was presented under the term of Guided-Mode Resonance (GMR) [39]. Another embodiment of essentially the same structure, the GIant Reflectivity to zero Order (GIRO) grating, was shown to have broadband high-reflectivity[40, 41, 42]. Figure 2.2 shows the reflectance of both a DBR and HCG mirror.

2.2.1 Method

In order to design the mirrors a method to calculate their reflectance, in terms of geometrical and physical properties, is needed. The reflectance of a multi-layer film such as the DBR is conveniently calculated using the Transmission Matrix Method (TMM). For re-

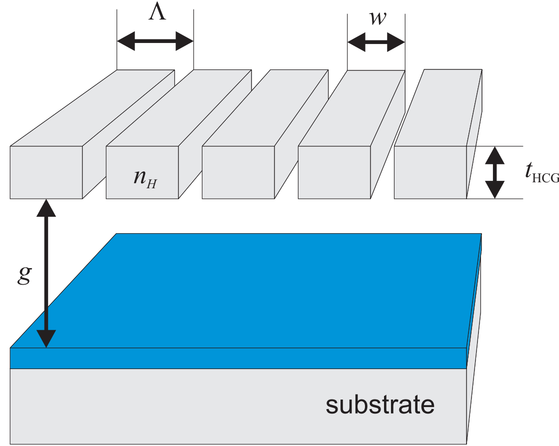

Figure 2.1: Schematic drawing of the HCG with grating period Λ, thickness t_{HCG} and duty cycle $DC = \frac{w}{\Lambda}$ given by the width, w of the high refractive index, n_{HCG}, medium. The high refractive index region is surrounded by air and space the length g above the substrate.

flectance at normal incidence the electric field and magnetic flux density[1] at the input plane (E_1 and B_1) and output plane (E_2 and B_2) of a thin film can be expressed as

$$\begin{bmatrix} E_1 \\ B_1 \end{bmatrix} = \underbrace{\begin{bmatrix} \cos(\delta/2) & \frac{i\sin(\delta/2)}{n\sqrt{\epsilon_0\mu_0}} \\ in\sqrt{\epsilon_0\mu_0}\sin(\delta/2) & \cos(\delta/2) \end{bmatrix}}_{\mathbf{M_{12}}} \begin{bmatrix} E_2 \\ B_2 \end{bmatrix} \tag{2.6}$$

where n is the thin film refractive index and δ the phase difference between a round-trip of the thin film

$$\delta = \frac{4\pi n t}{\lambda} \tag{2.7}$$

having a thickness t[43]. For a multi-layer film the transmission matrix of each layer is then multiplied to get the transmission matrix for the full stack.
The reflectance of a subwavelength grating, such as the HCG, is calculated using Rigorously Coupled Wave Analysis (RCWA)[44]. This method enables the computation of the transmittance and reflectance of a thin film with a periodic refractive index modulation.

[1]Since there is not magnetic media the magnetic flux density is related to the magnetic field by the magnetic permeability in vacuum

The HCG is an example of an ideal binary modulation. The periodic refractive index modulation of the grating and the resulting periodic modulation of the electric and magnetic field is presented through a Fourier series of order N. Applying Maxwell's equations and boundary conditions to the electric and magnetic fields inside and outside the grating, a system of coupled equations results. Here the implementation of RCWA named RODIS has been used for the calculation of the HCG reflectance [45]. Convergence analysis using RODIS for calculating the reflectance of a HCG shows that $N \geq 30$ to achieve an error in the reflectance lower than 5×10^{-4}. A thorough analytical treatment of the HCG shows that the ultra-high reflectance comes from the suppression of higher order diffraction modes and the cancellation of the two first modes [46].

2.2.2 HCG

The HCG enables ultra-high reflectivities $> 99.9\%$ by surrounding a sub-micron thick, high-refractive index material grating layer with a low-refractive index material [19, 38]. The use of broadband HCGs has so far been limited to coupled cavity design where it has been used to increase the reflection of a low-Q cavity consisting of 2-4 pairs of top DBRs and 34 pairs of bottom DBRs [47, 48]. The only demonstration of a VCSEL with a HCG as top reflector has been done at 1330 nm using a Si/SiO_2 HCG with 9 mA threshold current at 15°C [49].

The HCG only requires a single high-refractive index layer surrounded by low-refractive index material. This makes it markedly easier to fabricate than a similar approach to DBRs of increasing the refractive index contrast which requires several layers of dissimilar materials [50, 51, 52]. While the DBR requires the control of only two parameters, the optical thicknesses of the two layers, the HCG requires the control of three parameters, the grating thickness t_{HCG}, the period P and duty cycle Λ. From the carefull design of these parameters a photonic stopband similar to, or even exceeding, the high refractive index contrast DBR can be obtained. The HCG has the added advantage that when designed using grating bars (1D) strong polarization dependence can be achieved. Figure 2.2 shows the design employed throughout this thesis for $\lambda_0 = 1060$ nm, which was calculated using RODIS. This HCG design shows

broadband reflectivity for the TM mode, with the electric field perpendicular to the grating. This is an advantage when SOAs are to be used to boost the output power - with improper control of the polarization the power penalty can be up to 10 dB. In order to

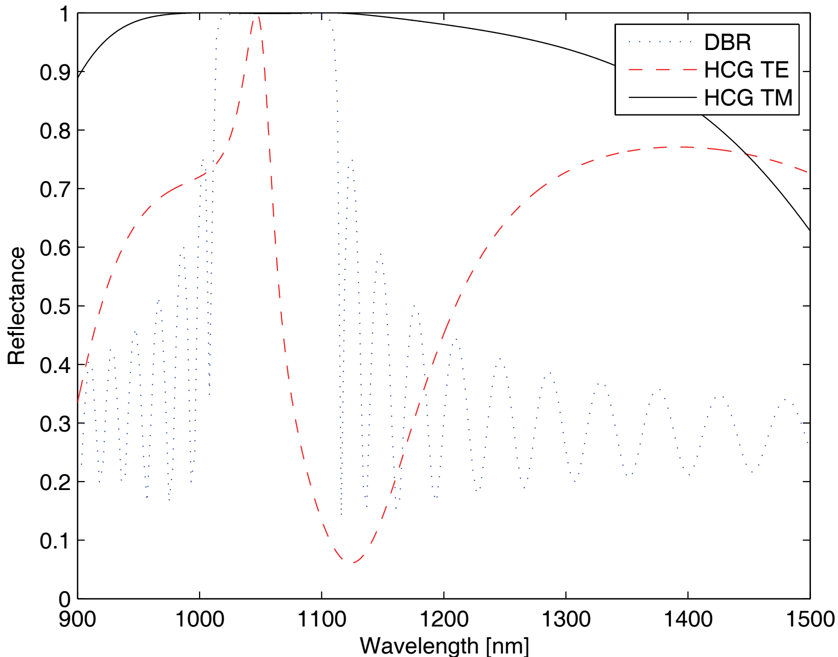

Figure 2.2: Plot of the reflectance of a 35 pair $Al_{0.9}Ga_{0.1}As/GaAs$ DBR (dotted) and HCG with $DC = 0.72$, $\Lambda = 460$ nm, $t_{\text{HCG}} = 280$ nm and $n_{\text{HCG}} = 3.5$. The reflectance for the HCG is plotted for both TE (dashed) and TM (solid) polarized light.

achieve very high HCG reflectance the grating period must be subwavelength in order to suppress all higher order diffraction modes other than the zeroth diffraction mode [46, 53]. This is because the ultra-high reflectivity effect depends on the destructive interference of the waveguide modes at the output plane of the HCG. The conditions for such cancellation in terms of the geometry can be found to be $DC = 0.7$ and $t_{\text{HCG}} = 300$ nm and $\Lambda = 500$ nm for $n = 3.21$ [46]. Here all computations are done with $n = 3.5$.

Figure 2.3 shows a 3D plot of the grating designs that yield an ultra-high reflectivity stopband of 40 nm around a center wave-

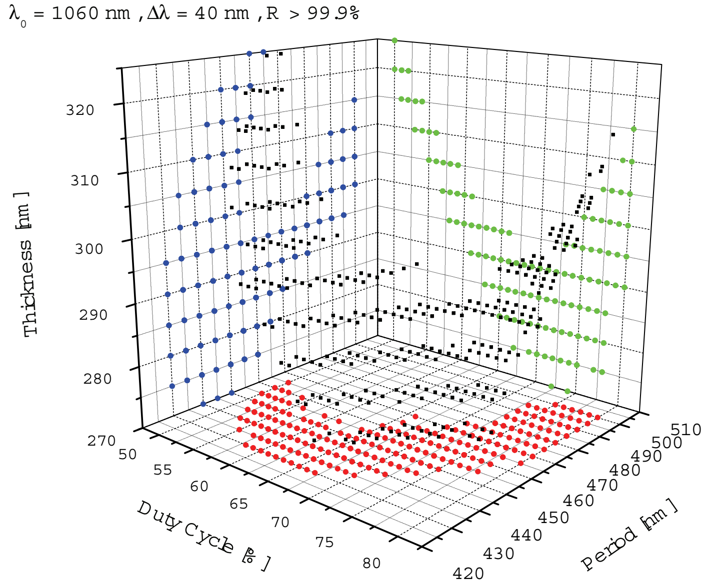

Figure 2.3: 3D plot of the combinations of grating thickness t_{HCG}, duty cycle DC and grating period Λ required for a 40 nm photonic stopband with $R > 99.9\%$. The refractive index of the grating is $n_{\text{HCG}} = 3.5$.

length of $\lambda_0 = 1060$ nm. In order to match the bottom DBR reflectance of the VCSEL with the top HCG we haven chosen a design with $t_{\text{HCG}} = 280$ nm, $DC = 0.72$ and $\Lambda = 460$ nm. This particular design has a local reflectance minimum of 99.9% at $\lambda_0 = 1060$ nm. The increasing reflectivity away from the center wavelength λ_0 then compensates the decreasing reflectivity of the DBR which has a maximum reflection coefficient at λ_0.

Since the ultra-high reflectivity effect of the HCG depends on the destructive interference of two modes the grating thickness, and thus propagating phase, become a key parameter. Fig. 2.4 shows a contour plot of the GaAs HCG reflectance versus wavelength and grating thickness. From Fig. 2.4 it is seen that in order to achieve a broadband reflectivity of 99.5% or higher the grating thickness must be close to 275 nm. Epitaxial growth of GaAs enables precise control of the grating thickness, t_{HCG}, to within ± 5 nm, and hence this is not out of reach. The period is well-controlled by e-beam

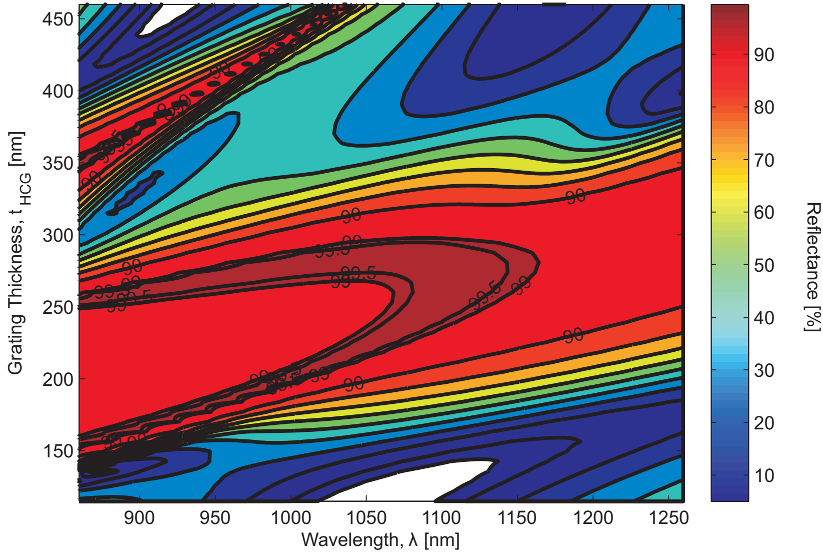

Figure 2.4: Contour plot of the HCG reflectance versus wavelength and grating thickness. The refractive index of the grating is $n_{\text{HCG}} = 3.5$, duty cycle $DC = 0.72$ and period $\Lambda = 460$nm.

writing, while the duty cycle depends on the control of the e-beam exposure, development and pattern transfer.

Figure 2.5 shows a contour plot of the GaAs HCG reflectivity at a wavelength of 1060 nm versus the grating thickness, t_{HCG}, and the duty cycle DC. At a grating thickness of 280 nm the reflectivity stays above 99.5% for at duty cycle of 0.7-0.85. This corresponds to a difference in the grating bar width of 70 nm at the given grating period of 460 nm. Hence the HCG reflectance is not very sensitive to the grating duty cycle. However, the HCG reflectance is not the only parameter changing with the duty cycle, the HCG reflection phase θ will also change. For the DBR it is very convenient that the reflection phase is zero at the Bragg frequency, but the HCG reflection phase is generally non-zero at the design resonance wavelength which must be accounted for in the epitaxial design. Figure 2.6 shows a contour plot of the GaAs HCG phase versus grating thickness, t_{HCG}, and duty cycle, DC.

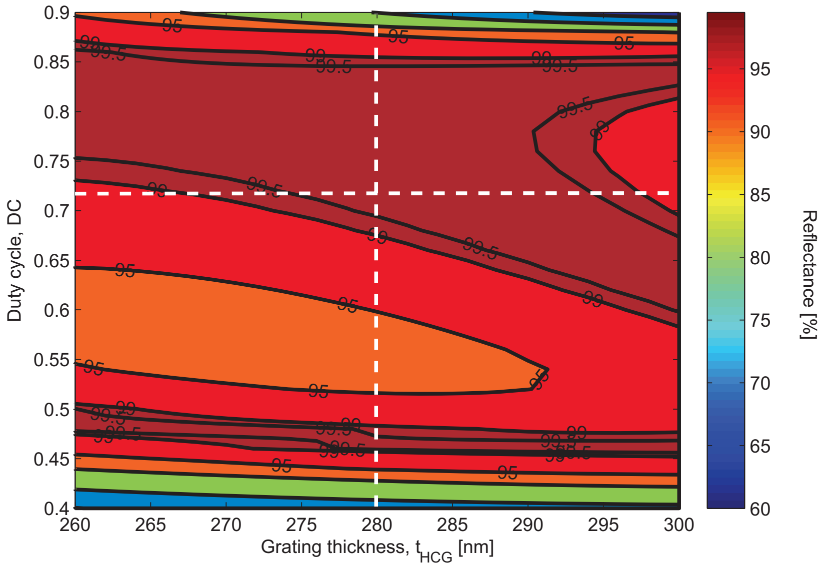

Figure 2.5: Contour plot of the HCG reflectance at $\lambda_0 = 1060$ nm versus the grating thickness, t_{HCG}, and duty cycle, DC.

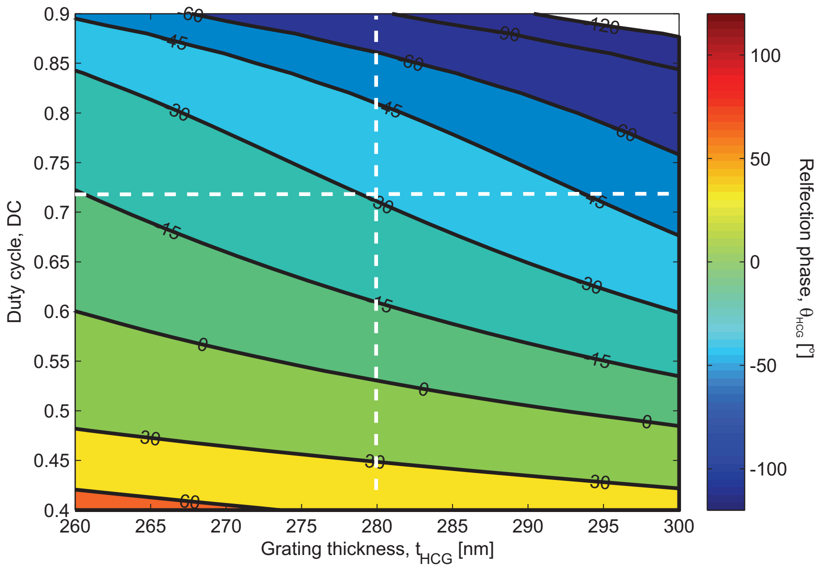

Figure 2.6: Contour plot of the HCG reflection phase θ_{HCG} at $\lambda_0 = 1060$ nm versus the grating thickness, t_{HCG}, and duty cycle, DC.

2.3 Fabry-Pérot filter

The two preceeding Secs 2.1 and 2.2 treated the Fabry-Pérot etalon and two types of reflectors, namely the DBR and HCG. Here we combine the two in what is the Fabry-Pérot interferometer seen in Fig. 2.7. Here the DBR is the bottom mirror, which is grown epitaxially on the substrate, and the HCG is the top mirror, which is patterned by surface micro-machining. From Eq. (2.1) we may conclude that the wavelength change is twice the change in gap distance for a interferometer with fundamental cavity $m = 1$, but the penetration depth of the mirrors will make the achievable wavelength change smaller.

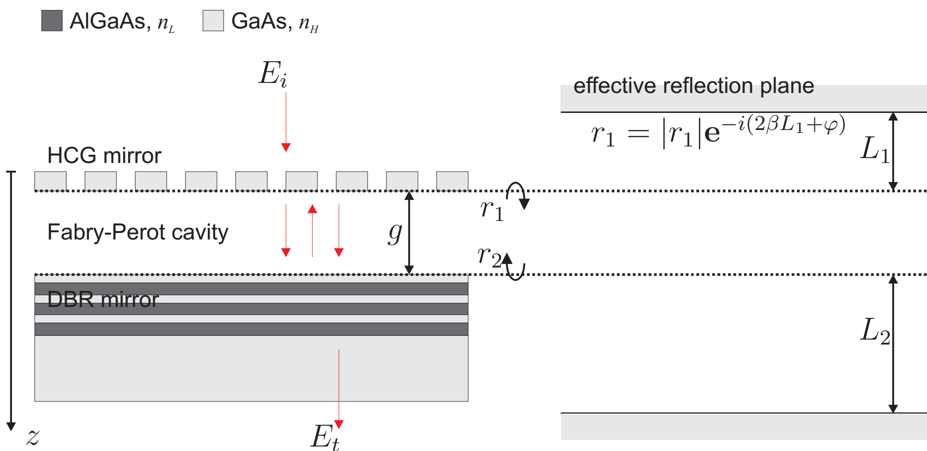

Figure 2.7: Filter schematic (left) and model (right). The filter consist of a bottom distributed bragg reflector (DBR) and a top high-index-contrast subwavelength grating (HCG). In the model the mirrors are represented by hard mirrors with a reflectance $|r|^2$ at a distance L and phase-shift φ from the physical reflection plane.

2.3.1 Resonance wavelength

The mirrors of the cavity will be characterized by their reflection coefficient and reflection phase (which for the DBR is zero at the Bragg frequency). The reflection phase can be approximated to be linearly dependent on the wavelength and can hence be linearized

around the center wavelength λ_0 [36, 54, 55]

$$\begin{aligned}
\theta(\lambda) &= \frac{\partial\theta}{\partial\lambda}\frac{\partial\lambda}{\partial\omega}\bigg|_{\omega_0}\left(\frac{2\pi c}{\lambda}-\frac{2\pi c}{\lambda_0}\right)+\theta(\lambda_0) \\
&= -\tau\left(\frac{2\pi c}{\lambda}-\frac{2\pi c}{\lambda_0}\right)+\theta(\lambda_0) \\
&= -\frac{4\pi n_g L_{\text{eff}}}{\lambda}+\varphi
\end{aligned} \tag{2.8}$$

where we have defined the reflection phase delay $(\partial\theta/\partial\omega)$

$$\tau \equiv -\frac{\partial\theta}{\partial\lambda}\frac{\partial\lambda}{\partial\omega}\bigg|_{\omega_0} = \frac{\partial\theta}{\partial\lambda}\bigg|_{\lambda_0} \times \frac{\lambda_0^2}{2\pi c}, \tag{2.9}$$

penetration depth

$$L_{\text{eff}} \equiv v_g\tau = \frac{c\tau}{2n_g} \tag{2.10}$$

and constant reflection phase delay

$$\varphi \equiv \frac{2\pi c\tau}{\lambda_0}+\theta(\lambda_0) = \frac{4\pi n}{\lambda_0}L+\theta(\lambda_0). \tag{2.11}$$

This allows us to rewrite the resonance condition as

$$\lambda_m = \frac{4\pi(n_0 g + nL_1 + nL_2)}{2\pi m + \varphi_1 + \varphi_2}, \tag{2.12}$$

where n_0 is the refractive index of the gap medium, g the gap distance and nL is the optical penetration depth of the mirrors of indices 1 and 2. The refractive index is that of the medium into which the light is reflected from the physical mirror. The effective mirror model provides the interpretation that the actual mirror can be replaced by a hard mirror at a distance L_{eff} from the physical mirror position with a constant reflection phase that is independent of the wavelength, as illustrated in Fig 2.7. The tuning efficiency of the interferometer is

$$\frac{\partial\lambda_m}{\partial g} = \frac{4\pi}{2\pi m + \varphi_1 + \varphi_2}. \tag{2.13}$$

For the HCG and DBR in Fig. 2.2 $\varphi_1 = 2.04\pi$, $\varphi_2 = 6.69\pi$, $nL_1 = 583$ nm and $nL_2 = 1770$ nm. Then the tuning efficiency as calculated for a fundamental mode cavity ($m = 1$) using Eq. (2.13) is 0.37.

2.3.2 Transmission

The transmission loss and the finesse $\mathcal{F}$ are the most important parameters of a filter. The transmission is unity at the filter resonance wavelength in the simple model of Eq. (2.12), but absorption loss and difference in the reflectance of the two mirrors will both result in reduced transmission. For application in WDM a finesse of $\mathcal{F} > 200$ is required, which corresponds to a FWHM of around 0.5 nm [56]. For application in OCT an even higher finesse of $\mathcal{F} > 400$ is required, which corresponds to a FWHM of around 0.15 nm at a center wavelength of 1060 nm. The transmission loss should be less than 3 dB. The transmission can be written (see App. A)

$$T_{FP} = \frac{|t_1|^2|t_2|^2}{(1-|r_1||r_2|)^2 + 4|r_1||r_2|\sin^2(\delta'/2)} \tag{2.14}$$

where t and r are the fresnel transmission and reflection coefficients, respectively, and δ' the phase difference after a round-trip.

Loss-less

The simplest case arise for the interferometer where there is no absorption loss, beam walk-off and the reflection phases are zero. With $R = |r_1||r_2|$ the filter transmission, using Eq. (2.14), becomes

$$\begin{aligned} T_{FP} &= \frac{(1-R)^2}{(1-R)^2 + 4R\sin^2(\delta/2)} \\ &= \frac{1}{1+F\sin^2(\delta/2)} \end{aligned} \tag{2.15}$$

where F is referred to as the coefficient of finesse. From Eq. (2.15) the FWHM can be derived

$$\begin{aligned} T_{FP}(\delta_0 \pm \Delta\delta) &= \frac{1}{2}T(\delta_0) \Rightarrow \\ \Delta\lambda_{\mathrm{FWHM}} &= \frac{\lambda^2}{2\pi n_0 g}\frac{1}{\sqrt{F}} \end{aligned} \tag{2.16}$$

The FWHM is an important parameter of the filter and is contained in the expression for the finesse, Eq. (2.2). From Eq. (2.16) it can be concluded that to decrease the filter linewidth the coefficient of finesse should be increased. In Fig. 2.8 the linewidth as calculated

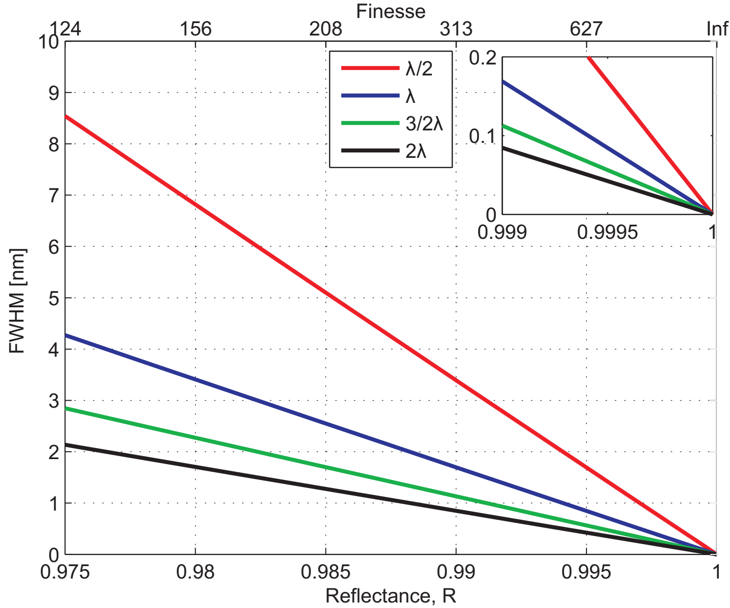

Figure 2.8: Plot of the linewidth as function of the mirror reflectance for different cavity lengths.

from Eq. (2.16) is plotted for different values of the reflectance R. A reflectance above 99.9% is required for the FWHM to be smaller than 0.1 nm for a λ-cavity.

Unequal reflectance

In a typical bulk type etalon the reflectivity of the two mirrors will be the same. Equal mirror reflectance will be more difficult to achieve when the mirrors are of different types. To take into account the difference in reflectivity we can expand Eq. (2.14)

$$T_{FP} = \frac{T_1 T_2}{(1-|r_1||r_2|)^2} \frac{(1-|r_1||r_2|)^2}{(1-|r_1||r_2|)^2 + 4|r_1||r_2|\sin^2(\delta'/2)} \tag{2.17}$$

where the second fraction is the the same as Eq. (2.14) with $R = |r_1||r_2|$ and the first fraction is a pre-factor that determines the effect of the mismatch of the two mirrors. This prefactor can be rewritten as

$$T_{12} = \frac{(1-|r_1|^2)(1-|r_2|^2)}{(1-|r_1||r_2|)^2} \tag{2.18}$$

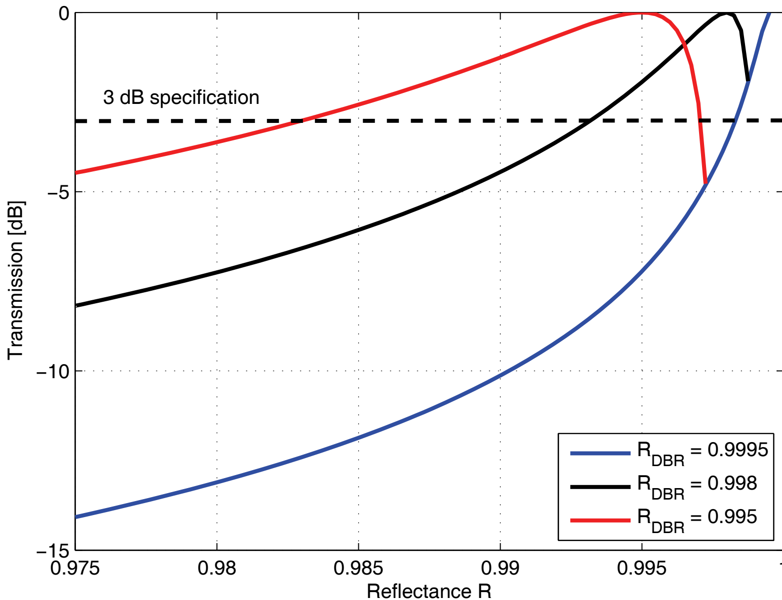

Figure 2.9: Plot of the mismatch pre-factor T_{12} as a function of the Reflectance $R = |r_1||r_2|$ for three different DBR Reflectances $R_2 = 99.5\%$, 99.8% and 99.95%.

where we again assume the lossless case $T = 1 - R$ for both mirrors. This function is one for $r_1 = r_2$ and for $r_1 \neq r_2$ it drops fast to zero. In case the two mirrors are not equal in their fabrication the resulting mirror reflectnace mismatch can induce a 5-10 dB transmission loss [50]. In the case of a 30-period $Al_{0.9}Ga_{0.1}As/GaAs$ DBR with a reflectance of 99.97% the other mirror reflectance must be 99.91% to keep the loss below 3.1dB (corresponding to $T_{12} \approx 0.5$). This means that the reflectance of the other mirror must be within 600 ppm of the DBR reflectance. Figure 2.9 shows T_{12} in dB as a function of the reflectance, $R = |r_1||r_2|$, for various values of the HCG reflection coefficient, r_2. It can be seen that the higher the value of R, the smaller is the region within which the mirrors match to such a degree that the transmittance is above 50%. Lowering the total reflectance increases the window within which there is less than 3 dB loss, but it also decreases the linewidth as seen in Fig. 2.8. Hence there is a trade-off between lowering the tolerance on the mirror reflectance and narrow linewidth.

Absorption Loss

The HCG and DBR mirrors are both doped to reduce the resistance and minimize the voltage drop across the substrate and the beam suspensions of the top mirror. This increases the absorption by several orders of magnitude relative to that of intrinsic GaAs. Absorption losses of 1-5 dB have been reported in the case of GaAs-based MOEMS filters [57, 56]. Absorption losses are included in the power transmission such that in order to rewrite Eq. 2.14 in terms of the reflectance it is used that now

$$1 = Te^{-A_\lambda} + R$$

where A_λ is the spectral absorbance. Hence Eq. 2.14 becomes

$$T_{FP} = e^{-2A_\lambda} \frac{(1-R)^2}{(1-R)^2 + 4R\sin^2(\delta/2)} \tag{2.19}$$

The Lambert-Beer absorbance of a material with absorption coefficient α is

$$A_\lambda = \alpha x \tag{2.20}$$

where x is the distance into which the wave has propagated. For a 350 μm slab of highly doped n-GaAs (5×10^{18}cm^{-3}) with an absorption coefficient of 40cm^{-1} the fraction of light transmitted will be 25% corresponding to 6 dB loss. Decreasing the doping of n-GaAs (10^{18}cm^{-3}) with an absorption coefficient of 5cm^{-1} the fraction of light transmitted would be 84% or a 0.8 dB loss.

Example

In Fig. 2.10 the resonance wavelength, transmission and linewidth are shown calculated for an example Micro-Opto-Electro-Mechanical Systems (MOEMS) filter based on Eqs. (2.12), (2.16) and (2.18). The MOEMS filter is a $\lambda/2$-cavity filter with a top HCG and bottom 30 pair $Al_{0.9}Ga_{0.1}As$/GaAs DBR. The reflectance and phase for the HCG and DBR have been calculated using the Rigorously Coupled Wave Analysis (RCWA) and Transmission Matrix Method (TMM) method, respectively (see Sec. 2.2.1). The filter resonance wavelength is linear with the air-cavity gap length, g, as expected from Eq. (2.12), while the transmission and filter linewidth are dominated by the variation in reflectance (mainly the HCG).

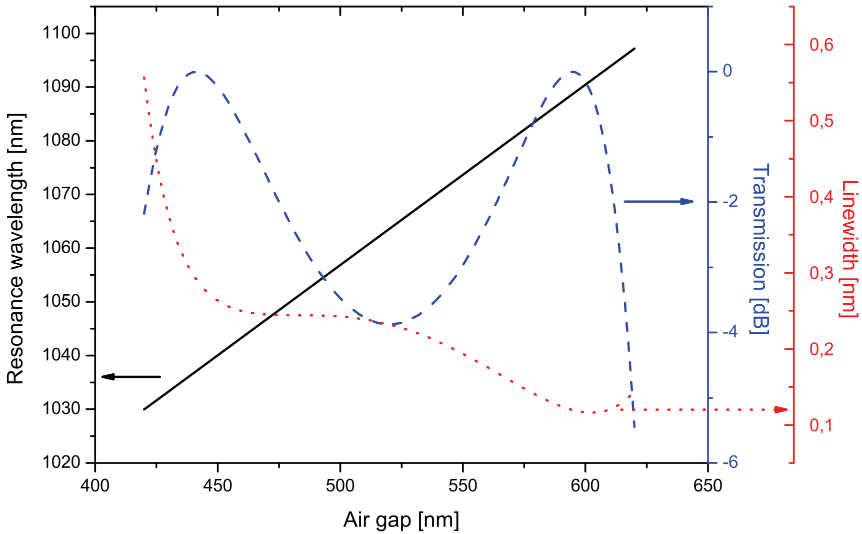

Figure 2.10: Plot of the filter resonance wavelength (solid black), transmission (dash blue) and linewidth (dot red) as a function of the Fabry-Pérot cavity gap.

2.4 HCG-VCSEL

In the preceeding section the Fabry-Pérot filter was presented. The VCSEL consists of a vertical Fabry-Pérot cavity (of length d) made up of two mirrors between which an optical gain medium is situated. Here InGaAs QWs are used as the gain medium. Figure 2.11 shows a schematic drawing of a VCSEL with bottom DBR mirror and top DBR (left) and HCG (right) mirror. The mirrors of the Fabry-Pérot cavity provide feedback for the photon multiplication and lasing occurs as the photon absorption $\langle \alpha_i \rangle$ and mirror loss α_m are balanced by the photon generation or modal gain $\langle g \rangle$. Photon generation is achieved through population inversion of the gain medium, such that electron-hole pair recombination dominates over photon absorption. The cavity length of a VCSEL is very short which provides large spacing between longitudinal modes, but this also requires high reflectivity mirrors to compensate the short gain region. DBRs and HCGs both provides this very high reflectivity, on the order of 99.5% [24, 38, 47, 58].

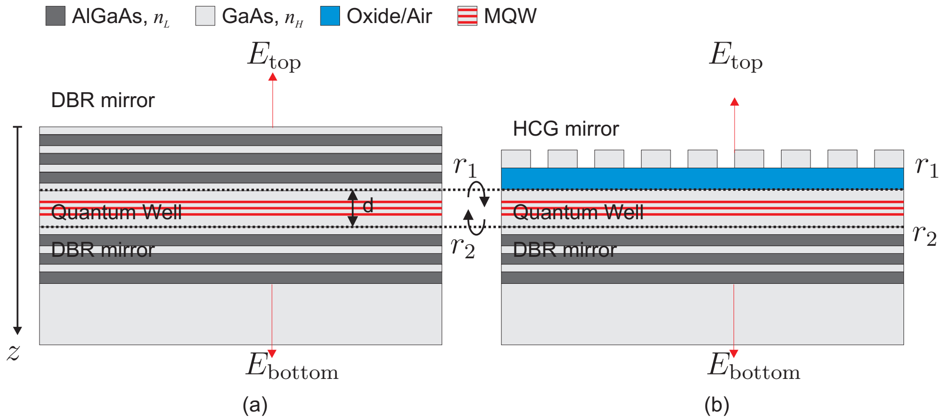

Figure 2.11: Schematic drawing of (left) a DBR VCSEL and (right) a HCG VCSEL. The VCSEL consist of a bottom DBR, a quantum well active region and a top mirror, being either a DBR or HCG.

The DBR VCSEL seen in Fig. 2.11 (a) is the standard VCSEL structure. The DBR reflectance is simply controlled by the number of pairs and the Bragg wavelength λ_B is controlled through the stringent thickness control enabled by Metal-Organic Vapour Phase Epitaxy (MOVPE). The first demonstration of a tunable VCSEL was made by patterning the top DBR mirror into a cantilever [25]. In this way a relative tuning range of 1.6% was achieved. In the following decade VCSEL with top movable DBRs has been presented with 6.5 % and 8.5% relative tuning range for a 1550 and 1300 nm center wavelength, respectively [20, 28]. With the DBR design a wavelength tuning rate of up to 500 kHz has been experimentally demonstrated [20].

In order to increase the tuning rate further the use of a HCG reflector was proposed by Huang *et al.* [19]. Fig. 2.11 (b) show the HCG VCSEL where the high-index contrast is achieved by spacing the subwavelength grating from the semiconductor cavity by air or a low-refractive index medium such as an oxide. The HCG achieves the same high reflectance as the DBR, with much wider wavelength bandwidth, by the meticulous lithographic control of a subwavelength period grating [38, 59]. The HCG enables a significant thickness reduction compared to the DBR which is typically 3-5 μm thick. This both relaxes constraints on epitaxial growth, enables aperture definition through ion implantation and reduces

the mechanical mass for MEMS applications [60]. The reduction of the mirror mass goes into the mechanical resonance frequency as the square root of the reciprocal thickness. Replacing the DBR by a HCG mirror the thickness is reduced by a factor of 10 and thus increase the resonance frequency by a factor of 3. HCG VCSEL tuning rates of 3 MHz has been demonstrated at 0.4% relative tuning range [19].

In this section the theory and design of the HCG-VCSEL will be presented. The reader is referred to Chap. 3 for details on the device fabrication and epitaxial structure. The major difference between the Fabry-Pérot filter and the VCSEL is the inclusion of a semiconductor gain medium. This introduces an undesired reflection at the abrupt change in refractive index between the semiconductor and air region. Hence the VCSEL must be treated as a three-mirror cavity as opposed to the simpler two-mirror cavity [61]. The effects of the parasitic reflection can be circumvented by applying an anti-reflective coating - in which case the two-mirror cavity model suffice. Here we start out by presenting the well-known lasing condition of a standard VCSEL and continue to treat the HCG VCSEL in the two-mirror cavity picture as well as the three-mirror cavity picture.

2.4.1 Lasing condition

The most important aspect of the laser is the light amplification by stimulated emission of radiation. From the steady state requirement that the electrical field repeats itself upon a round-trip propagation the following condition can be derived [37, 54]

$$1 = |r_1||r_2|e^{(\Gamma g - \langle\alpha_i\rangle)d}e^{-i(2\beta d - \theta_1 - \theta_2)}. \tag{2.21}$$

where and r and θ are the reflection coefficient and reflection phase with indices refering to the top (1) and bottom mirror (2) as defined in Fig. 2.11. The phase change during a round-trip is the product of the propagation constant $\beta = \frac{2\pi n}{\lambda}$ and the cavity length d plus the mirror reflection phases $\theta_{1,2}$. The product of the material gain, g, and the confinement factor Γ makes up the modal gain $\langle g\rangle$ [54]. The first exponential in the lasing condition, Eq. (2.21), gives the gain requirements while the second gives the phase requirement.

Gain requirement

In order for lasing to occur the following equality must hold

$$1 = |r_1||r_2|e^{(\Gamma g - \langle \alpha_i \rangle)d}. \tag{2.22}$$

The mirror reflection coefficients are always less than 1 and thus the term of the exponential must be positive. The gain material is InGaAs QWs which provide both electron-hole confinement and an energy level difference engineered to the desired center wavelength λ_0. The dominant optical loss is that of the highly doped regions providing low-resistance current transport as well as the scattering loss of the oxide aperture. Eq. (2.22) can be re-written as

$$\Gamma g_{th} = \alpha_m + \langle \alpha_i \rangle \,, \tag{2.23}$$

where g_{th} is referred to as the threshold material gain required for lasing. In Eq. (2.23) the mirror loss was defined as

$$\alpha_m = \frac{1}{d} \ln \left(\frac{1}{|r_1||r_2|} \right) \tag{2.24}$$

Eq. (2.23) shows that the threshold material gain must balance the mirror and material loss, where the latter can be taken to be constant. The mirror loss on the other hand depends on the mirror reflection coefficient which is strongly wavelength dependent away from the Bragg wavelength. The modal gain $\langle g \rangle$ is mainly affected by the position of the QWs in the vertical direction and the mode confinement by the oxide aperture. The oxide aperture provides confinement of both electrons and photons. The electron confinement reduces current leakage and ensures that the gain material is under population inversion in the same region as is occupied by the optical mode [62, 63]. The oxide aperture further introduces scattering for higher order modes which can be used to ensure single-mode operation.

Phase requirement

From the second exponential in Eq. (2.21) follows the requirement that the round-trip electric-field must be in-phase fulfilling

$$2\pi m = 2\beta d - \theta_1 - \theta_2 \tag{2.25}$$

where

$$\beta = \frac{2\pi n}{\lambda}. \tag{2.26}$$

For a VCSEL with DBR mirrors both mirror reflection phases $\theta_{1,2}$ are zero at the Bragg wavelength and the cavity resonance wavelength is given by Eq. 2.1.

2.4.2 Method

To design the VCSEL we must have a method to calculate the mirror reflectance (covered in Sec. 2.2) and a method to calculate the modal gain, Γg. As stated by Eq. (2.23), these two quantities together with the optical loss $\langle \alpha_i \rangle$ determine whether lasing can be achieved or not. The CAvity Modelling FRamework (CAMFR) has been used to solve for the resonance wavelength and threshold material gain [64, 65, 66]. The CAMFR package relies on the eigenmode expansion method. The refractive index and possible index variation is defined for each layer in the structure. In the eigenmode method the forward propagating electric field in each layer is a periodic function that can be written

$$E(x, y) = E_i(x, y) \exp\{-j\beta z\} \tag{2.27}$$

which satisfy Maxwells equation in the form of an eigenvalue problem. Equation (2.27) is the eigenmode of this eigenvalue problem and using Fourier expansion any field profile can be represented. This works well for the 1D simulations where a computationally efficient number of modes ($N > 30$) is needed for convergence of the single-period HCG reflectivity. For simulation of the full structure, with multiple periods of the HCG, the number of modes required for convergence makes the computation time prohibitive to the design process. For a 20 period HCG, needed to span the oxide aperture, the number of modes needed is 600. In order to keep computation time reasonable the oxide aperture is excluded from the model and thus the optical scattering losses induced by the oxide aperture are not included in the results. In order to calculate the threshold material gain of the design 2D Finite-Difference Time-Domain (FDTD) calculations have been done to include the effects of the oxide aperture [36]. For the simulation of the full structure with a DBR top mirror the calculation of the gain for a solid cavity VCSELs using CAMFR has been shown to compare to other models [65].

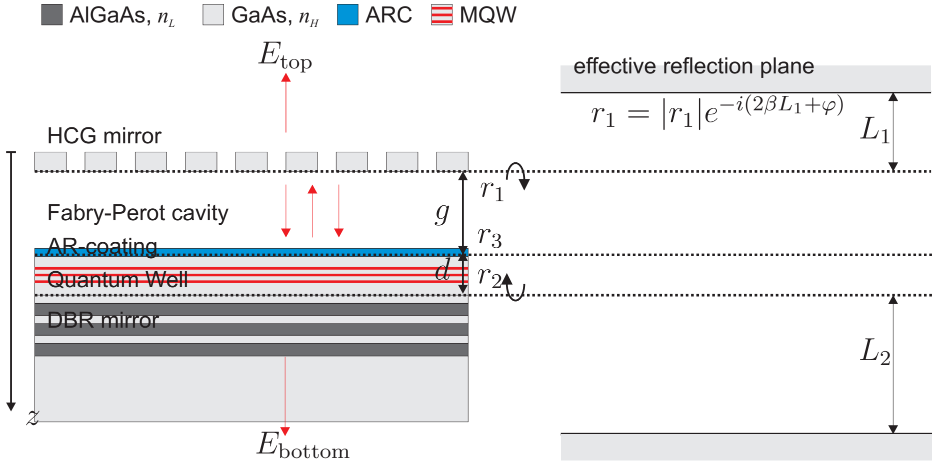

Figure 2.12: Tunable VCSEL schematic (left) and model (right). The VCSEL consist of a bottom DBR, a quantum well active region, anti-reflective coating, an air-gap and a top HCG. In the model the mirrors are represented by hard mirrors with a reflectance $|r|^2$ at a distance L and phase-shift φ from the physical reflection plane (see Eq. 2.11).

2.4.3 Two mirror Fabry-Pérot cavity

The two-mirror cavity is conceptually the simplest. For the treatment to be valid we imagine that the internal air-semiconductor interface is coated with an ideal anti-reflective coating. Figure 2.12 shows the HCG VCSEL with anti-reflective coating at the internal air-semiconductor interface. The reflection, r_3, at the air-semiconductor interface is taken to be negligible.

Lasing condition

With the introduction of a passive region into the cavity the lasing condition Eq. (2.21) changes accordingly to

$$1 = |r_1||r_2|e^{(\Gamma g - \langle\alpha_a\rangle)d_a - \langle\alpha_p\rangle d_p}e^{-i(2\beta d - \theta_1 - \theta_2)} \tag{2.28}$$

Given that the absorption of the air region is zero and by neglecting the loss in the mirrors, the gain condition simplifies to that of Eq. (2.22). The phase condition becomes

$$2\pi m = 2\sum_i \frac{2\pi n_i}{\lambda_m} d_i - \theta_1 - \theta_2, \tag{2.29}$$

where the summation is over the optical length of all the layers making up the cavity. At the Bragg wavelength the DBR reflection phase $\theta_{\text{DBR}} = 0$, while the HCG reflection phase θ_{HCG} can be taken as a correction to the air-gap given by $-\frac{\lambda_m}{4\pi n}\theta_{\text{HCG}}$. Eq. (2.29) can be used in the design of the HCG-VCSEL epi-structure to be resonant at the wavelength λ_0. From the phase condition Eq. (2.29) the cavity resonance wavelength becomes

$$\lambda_m = \frac{4\pi}{2\pi m + \varphi_1 + \varphi_2} D_{\text{eff}}. \tag{2.30}$$

Here D_{eff} has been defined as the total optical length of the cavity. The shift in wavelength with a change in the air-gap length, also referred to as the tuning efficiency, can then be written as

$$\frac{\partial \lambda_m}{\partial g} = \frac{4\pi}{2\pi m + \varphi_1 + \varphi_2} = \frac{\lambda_m}{D_{\text{eff}}} \tag{2.31}$$

Eq. (2.31) shows that the tuning efficiency is inversely proportional to the effective cavity length D_{eff}, which provides the guideline that the cavity length must be minimized [28]. The full spectral range

$$\text{FSR} = \lambda_m - \lambda_{m+1} = \frac{\lambda_m^2}{2D_{\text{eff}}} \tag{2.32}$$

is inversely proportional to the effective cavity length. The FSR sets the upper limit on the continous wavelength tuning range. For the HCG-VCSEL design seen in Tab. 2.1 the tuning efficiency is $\frac{\partial \lambda_m}{\partial d_{\text{air}}} = 0.212$ and the FSR is 113 nm. In the case that electro-static actuation is used in changing the air-gap, the absolute change is limited to $\frac{1}{3}$ of the initial air gap thickness due to the pull-in instability. Then the maximum tuning range becomes

$$\Delta\lambda = \frac{\partial \lambda_m}{\partial g}\Delta g = 0.212 \cdot \frac{0.46\lambda_0}{3} = 0.033\lambda_0 = 35\text{nm} \tag{2.33}$$

which is well within the FSR. Hence for electro-static actuation the FSR will not be the limiting factor for a fundamental-cavity design. The tuning range can be extended by increasing the initial air-gap distance, which will slightly decrease the tuning efficiency. Since pull-in limits the tuning range it can be nearly doubled by increasing the air-gap thickness to the next integer mode, as the tuning

Section	τ	$n_g L$	φ
HCG	3.9 fs	$0.55\lambda_0$	2.04π
Air-gap		$0.46\lambda_0$	0
AR-coating		$0.25\lambda_0$	0
Semiconductor		$1.78\lambda_0$	0
30-pair DBR	11.8 fs	$1.67\lambda_0$	6.69π
Total, D_{eff}		$4.71\lambda_0$	8.7π

Table 2.1: Reflection delay τ, penetration depth L and constant reflection phase φ for the two types of mirrors. The DBR is a 30-pair $Al_{0.9}GaAs/GaAs$ stack designed for $\lambda_0 = 1060$ nm. The HCG is a 280 nm thick GaAs slab with a grating period of 460 nm and duty cycle of 72%.

efficiency and FSR only decrease by 10% in the given example (referring to Tab. 2.1 the total cavity length D_{eff} only increase by 10%). Recalling that the 99.5% bandwidth of the $Al_{0.9}GaAs/GaAs$ DBR was 80 nm, pull-in is expected to set the upper limit on the tuning range.

Mode confinement

The field distribution throughout the device structure or the standing wave pattern at lasing was calculated using CAMFR. Fig. 2.13 shows an example of a standing wave pattern of a HCG-VCSEL with a $\lambda_0/2$ air-gap, an ideal anti-reflection coating, an oxide aperture and 3 QWs where the cavity thickness, d, has been chosen such that phase condition, Eq. (2.21), is fullfilled at 1060 nm. Fig. 2.13 shows how the field anti-node is aligned to the QW such that the material threshold gain is minimum. In this example the oxide aperture is also placed at the field anti-node in order to maximize optical confinement. The oxide position is a trade-off between optical scattering loss from the thin oxide aperture and optical confinement [67]. Strong optical confinement results from placing the oxide aperture at the field anti-node at the expense of higher optical scattering loss. Placing the oxide aperture at the field node the optical scattering loss is smaller, but this also results in poor optical confinement why the mode will spread over a larger mode volume. This will decrease the overlap of the optical mode with the region of population inversion and increase optical loss through absorption.

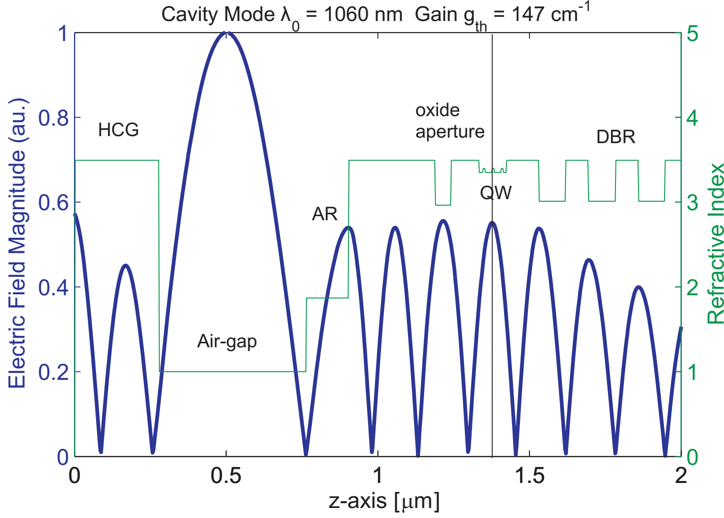

Figure 2.13: Plot of the standing wave electric field in a HCG-VCSEL with 30-pair $Al_{0.9}GaAs/GaAs$ DBR with $\lambda_B = 1060$ nm and HCG with 280 nm thickness, 460 nm period and 72% duty cycle. The HCG-VCSEL has a 530 nm air-gap and $\frac{\lambda_0}{4n}$ ideal single-layer anti-reflection coating. The oxide current aperture and 3 QWs both aligned to the electric field anti-node.

The 1D simulation shows a 15% reduction in the threshold material gain with the oxide aperture placed at the field node. In order to optimize the position of the oxide aperture in terms of lateral confinement 2D simulations has been done.

Output power

The laser output power above threshold is given by

$$P = \eta \frac{h\nu}{q} (I - I_{\text{th}}) \tag{2.34}$$

where η is the differential quantum efficiency. This is the *total* power output, but normally it is the power output of either the top or bottom mirror that is of interest. The light escaping the cavity through the mirrors is determined by the mirror transmittivities and if they are not equal the power output out of the two mirrors will not be either. The fractional power output of mirror 1

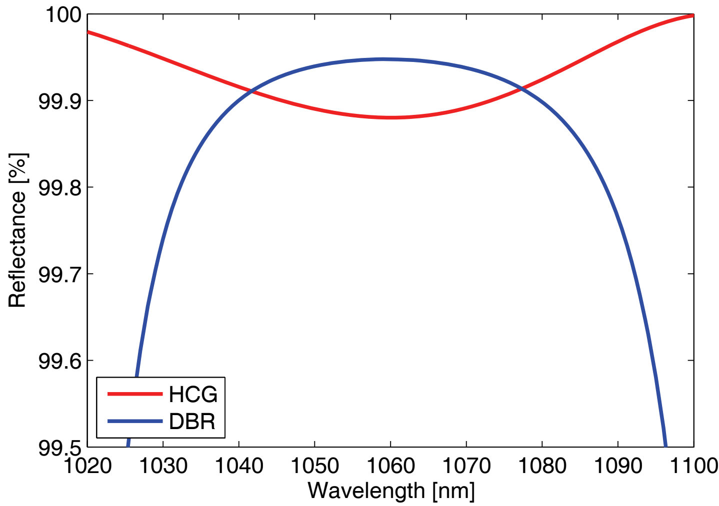

Figure 2.14: The reflectance for a 30-pair $Al_{0.9}GaAs/GaAs$ DBR with λ_B = 1060 nm and HCG with 280 nm thickness, 460 nm period and 72% duty cycle.

is determined by

$$F_1 = \frac{t_1^2}{(1 - r_1^2) + \frac{r_1}{r_2}(1 - r_2^2)} \tag{2.35}$$

where the indices refers to the top (1) and bottom (2) mirror. Fig. 2.14 shows the reflectance of a 30-pair $Al_{0.9}GaAs/GaAs$ DBR with λ_B = 1060 nm and HCG with 280 nm thickness, 460 nm period and 72% duty cycle. The reflectance of the HCG has a high bandwidth characterized by two resonances. As seen from Fig. 2.14 the HCG reflectance is higher than the bottom DBR outside a 40 nm bandwidth. This would result in a roll-off in the power output through the top mirror, but it remains to be experimentally demonstrated what the upper limit is to the HCG reflectance. Hence this roll-off may not be observed in experiments. The high HCG reflectance could be used to an advantage in bottom emitting devices. This is viable for VCSEL beyond 980 nm, but at lower wavelength optical absorption in the GaAs substrate will limit the power output. Another solution would be to use $Al_2O_3/GaAs$ bottom mirrors, that have a much broader bandwidth, to ensure top emission.

2.4.4 Three mirror Fabry-Pérot cavity

The refractive index continuity between the active and passive part of the laser cavity, seen in Fig. 2.12, must be included to properly model the cavity resonance. The large index contrast between the gain region and the air region, with no anti-reflective coating present, will cause a reflection of $|r_3|^2 = 30\%$. In the preceeding section Sec. 2.4.3 a two mirror Fabry-Pérot laser cavity was treated, by neglecting the reflection at the semiconductor-air interface. This will be shown to be a valid assumption in the case of an anti-reflective coated interface. Removing the anti-reflective coating, two different cases arise where either the field magnitude is largest in the air-gap or in the semiconductor [68]. The two situations are referred to as the air-coupled and the semiconductor-coupled cavity, respectively. For the total round-trip phase to add up we still adhere to the requirement of Eq. (2.29), namely that the total cavity optical length is a integer multiple of $\lambda_0/2$.
Following the treatment in [54] the three-mirror cavity can be treated in the same way as the two-mirror cavity, where the air-HCG section is replaced by an effective reflectance, r_{eff}, that includes the semiconductor-air interface

$$r_{\text{eff}} = r_3 + \frac{t_3^2 r_1 e^{-j(2\beta g - \theta_1)}}{1 + r_3 r_1 e^{j(\theta_1 - 2\beta g)}}. \tag{2.36}$$

where

$$r_3 = \frac{n_{\text{GaAs}} - 1}{n_{\text{GaAs}} + 1} \quad \text{and} \quad t_3 = \sqrt{1 - r_3^2}. \tag{2.37}$$

Figure 2.15 shows Eq. (2.36) plotted versus the air-gap length βg. In Fig. 2.15 there are two distinct regions. For $\frac{\lambda}{2}m$ there is an minimum in reflectance and the slope of the reflection phase is highest. This corresponds to the air-coupled case. For $\frac{\lambda}{4}(2m+1)$ there is a maximum in reflectance and the slope of the reflection phase is smallest. This corresponds to the semiconductor-coupled case. The phase condition for the coupled cavity is

$$2\pi m + \varphi_{\text{DBR}} = \frac{4\pi}{\lambda} \underbrace{(nd + nL_{\text{DBR}})}_{D_{\text{eff}}} - \theta_{\text{eff}}(g) \tag{2.38}$$

from which the tuning efficiency follows as

$$\frac{\partial \lambda_m}{\partial g} = -\frac{\lambda_m^2}{4\pi D_{\text{eff}}} \frac{\partial \theta_{\text{eff}}}{\partial g}. \tag{2.39}$$

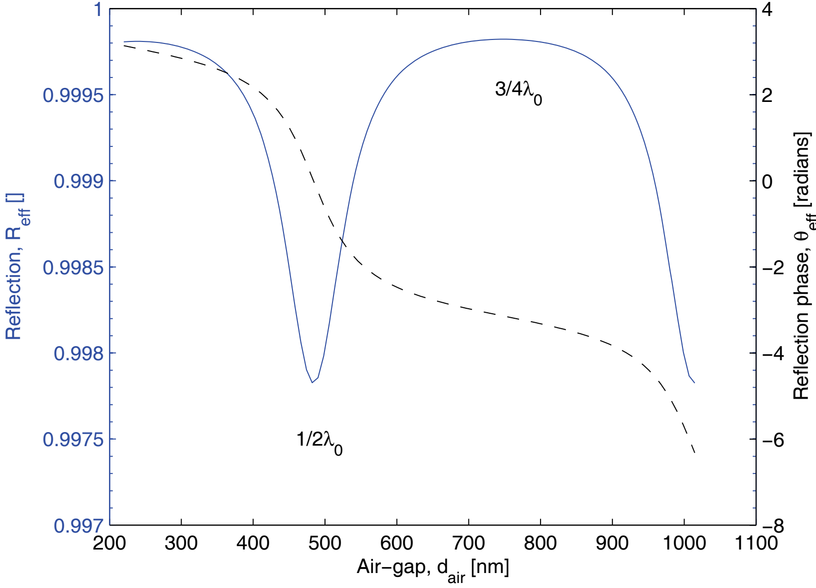

Figure 2.15: Plot of the effective reflectance, R_{eff} and the reflection phase, θ_{eff}, for the semiconductor-air-HCG effective mirror.

From Eq. 2.39 it can be concluded that the wavelength change is proportional to the effective mirror reflection phase change.

Air-coupled cavity

For the air-coupled cavity the optical thickness of the air-region must be $ng = \frac{\lambda}{2}m$. The air-coupled cavity has the advantage of a high tuning efficiency, while the drawback is that the optical field is highest in the air-region where the optical gain is zero. The derivative of the reflection phase is found to be $\frac{\partial\theta_{\text{eff}}}{\partial g} = -0.0406/\text{nm}$ and inserting in Eq. (2.39) the tuning efficiency is calculated to be 0.927 using the values in Tab. 2.2.

Semiconductor-coupled cavity

For the semiconductor-coupled cavity the optical thickness must be $ng = \frac{\lambda}{4}(2m + 1)$. The semiconductor-coupled cavity has the advantage of a low threshold material gain, while the drawback is that the tuning efficiency is low. The derivative of the reflection

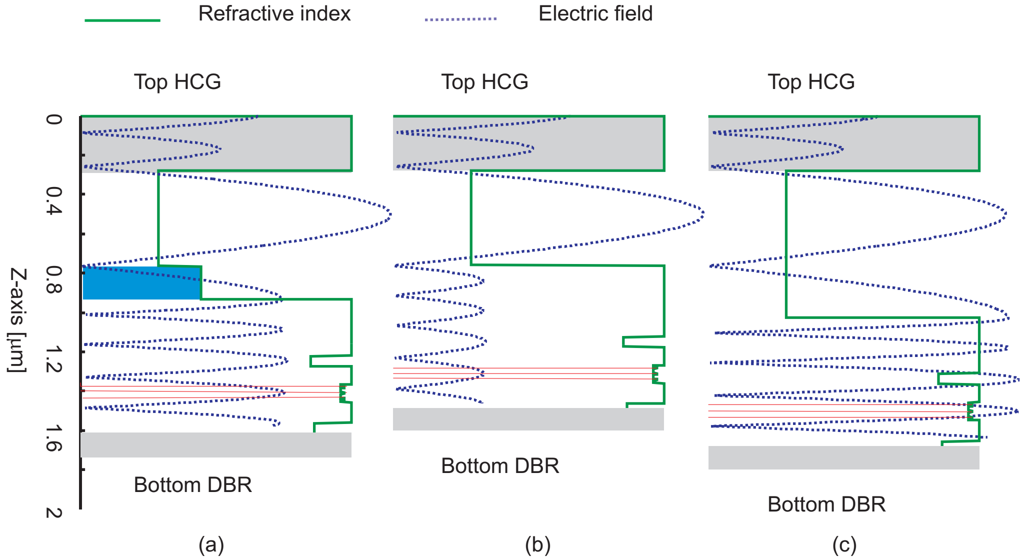

Figure 2.16: Plot of the refractive index (solid) and electric field (dashed) from the top HCG to the bottom DBR for an (a) extended cavity (b) air-coupled cavity (c) semiconductor-coupled cavity.

phase is found to be $\frac{\partial \theta_{\text{eff}}}{\partial g} = -0.0035/\text{nm}$ from which the tuning efficiency results as 0.086.

2.4.5 Summary

In sections 2.4.3 and 2.4.4 three possible cavity design has been discussed, namely the (a) extended cavity, (b) the air-coupled cavity and (c) the semiconductor coupled cavity. In order to tune the physical length of the cavity, part of it must be air and this results in an unwanted reflectance between the air and semiconductor region. This situation can be analyzed as a three-mirror cavity. Table 2.2 compares the tuning efficiency, range and minimum threshold material gain for an extended cavity with ideal anti-reflective coating, extended cavity with Al_2O_3 anti-reflective coating, air-coupled cavity and semiconductor-coupled cavity. The standing wave pattern can be seen in Fig. 2.16, which shows how the electric field is more strongly confined in the air region for the air-coupled cavity. From Tab. 2.2 it is seen that the tuning efficiency of the extended cavity is twice that of the semiconductor-coupled cavity, while the minimum threshold material gain is only 20% larger. The tun-

Structure	Air λ_0	Cavity λ_0	D_{tot} λ_0	Efficiency [nm/nm]	Range [nm]	g_{min} [cm^{-1}]
Ideal ARC	0.707	1.779	4.75	0.212 (0.213)	34 (37)	140
AlOx ARC	0.707	1.779	4.75	0.212 (0.162)	26 (29)	120
Air-coupled	0.457	2.025	4.70	0.927 (0.474)	77 (42)	327
Semiconductor-coupled	0.707	1.775	4.74	0.086 (0.069)	17 (18)	98

Table 2.2: shows the tuning efficiency and range for different HCG-VCSEL cavity design together with the minimum gain (at $\lambda_0 = 1060$ nm). The range is limited by electro-static pull-in to 1/3 of the initial gap spacing. The tuning range value in parenthesis is the numerical value from CAMFR. The HCG initial phase is $\theta_{\text{HCG}} = -0.535$ and the effective length $L_{\text{HCG}} = 0.55\lambda_0$ and the bottom DBR 30 pair GaAs/$\text{Al}_{0.9}$GaAs has an effective length of $L_{\text{DBR}} = 1.67\lambda_0$.

ing efficiency of the air-coupled cavity is several times higher than the semiconductor-coupled cavity, but in practise it is limited by high threshold material gain. Tab. 2.2 shows the tuning efficiency for different design computed from the analytical expression in Eq. (2.31) compared to the result computed by CAMFR (in parentheses). For a VCSEL structure with a perfect anti-reflective coating, the analytical result of Sec. 2.4.3 matches the numerical result. From the analytical and numerical modelling it is found that there is a trade-off between low threshold material gain and high tuning efficiency for the three-mirror cavity. In order to overcome this limitation the internal semiconductor-air interface can be coated with an anti-reflective coating. The refractive index of the anti-reflection coating should preferably be as close to $\sqrt{n_{\text{cav}}} = \sqrt{3.5} = 1.87$ as possible. For a fully epitaxial solution the oxide of AlAs can be used which has a refractive index close to 1.6. From Tab. 2.2 this is seen to result in a decrease of the tuning efficiency by 24%. Nevertheless the tuning efficiency is still 60% larger than the semiconductor coupled cavity, while the threshold material gain is only 22% larger.

Fig. 2.17 shows a plot of the threshold material gain as function of the wavelength detuning, $\lambda - \lambda_0$, for the Al_2O_3 coated extended cavity, air-coupled cavity and semiconductor-coupled cavity. Again the threshold material gain is seen to be lowest for the semiconductor-coupled cavity, but the extended cavity shows are more flat curve.

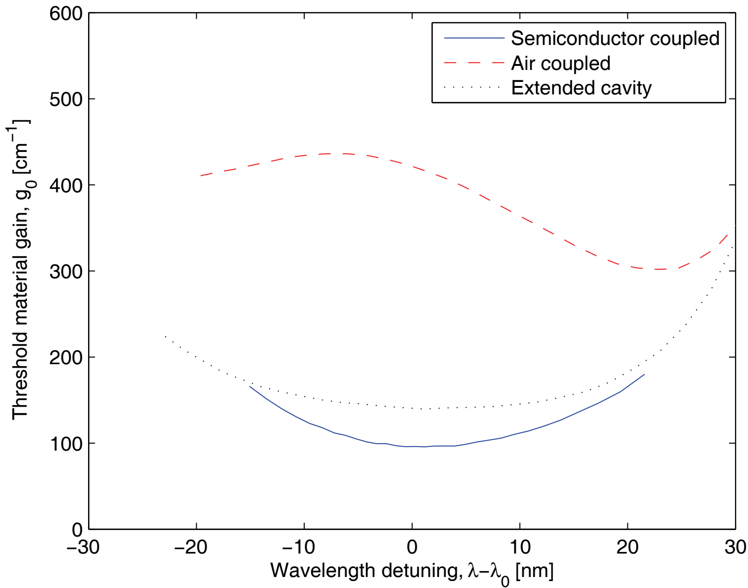

Figure 2.17: Plot of the threshold material gain as function of the wavelength detuning, $\lambda - \lambda_0$, from the intial wavelength λ_0 for the three possible cavity configurations: semiconductor coupled (solid), air coupled (dashed) and extended cavity (dotted)

2.5 Electro-static actuation

The most straight-forward way to implement tuning of the air-gap distance is through electro-static actuation. This only requires electrical contacts to the top and bottom mirrors, both of which should be conductive, and a mechanical suspension of the top mirror. Fig. 2.18 shows a schematic drawing of how this could be implemented. The mechanical suspension (spring) counters the electrostatic forces and the gap distance can then be controlled through what is an electrostatic actuator. Piezo-electric actuation was also considered at the outset of the project. This would enable larger tuning range, but also require more elaborate process development and it is not yet clear whether meaningfull actuation ranges can be achieved [33].

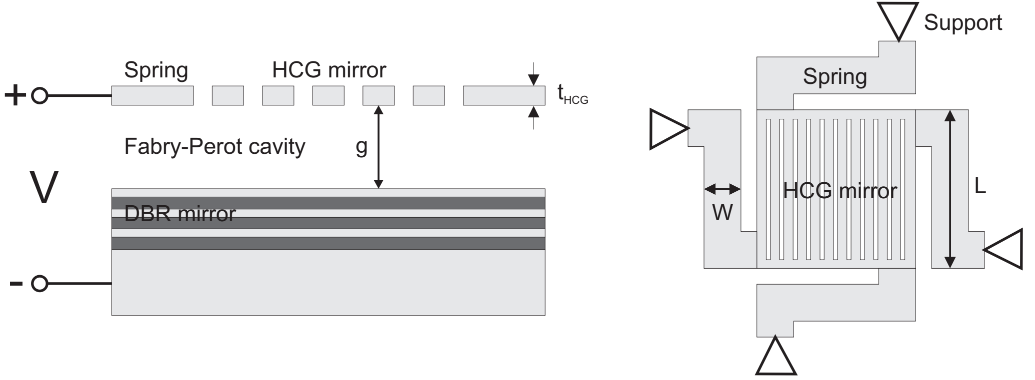

Figure 2.18: Schematic of the electro-mechanical design of the filter.

2.5.1 Static operation

The electro-static tuning of the MEMS VCSEL can be described through the electro-static force on the parallel-plate capacitance between the HCG and the substrate. In the derivation of the electric force the fringing field is assumed negligible. In Fig. 2.18 the grating structure of the HCG mirror is shown. The grating consists of bars and air spacing and because the mirror is not solid fringing fields will exist between the bars. Due to the symmetry the electric field profile in the air-gap will be very similar to that of a solid mirror and only perimeter will contribute to the fringing field. The displacement of the HCG mirror can be controlled by electrostatic actuation using a voltage source. The force acting on a capacitive element of area A is [69]

$$F_{\mathrm{el}} = \frac{\epsilon A V_{DC}^2}{2g^2} \tag{2.40}$$

where the gap distance

$$g = g_0 - w \tag{2.41}$$

can be written in terms of the initial gap distance g_0 and the mirror displacement w. The mechanical force, $F_{\mathrm{mech}} = kw$ and the electrical force F_{el} balance each other at a gap distance of

$$g = g_0 - \frac{\epsilon A V_{DC}^2}{2kg^2}. \tag{2.42}$$

Eqs. (2.40) and (2.42) shows the non-linear behaviour of the voltage-controlled electro-static actuator. Eq. (2.42) has two equilibrium

gap distances g until it reaches the pull-in instability at g_{PI} above which the electrostatic force is larger than the mechanical restoration force for all g. From the requirement that the tangential of the two forces are equal this found to occur for $g_{\mathrm{PI}} = \frac{2}{3}g_0$ at a voltage of

$$V_{\mathrm{PI}} = \sqrt{\frac{8kg_0^3}{27\epsilon A}}. \tag{2.43}$$

The above analysis readily applies to the case of the HCG VCSEL which has the same electro-mechanical structure. In the case of the HCG VCSEL with anti-reflective coating (ARC) the capacitance changes due to the presence of an isolating oxide. This can be accounted for in substituting $g = g' - t_{\mathrm{ox}}$ in the above equations, where g' is the physical air gap distance and t_{ox} the coating of the oxide.

The function of the mechanical suspension is to allow the mirror to move in the vertical direction, while maintaining its flatness. Hence it is mainly the mechanical suspension, the spring, that is deforming under the applied electrostatic load. The mirror is taken to be a rigid plate, which is connected to a solid support by four fixed-guided beams. Simply due to the larger size of the mirror it will have a higher stiffness. The stiffness of a fixed-guide beam is found solving the Euler equation [69]

$$K = \frac{EWH^3}{(\chi L)^3} \tag{2.44}$$

where E is the Youngs modulus ($E_{\mathrm{GaAs}} = 85.9$ GPa), W is the width, H the thickness and χL the length of the spring. In the mechanical design of Fig. 2.18 the HCG is attached to 4 springs why the total spring constant, k is four times that given by Eq. (2.44).

Electrostatic spring softening

The spring suspension will also experience a distributed electrostatic force

$$EI\frac{\partial^4 w(x)}{\partial x^4} = q(x) = \frac{\epsilon(\chi L)V^2}{2(g_0 - w(x))^2} \tag{2.45}$$

where $w(x)$ is the displacement, g_0 the gap distance at zero voltage $V = 0$. Through a Taylor expansion of the right-hand side of

Eq. (2.45) around $w(x) = 0$ the differential equation is linearized, resulting in an electrostatic spring constant

$$K_{\text{elec}} = -\frac{\epsilon a V_{DC}^2}{g_0^3} \tag{2.46}$$

The sign in Eq. (2.46) shows that increasing the electro-static force, as given by Eq. (2.40), results in a decrease of the beam stiffness. This results in a decrease of the resonance frequency at large-signal modulation and the electro-static spring softening must be taken into account when estimating the displacement versus voltage characteristic of the MEMS. Fig. 2.19 shows a plot of the gap distance versus voltage for a $\frac{1}{2}\lambda_0$-cavity. The displacement has been computed from the analytical expression Eqs. (2.44) and (2.46) and by using a finite-element model (FEM) implemented in COMSOL. The FEM is implemented using a moving mesh to account for the change in gap distance when computing the electro-static force from which the mechanical deformation is computed. The relative error of the displacement is reduced by half using the first order estimate of the electro-static spring softening.

2.5.2 Dynamic operation

The dynamics of the mirror is determined by Newton's second law which couples the mirror mass acceleration to the spring constant. Due to squeeze film damping, the dynamic response for the actuator will be damped in operation at atmospheric pressure, while in vacuum the actuator will behave as a simple oscillator due to the abscene of a frictional force [70]. The mirror can be analyzed in terms of the classical harmonic oscillator with damping. The equation of motion of the mirror may in dimension-less form, be expressed as [69, 71, 72]

$$\ddot{u} + \frac{\omega_0}{Q}\dot{u} + \omega_0^2 u = \frac{4}{27}\left(\frac{V}{V_{\text{PI}}}\right)^2 \frac{\omega_0^2}{(1-u)^2} \tag{2.47}$$

where $u = z/g_0$ is the normalized deflection, Q is the quality factor, ω_0 is the angular resonance frequency, V the bias voltage and V_{PI} the pull-in voltage. The driving force of the harmonic oscillator is the electro-static non-linear term at the right of Eq. (2.47). Doing

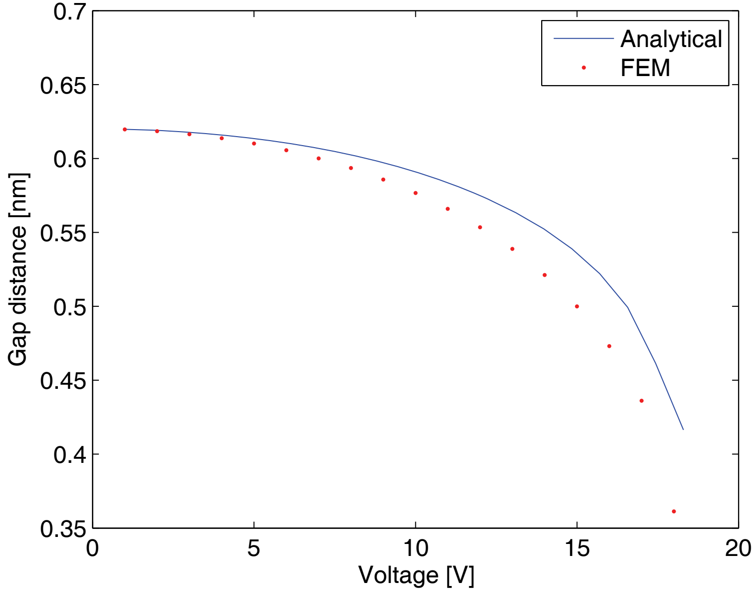

Figure 2.19: Plot of the electro-mechanical deflection versus the capacitor voltage. The beam thickness is 0.28 μm, the width 1.5μm and the HCG mirror has a sidelength of 12μm.

a series expansion of the right-hand side of Eq. (2.47) in terms of the normalized deflection u the electro-static driving force per unit mass, F'_{el} writes as

$$F'_{\text{el}} = \frac{4\omega_0^2}{27}\left(\frac{V}{V_{\text{PI}}}\right)^2 \left(1 + 2u + 3u^2 + 4u^3 + \mathcal{O}(u^4)\right). \tag{2.48}$$

For the linear harmonic oscillator a forced oscillation will result in a time-dependent deflection of

$$u(t) = \frac{4}{27}\left(\frac{V}{V_{PI}}\right)^2 \frac{\omega_0^2}{\sqrt{\left(\omega_0^2 - \omega^2\right)^2 + \left(\omega_0^2/Q\right)^2}} \cos(\omega t - \phi) \tag{2.49}$$

which has a peak at $\omega = \omega_0$, its magnitude proportional to the quality factor Q. The phase lag of the deflection amplitude to the driving force is given by

$$\tan\phi = \frac{1}{Q}\frac{\omega/\omega_0}{\omega_0^2 - \omega^2} \tag{2.50}$$

The first higher order term ($2u$) of Eq. (2.48) results in a reduction of the spring constant (see Eq. (2.46)), why it is commonly referred to as the electro-static spring softening. The second ($3u^2$) and third ($4u^3$) higher order terms are additional corrections to the spring constant. The correction term to the third order is often referred to as the Duffing constant as it appears in the Duffing equation. The higher order terms mainly affect the behavior near resonance, which is seen as hysteresis in the amplitude frequency response [70]. Hence we note that the non-linear terms turns up as a correction to ω in Eq. (2.49).
Generally downwards tuning (blue-shifting) from the initial emission wavelength is considered applicable to MEMS VCSEL when static operation is considered. Here we show that by considering dynamic operation upwards wavelength tuning (red-shifting) can be achieved.

Resonance frequency

The resonance frequency of the mirror can be estimated as

$$\omega = \sqrt{\frac{4K}{m}} \tag{2.51}$$

where m is the mass

$$m = \rho L^2 H \tag{2.52}$$

and K is the total spring force. Fig. 2.20 shows the resonance frequency versus the mirror sidelength for a beam length fixed to the mirror sidelength. The mechanical resonance frequency increases into the 100 kHz range below a mirror sidelength of 40 μm. The inset in Fig. 2.20 shows the COMSOL model of the mirror with a color-graded vertical deformation (red = largest deformation, blue = no deformation). This shows how the mirror stay planar to a large extent, while it is the beams that carry the deformation. The design in Fig. 2.20 is for the Fabry-Pérot filter, while similar results apply to the HCG-VCSEL. The HCG-VCSEL is not as the Fabry-Pérot filter limited by the focusing and coupling of the filtered light beam and smaller mirrors can be used. This increases the obtainable mechanical resonance frequency towards the MHz regime.

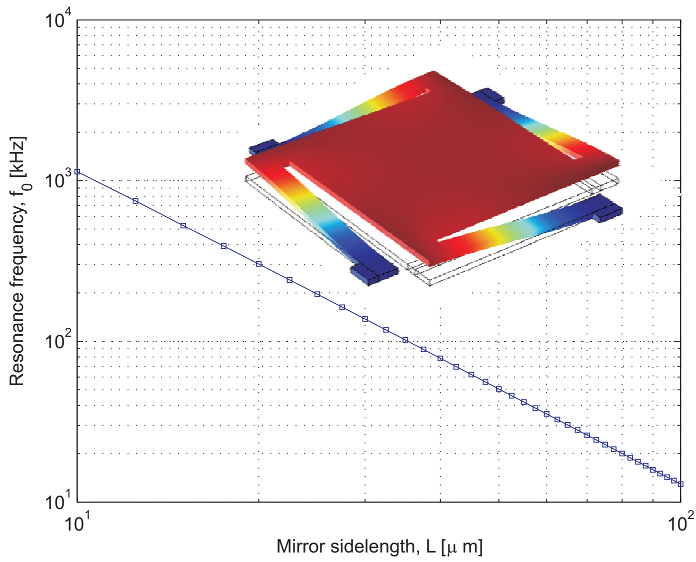

Figure 2.20: Plot of the resonance frequency for a HCG Fabry-Pérot cavity as function of the mirror sidelength L calculated using COMSOL. The beam width is fixed at $W = L/10$.

Chapter 3

Device fabrication

In this chapter the device fabrication is presented together with the measurements done in order to qualify the process. The major part of the thesis work has been put into process development. A process for the fabrication of monolithic MOEMS has been developed based on an AlInP sacrificial process. Furthermore, growth of an $In_{0.3}Ga_{0.7}As$ Multiple Quantum Well (MQW) has been developed in order to fabricate a tunable VCSEL at 1060 nm. The epitaxial growth is covered in Sec. 3.1 where an accounts is given for both the development of strained InGaAs MQWs and lattice-matched InAlP together with considerations on growing the full epitaxial structure for the VCSELs. InAlP is used as a sacrificial layer to define the tunable air-gap and since the anisotropic wet etching of InAlP is not covered in literature, a detailed account is given in Sec. 3.2. This is followed by another part of the process development work which has been the patterning of subwavelength gratings. The different masking and patterning techniques that have been investigated are described in Sec. 3.3. The chapter ends with a description of the process flow for making the Fabry-Pérot filters, VCSELs and HCG VCSELs that are part of this thesis. This is covered in Secs. 3.4-3.6. The process flow for the DBR VCSEL was developed prior to this work.

3.1 Epitaxial growth

The goal of this project has been to realize a tunable VCSEL with a center wavelength at 1060 nm. Within telecommunication em-

phasis has been put on 850, 980, 1310 and 1550 nm, while 1060 nm has mainly found its use as seed laser diode in second harmonic generation of green light and supercontinuum generation in optical fibers. For VCSELs in this wavelength, InGaAs grown on GaAs is favoured due to the high index contrast of AlGaAs/GaAs DBRs. The disadvantage is that InGaAs is not lattice-matched to GaAs and the strain give rise to growth instabilities. InGaAs Quantum Well (QW) gain material is used for 980 nm VCSELs where the strain increases the differential gain which in return allows for higher modulation frequencies to be reached. The commercial use of 1310 nm VCSELs has made several research groups interested in pushing the boundary for growth of InGaAs QWs [73, 74, 75, 76]. The two main approaches in growing long-wavelength InGaAs QWs has been to either suppress growth defects by lowering the growth temperature or to use strain-balancing barriers. In this work we established the growth parameters at DTU for growing 1060 nm $In_{0.28}Ga_{0.72}As$ MQW as presented by Hou et. al. using GaAsP barriers for strain-balancing [77].

The growth was done using an Emcore D-125 Turbodisc® equipped MOVPE rotating disk reactor. The growth pressure was fixed at 80 Torr. Epi-ready 50 mm (100) GaAs wafers with the major flat cut along $\left[0\bar{1}\bar{1}\right]$ were used for all growths. The MOVPE was equipped with hydrogen (H_2) as carrier gas. For the group III the precursors trimethylgalium (TMGa), trimethylindium (TMIn), trimethylaluminum (TMAl) were used and for the group V arsine (AsH_3), phosphine (PH_3) and tributhylphosphine (TBP). The n-dopant was disilane (Si_2H_6) and the p-dopant carbon tetrabromide (CBr_4). The epitaxial growth for all devices was done on polished n-doped GaAs grown by the vertical gradient freeze method. As has been noted in the literature the substrate quality is key in order to obtain good epitaxial wafers [74]. The same recipe on different substrates would yield completely different growth results both in term of composition and growth instabilities. We have painstakingly found the same result.[1]

[1]Poor crystal quality GaAs leads to surface rougness, and thus lower X-Ray Diffraction (XRD) signal, while the Photoluminescence (PL) does not suffer unless the surface roughness triggers growth instabilities. A large number of wafers from the same ingot would show a high PL-signal at the edges and low in the center with a hazy surface finish. The exact same growth on a wafer

Epitaxial growth is done in the mass transport limited regime with a high partial pressure of the group V constituents. This has the consequence that the growth rate is limited by the diffusion of group III constituents to the V-rich GaAs surface. The solid composition, x_s, of ternary materials $A_xB_{1-x}C$ with a single group V element is controlled through the vapor phase composition $x_v = \frac{[A]}{[A]+[B]}$. Controlling the flow rate of the group III precursors, at complete pyrolysis efficiency, give direct control of the vapor phase composition. The complete decomposition of TMIn and TMGa happens at low temperatures of 350°C and 475°C, respectively [78]. The low temperature needed to decompose TMIn makes it possible to grow InGaAs at lower temperatures. Lowering the temperature reduces the migration length of In atoms on the surface and this is believed to suppress the transition to island growth mode. In this study we chose a growth temperature of 580°C for the InGaAs QWs and GaAsP barriers. In order to grow the barriers at the same temperature as the QWs, to avoid long growth interrupts, TBP was used instead of PH_3. Very high temperature, greater than 850°C, is required for full PH_3 pyrolysis, while a much lower temperature around 450°C is required for TBP [78]. The incomplete pyrolysis of PH_3 at low growth temperatures makes the solid composition x_s highly non-linearly dependent on the vapor phase composition x_v. Since pyrolysis of TBP is achieved at lower temperatures, control of the As/P ratio is more linearly dependent and higher P-concentration can more easily be achieved [78]. AlGaAs growth was done at higher temperatures (720° for the DBRs) in order to suppress the presence of oxygen which would otherwise result in poor layer quality.

3.1.1 InGaAs MQW

To increase the emission wavelength from InGaAs QWs the In-content and or the QW thickness should be increased. Fig. 3.1 shows the wavelength corresponding to the conduction band electron to heavy-hole bandgap. From the Matthews-Blakeslee theory

from another ingot would show a specular surface finish and high average PL across the full wafer.

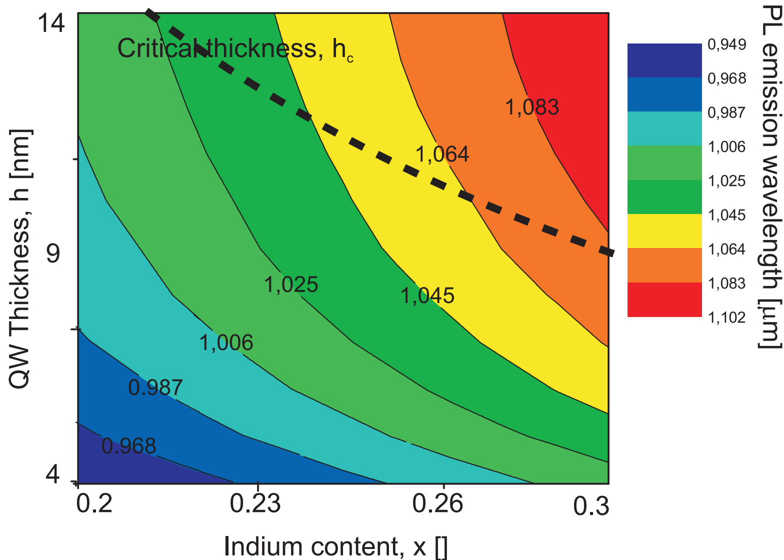

Figure 3.1: Contour plot of the PL emission wavelength as a function of In-content and QW thickness. The dashed line show the critical thickness with $m = 2$.

the critical thickness, h_C, is given by

$$h_C = \frac{1-\nu}{1+\nu} \frac{a_{\text{GaAs}}}{m\sqrt{2}\pi|f|} \left(\ln \left(\frac{\sqrt{2}h_C}{a_{\text{GaAs}}} \right) + 1 \right) \tag{3.1}$$

where a_{GaAs} is the lattice constant of the GaAs substrate, ν the Poisson ratio, f the lattice mismatch and m is 1, 2 or 4 depending on whether the thin film is a single layer, embedded in the substrate or part of a multilayer structure [79, 80]. In order to arrive at Eq. (3.1) we have assumed a burgers vector of $b = a_0/\sqrt{2}$, a misfit dislocation angle of $\alpha = 60°$ and slip direction $\lambda = 0°$ relative to the $\{111\}$ plane. Fig. 3.1 shows that it should be possible to increase the emission wavelength beyond 1060 nm with an In-content above 25%. This is close to the thickness at which the strain is accommodated by misfit dislocations. Increasing the In-content is by itself a challenge since high strain limits the incorporation of In to around 30% at 650° [81]. Growth to thicknesses close to the critical thickness predicted by the Matthews-Blakeslee theory have been shown possible [74]. This can be done by supressing the formation of misfit dislocations that forms the basis of the Matthews-Blakeslee theory.

There are two distinct strategies undertaken in order to push the PL emission to longer wavelengths: 1) decrease misfit dislocation formation, 2) reduce the effective strain. In the first case GaAs is used as a lattice-matched barrier material, while in the second case GaAsP is used as a strain-compensating barrier material due to its opposite (tensile) biaxial strain. Common to both approaches is that in order to limit transition from 2D to 3D growth (island nucleation) it is generally accepted that a low growth temperature, high growth rate and V/III ratio[2] should be used in order to lower the In migration/diffusion length [76]. Lowering the migration length of In suppress the coalescense of In-rich clusters. For the first case the low growth temperature furthermore suppress the relaxation of misfit dislocations. High growth temperatures are on the other hand associated with better crystal quality. For the second case a phase separation can occur due to the presence of both InGaAs and GaAsP. The lower the temperature the larger is the miscibility gap [82]. To avoid the phase separation associated with the miscibility gap the growth should be driven far from thermodynamic equilibrium. High growth rates together with high V/III ratio can be used in order to suppress phase separation.

We have succeeded in growing high-quality 5MQW active material using the Zero Net Strain (ZNS) approach where the tensile strain of the GaAsP barrier layer compensate the compressive strain of the InGaAs active layer according to

$$\epsilon_{\mathrm{QW}} d_{\mathrm{QW}} - 2\epsilon_{\mathrm{Barrier}} d_{\mathrm{Barrier}} = 0 \tag{3.2}$$

where ϵ and d are the biaxial strain of the QW and barrier thickness, respectively. For $In_{0.3}Ga_{0.7}As$ the compressive strain is $\epsilon_{xxyy} = 2.1\%$ and using $GaAs_{0.8}P_{0.2}$ with a tensile strain of $\epsilon_{xxyy} = 0.7\%$ the ZNS condition for $d_{\mathrm{QW}} = 8$ nm is reached with $d_{\mathrm{Barrier}} = 23$ nm. In order to achieve strain balancing the growth time for the GaAsP barriers was tuned according to the P-content fitted from the XRD measurement of InGaAs/GaAsP calibration growths.

The solid composition of $GaAs_{1-x}P_x$ is highly dependent on the vapor phase ratio between AsH_3 and PH_3 for low temperatures $<$

[2] In this text we define the V/III ratio in terms of the molar flow rates at the chamber inlet. The V/III ratio is an often used variable that albeit not saying anything of the partial pressure at the surface it the actual parameter we control.

650 °C. Since the GaAsP strain-compensating barrier layers are grown at the same temperature as the InGaAs QW (580°); this favors TBP, which show a reduced dependence on the vapor phase composition of the group V [78]. The best results for the barrier $GaAs_{0.8}P_{0.2}$ in terms of surface quality was achieved by using TBP as precursor with the same growth rate as the QW.

A screening experiment for the InGaAs QW in terms of the growth temperature together with the TMIn and AsH_3 flow rates was done. From this screening experiment two trends were seen. First lowering the temperature was required to avoid In segregation in the QW which resulted in a shoulder on the long-wavelength side of the PL peak. Secondly increasing the growth rate and V/III ratio increased the PL intensity. While the positive effect of increasing the growth rate can be understood in terms of the suppression of phase separation the positive effect of the V/III ratio is not well understood. The optimum growth parameters was found to be a growth rate of 8 Å/s and a V/III ratio of 150. Increasing both the growth rate and the V/III ratio at the same time is limited by the maximum AsH_3 flow rate. Lowering the growth rate would allow the V/III ratio to be increased, which has been used in InGaAs growth with GaAs barriers [74]. For GaAsP strain-compensated barriers we have found island nucleation at low growth rates of 2 Å/s. Fig. 3.2 shows the rocking curve from an XRD measurement around the Bragg angle of the GaAs substrate together with the PL intensity spectrum (inset) of a ZNS 5MQW $In_{0.3}Ga_{0.7}As$ test growth. The clear superlattice fringes seen on the rocking curve is a sign of sharp layer transitions. The superlattice peak FWHM is 120".The period of the superlattice modulation peaks at the left side of the substrate peak corresponds to a thickness of 27.5 nm. The inset shows the room-temperature PL spectrum with at peak intensity at 1071 nm and 29 nm FWHM.

3.1.2 VCSEL

Si-doped $Al_{0.9}Ga_{0.1}As$/GaAs n-DBRs was grown as bottom mirrors. The high Al-content gives a moderate refractive index contrast, while still being low enough for the oxidation rate to be orders of magnitude lower than the oxidation layer ($Al_{0.98}G_{0.02}aAs$). The GaAs is grown at 13 Å/s and the $Al_{0.9}Ga_{0.1}As$ at 9 Å/s. In order to

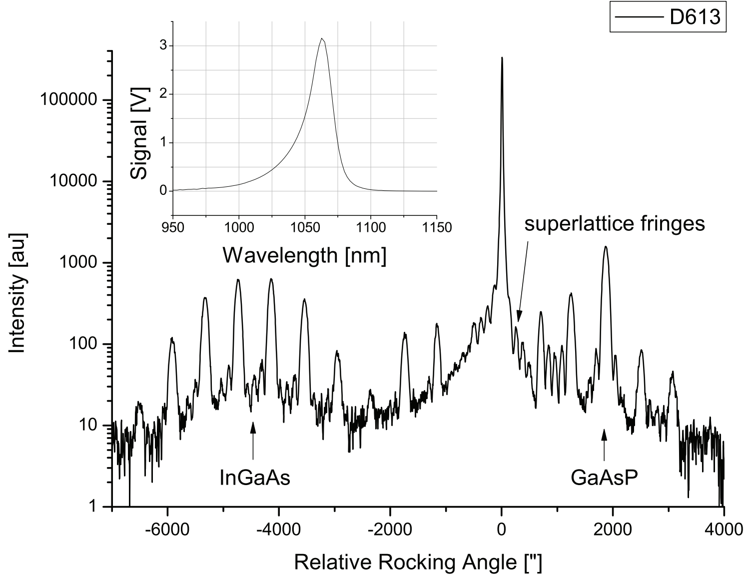

Figure 3.2: Plot of the rocking curve for a ZNS 5MQW $In_{0.30}Ga_{0.70}As$ with $GaAs_{0.83}P_{0.17}$ barriers (no cladding). The InGaAs/GaAsP superlattice thickness is 31.8 nm. The inset shows the PL intensity with a peak at 1063 nm and 21.7 nm FWHM (24 meV).

calibrate the growth rate a 11.5 pair $Al_{0.9}Ga_{0.1}As$/GaAs DBR was grown and the reflectance spectrum fitted using the TMM. From such a growth and fit routine the growth rate can be determined to within ± 0.5 Å/s. The fitting routine was based on fixing the refractive index and only varying the thickness[83]. As cladding layer GaAs was chosen since it can be grown at higher crystal quality at the low temperatures used for the MQW growth than $Al_{0.3}Ga_{0.7}As$ - which on the other hand would give better carrier confinement. The MQW and cladding are un-doped in order to limit absorption losses. A 55 nm $Al_{0.98}Ga_{0.02}As$ oxidation layer was placed close to the field anti-node the exact position optimized to give the lowest threshold current by balancing optical confinement and scattering losses. The thickness of the oxide aperture layer was choosen such that the oxidatin rate would not depend on deviations in the grown thickness [84]. Above the oxide aperture layer the GaAs was doped $5\times10^{18}cm^{-3}$ in order to allow low-resistance current spreading. The

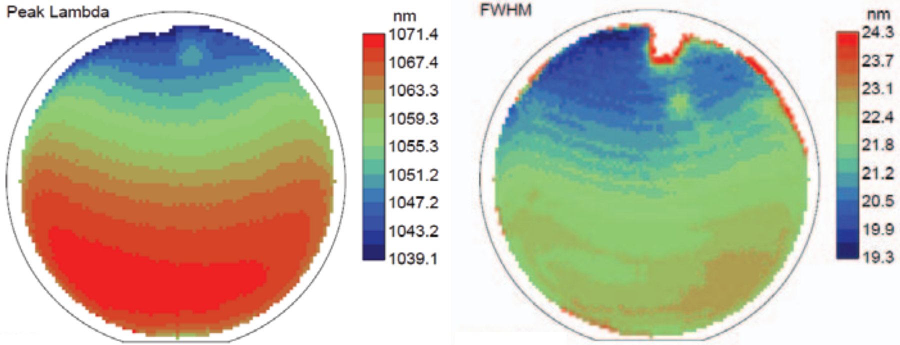

Figure 3.3: Plot of the **left:** PL peak wavelength λ, **right:** FWHM for a ZNS 5MQW $In_{0.30}Ga_{0.70}As$ with $GaAs_{0.83}P_{0.17}$ barriers (D613). The sample has been excited with a 532 nm CW laser and the PL measured using an InGaAs detector.

GaAs current spreading layer was followed by the InAlP sacrificial layer and the top Si-doped GaAs HCG layer. The epitaxial structure grown is shown in the results section 5.3 Figure 3.3 shows the peak wavelength and FWHM of a ZNS 5MQW $In_{0.30}Ga_{0.70}As$ test growth with $GaAs_{0.83}P_{0.17}$ barriers. The same growth parameters were used for the final HCG-VCSEL growth. The average wavelength is 1062 nm with a standard deviation of 8 nm across the wafer. The wafer surface is specular and the surface planar with a very low density of growth defects. Fig. 3.4 shows the measured and simulated XRD of the full epitaxial structure. The InGaAs/GaAsP superlattice is clearly visible and the fitted values are close to that of the test growth, see Fig. 3.2. The pendelösung fringes splitting the GaAs substrate peak originates from the AlGaAs/GaAs superlattice. The good agreement between the simulated and measured XRD with regard to the epi-design parameters shows that good layer control has been achieved. The inset in Fig. 3.4 shows the fitted values of the simulation where the thickness and composition has been fixed for all layers except GaAsP and InGaAs.

3.1.3 InAlP

$In_{1-x}Al_xP$ was grown using PH_3, TMIn and TMAl. In order to achieve lattice-matching to the GaAs substrate the composition

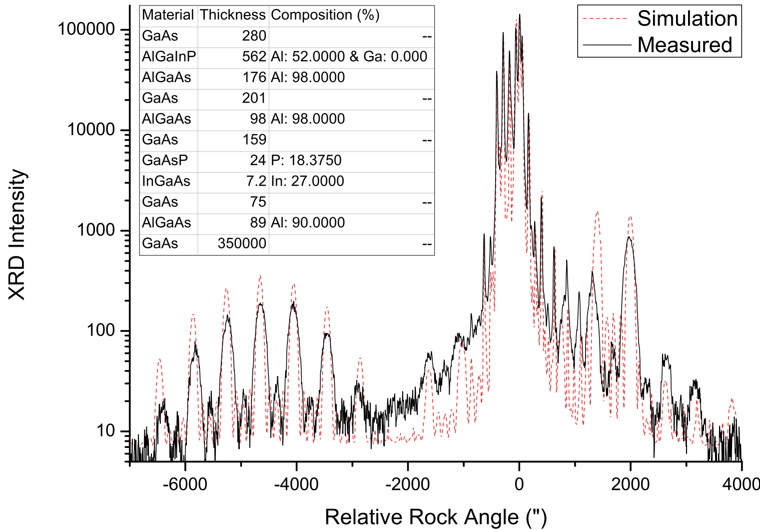

Figure 3.4: Plot of the XRD of the full epitaxial HCG-VCSEL structure.

should be $In_{0.48}Al_{0.52}P$. The InAlP was grown at temperatures from 610 °C to 700 °C. Comparing growths at 610, 650 and 700 °C all had a specular surface. Hence we are able to grow InAlP with good surface morphology at low growth temperatures [85]. The growth temperature was fixed to 610 °C to match the growth temperature of the MQW. Fig. 3.5 shows the peak separation measured from XRD on test growths of 530 nm InAlP capped with 280 nm GaAs. The right axis shows the corresponding lattice mismatch - which was calculated from the differential form of Bragg's law

$$\frac{\Delta a}{a} = -\cot(\theta_{\mathrm{B,GaAs}})\Delta\omega_{\mathrm{GaAs-InAlP}} \tag{3.3}$$

where a is the substrate lattice constant, Δa the lattice mismatch, $\theta_{\mathrm{B,GaAs}}$ the substrate peak and $\Delta\omega_{\mathrm{GaAs-InAlP}}$ the epi peak separation. From Eq. 3.1 we estimate the required lattice mismatch for growing a 530 nm thick InAlP layer, free of threading dislocations, to $< 0.5 \times 10^{-3}$. From Fig. 3.5 it is seen that the Al-content should be controlled to within 0.2 % in order to achieve such low lattice mismatch. Since the InAlP is to be used as a sacrificial layer we do not need to be concerned with the amount of threading dislo-

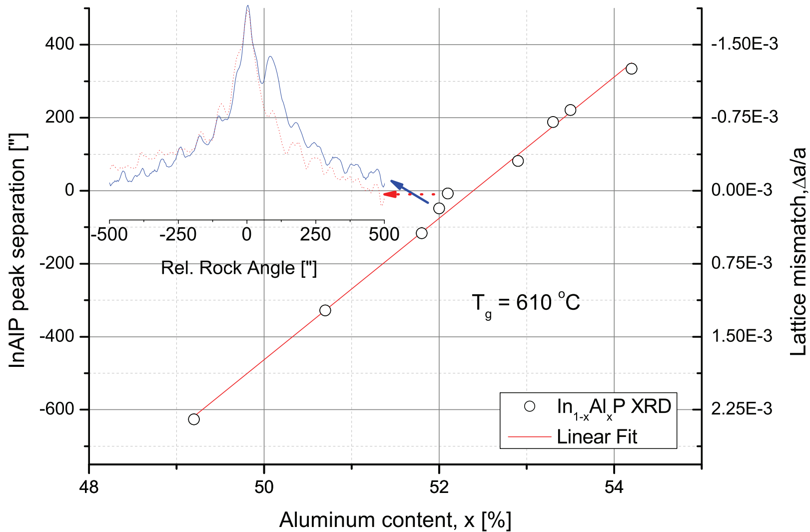

Figure 3.5: Plot of the aluminum content, x, and epilayer peak separation for $In_{1-x}Al_xP$. The inset shows the relative intensity of the x-ray diffraction measurement versus rocking angle relative to the GaAs Bragg Angle $\theta_{\mathrm{B,GaAs}} = 33.03$.

cations, but it gives an idea of the lattice match needed in order to avoid strain effects manifesting during growth. The growth of InAlP was found to be sensitive to the underlying structure with hillock formation (believed to be segregation of In) resulting from growth on rough surfaces.

3.2 Sacrificial release etch

A critical process step is the sacrificial release of the mechanical structure, which forms the cavity air-gap. A sacrificial layer acts as a place-holder at the desired position of the air-gap during processing. At the end of the device processing the sacrificial layer is etched away, thus leaving behind the desired air-gap. This kind of semiconductor processing has been known for more than 50 years [21].

The sacrificial layer can either be deposited onto the epitaxial

substrate or grown during the epitaxial process. The advantages of the first approach, which is well-established, is that the sacrificial layer can be deposited independently of the underlying substrate. The advantage of the monolithic sacrificial layer is that the layers above can maintain their crystal structure. This is important for applications where e.g. the piezo-electric properties depend on the zinc-blende crystal structure such as is the case for $Al_xGa_{1-x}As$ [86].

3.2.1 General considerations

For devices based on GaAs substrates there is a large variety of ternary compounds that can be used for sacrificial etching [87]. Since we would like the thickness of the sacrificial layer to be a free parameter, the ternary compound must be lattice-matched to GaAs. The thickness required for Fabry-Pérot cavity devices range from around a fourth of the wavelength to one or more multiples. AlGaAs can be lattice-matched to GaAs over the entire composition range and is therefore widely used as sacrificial material [88]. $Ga_{0.51}In_{0.49}P$ is also lattice-matched to GaAs and have been used for sacrificial etching, in particular where an Al-free material system is desired [89]. The last candidate taking into account the lattice-match criteria is $In_{0.49}Al_{0.51}P$, which thus far has not been used for sacrifical etching to the authors knowledge [90]. Hydroflouric acid is favoured for etching of $Al_xGa_{1-x}As$ where $x \geq 0.5$, showing high etch-rates and selectivities at the same time [88]. Hydrochloric acid (HCl) has been reported for sacrificial wet etching of both $In_{0.49}Al_{0.51}P$ and $Ga_{0.51}In_{0.49}P$ selectively to GaAs[90, 91]. The good etching properties of both compounds in HCl is likely to be rooted in both $AlCl_3$ and $GaCl_3$ to be soluble in water. The greater affinity of $AlCl_3$ to water, compared to $GaCl_3$ might also account for the higher etch-rate of $In_{0.49}Al_{0.51}P$. The etch-rate of $In_{0.49}Al_{0.51}P$ in concentrated 37% HCl is five times higher that that of $Ga_{0.51}In_{0.49}P$ [92, 91]. The lateral etch-rate of $Ga_{0.51}In_{0.49}P$ has been reported for different crystallographic orientation, while this is not the case for $In_{0.49}Al_{0.51}P$ where only the bulk properties has been examined [89]. Selectivity to GaAs is of interest in VCSELs for 1060 nm and above, but at lower wavelengths such as 850 nm Al_xGa_{1-x} would be favoured due to its lower optical

	GaAs	InGaAs	AlGaAs	InAlP	GaInP	AlO_x
$C_6H_8O_7$:H_2O_2	E [93]	CD [94]	CD [95, 96]	S		S
HCl:H_2O	S	S	CD [97]	E [90]	E [89]	E
HF:H_2O	S		CD [98]	E		E
NH_4OH:H_2O_2	E		CD [99]			(E)

Table 3.1: Etchant selectivity for the materials present in the material system used for the HCG-VCSEL . E = Etches, CD = composition dependent, S = Slow (≈ 1-10 nm/min).

absorption compared to GaAs. Anhydrous (water-free) citric acid ($C_6H_8O_7$) mixed with hydrogen peroxide (H_2O_2) and ammonium hydroxide (NH_4OH) has been used for etching of GaAs selectively to $Al_{0.15}Ga_{0.85}As$ with selectivities up to 100[93]. Since we focus on 1060 nm VCSEL the use of citric acid is not an option.

Tab. 3.1 summarizes the etch properties of selected binary and tenary semiconductor compounds, together with the oxide of aluminum, for different etchants. From the table it is seen that etching in HCl:H_2O stops on GaAs, while both $In_{0.49}Al_{0.51}P$ and $Ga_{0.51}In_{0.49}P$ are etched. AlO_x also etches in HCl:H_2O, but with a selectivity of 1:50 towards InAlP. The metal stacks (Ti,Pt,Pd,Au) will not etch in HCl due to the lack of an oxidizing agent. Since HCl has been reported to show complete selectivity to GaAs it was chosen for further investigation [87].

3.2.2 InAlP sacrificial etch

For this work we choose to focus our efforts on $In_{0.49}Al_{0.51}P$ as sacrificial material given its high etch rate as compared to $Ga_{0.51}In_{0.49}P$. This is an advantage in the sacrificial release of "large" structures such as Fabry-Pérot filters where the minimum size is restricted by focusing of the optical beam spot size.

In order to test the etching characteristics of InAlP using HCl, in particular the dependence on crystal direction, samples with GaAs/InAlP layers were masked with the positive UV-resist AZ5214E. The pattern was transferred to the GaAs using dry etching and the sample was then etched in HCl at different concentrations. The etch rate in different directions was measured from 40 μm squares using differential contrast imaging (DIC) to see the undercut of the GaAs. The direction was measured relative to the major flat to which the

pattern was aligned. This means that there is an uncertainty of around 3° on the direction with regards to the major crystal axis as given by the specifications on the GaAs wafer. Alignment to a cleaved flat or etched pits could remove this uncertainty.

3.2.3 Results

It has been found that the wet etching of $In_{0.49}Al_{0.51}P$ in $HCl{:}2H_2O$ is limited by {111} planes that etch by 0.5 μm/min at 22°C. The etch-profile is typical of anisotropic reaction-limited etching with a slope of 55° corresponding to the angle of the $(1\bar{1}1)$ to the (100) surface. The observed crystallographic dependence match the expected behavior stopping at the column III-terminated (111) surfaces where the rate-limiting In/Al atom have 3 backbonds and 1 dangling bond. It is widely reported that HCl does not etch GaAs, since etching of GaAs is normally mediated by an oxidizing agent [90]. When using diluted HCl for etching, H_2O can act as an oxidizing agent, forming Ga_2O_3, and although the oxidation rate is very low ($\approx$ 0.5nm/hr for pure H_2O) it can significantly increase when the pH-value of the mixture is lowered[100]. This could explain the slow etch rate of 2 nm/min of GaAs in the [110]-direction by $HCl{:}2H_2O$ observed in device processing. Although this is 250 times slower than the etch rate of $In_{0.49}Al_{0.51}P$, the dimension of the HCG patterns etched in GaAs are also around 25 times smaller.

Another concern is etching of Al-containing layers, in particular the oxidized AlGaAs. The reactive nature of aluminum makes it difficult to avoid any reaction, but one advantage is that the aluminum oxide is more resistant to wet etching. Experiments where epitaxial layers of $Al_{0.9}GaAs$ were exposed show selectivity of 1:5 when compared with InAlP, while in the case of AlO_x lateral etching of AlO_x (sandwiched in between GaAs) was not observed. Fully exposed thin films of AlO_x, on the other hand, showed a selectivity of 1:50. It has been reported that $Al_xGa_{1-x}As$ will be etched by conc. HCl for $x \geq 0.3$[97]. Here we have not seen etching of $Al_{0.98}GaAs$ in $HCl{:}xH_2O$ with $x > 2$ during device processing. This makes the use of $Al_{0.51}In_{0.49}P$ viable as sacrificial material in device processing of AlGaAs-based 850 nm HCG-VCSELs. Fig. 3.7 shows a scanning electron micrograph (SEM) of fully released cantilevers. The sacrifical etching was done using $HCl{:}2H_2O$ and critical point

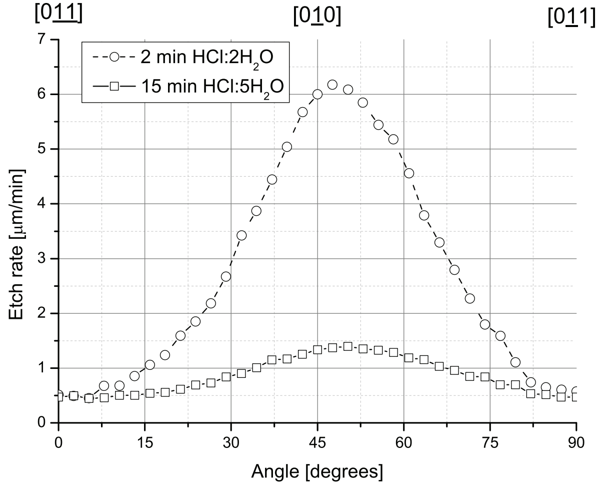

Figure 3.6: Etch rate (μm/min) as a function of the crystal direction normal to the plane being etched. The graph shows the etch-rate for HCl diluted to water and 5 times water, respectively.

drying. The slight curvature of the cantilever apparent in the inset could indicate either a difference in the surface properties of the top and bottom surface of the cantilever (leading to different water condensation behaviour) or that another material remains at the bottom surface. SEM of completely released HCG-VCSEL top mirrors (curled up due to the stress of the gold contacts) do not show any residues, why it is postulated that the slight bending is due to different surface wetting. The cantilever test structures are are an order of magnitude longer than the HCG VCSEL, where height measurement by confocal microscopy show perfect flatness.

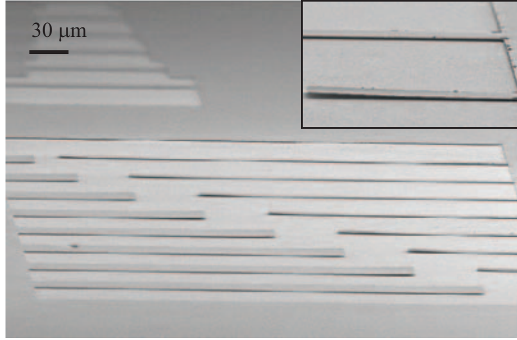

Figure 3.7: Scanning electron micrograph (SEM) of cantilever beams released using HCl:2H_2O and critical point drying. The beams are up to 350 μm long and 0.28μm thick. The beams to the right and left are 10 and 40 μm wide, respectively. The inset shows a free-hanging cantilever (the electrons are not reflected from the empty space underneath). The airgap is 0.5μm.

3.3 Grating pattern transfer

Apart from the establishment of a process for the sacrificial release of III-V structures in GaAs, another focus of the process development has been the grating patterning. The following section will go through the results of the different mask and dry etching combinations to provide an overview on this part of the work. The first III-V dry etching process established at the cleanroom facility was RIE using flouroform (CHF_3) and methane (CH_4) for etching of silicon oxide (SiO_2)/silicon nitride (Si_3N_4) and InP/GaAs, respectively [101, 102]. The RIE is equipped with an quartz carrier and this results in significant heating of the photoresist which lowers the etch resistance and especially in the case of ZEP520a compromise the resist structural stability [101]. During the project Inductively Coupled Plasma (ICP) was installed and the GaAs etching process was transferred from the RIE to the ICP. This meant an increase of the grating pattern etch rate from 9 to 160 nm/min. This is facilitated by the decoupling of the plasma generation and the substrate bias in the ICP allowing for very high powers to increase the radical density, while keeping both the pressure and substrate bias power low. In this way the etch-rate is significantly increased without the physical etch increasing as would be the result of increasing

Bias		Flow		Pressure
Coil [W]	Platen [W]	Cl_2 [sccm]	Ar [sccm]	[mTorr]
800	70	4	12	6

Table 3.2: ICP GaAs Nano etch

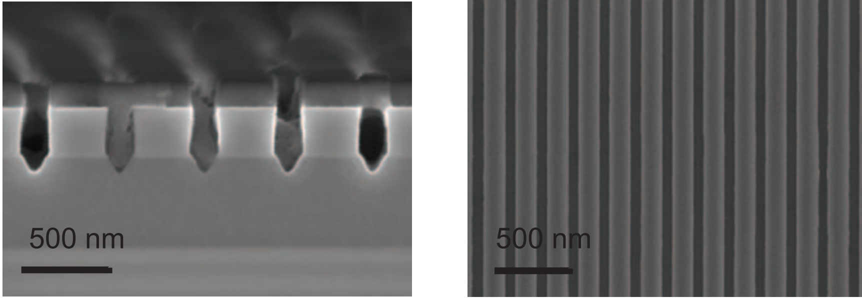

Figure 3.8: Scanning electron micrographs of the nano patterning **left:** after pattern transfer from the positive electron beam resist (ZEP520a) to the Si_3N_4 **right:** after sacrificial etching.

the plasma density in a RIE system by increasing the substrate bias. Table 3.2 shows the etch recipe used for etching GaAs grating patterns. This etch was optimized for etching holes with vertical side-walls in GaAs photonic crystal structures. The etch-rate of GaAs was approximately 300 nm/min, but due to the aspect-ratio dependent etching (ARDE) effect the etch-rate of the grating pattern was around a factor of two lower.

3.3.1 Si_3N_4 mask

In the first batches the e-beam resist ZEP520a was used to transfer the HCG pattern into a 180 nm Si_3N_4 hard mask, which was then used to transfer the pattern to the 0.28μm thick GaAs[3]. ZEP520a is a positive e-beam resist and thus only the air spacing of the HCG is written. The pattern transfer into Si_3N_4 after ZEP520a resist development was done by RIE. A CHF_3/O_2 dry etch was used at an etch rate of 17 nm/min. For the pattern transfer into GaAs a cyclic CH_4/H_2-based RIE with $(CH_2)_x$ passivation and a oxygen plasma

[3]The reason for using silicon nitride instead of silicon oxide was that a better selectivity to ZEP520a has been reported [101]

etch-back or a Cl_2/Ar-based ICP was used [101]. For the CH_4/H_2 RIE, the etch-rate of the grating structures was 9 nm/min, while it was 38 nm/min in larger areas, and the selectivity Si_3N_4:GaAs was 1:4 [102, 101]. The substrate was placed on a built-in quartz carrier with no active temperature control. The lack of substrate cooling means that the resist is heated during etching, which results in poor etch resistance (the selectivity being 1:1). Mask erosion during the long etches required to transfer the nanometer pattern into Si_3N_4 resulted in severe linewidth broadening on the order of 70 nm for 18 min etching. The linewidth broadening observed could be a combined effect of ZEP520a contraction due to charging and temperature effects together with mask erosion at the edges due to the physical component of the etch. Resist residues was observed to be a problem. This leftover resist at the bottom would negatively affect the pattern fidelity by blocking the etch of the GaAs[101]. The linewidth broadening could only be partly accountedfor by a linewidth reduction during e-beam writing. The reason is that the 600-nm thick ZEP520a, required to withstand the duration of the etch, also means significant forward scattering during e-beam writing, which limited the minium linewidth in the ZEP520a to around 40 nm. This makes the aspect ratio of the ZEP lines around 1:15, which helps to explain the factor of 2 in RIE lag encountered. In addition the sidewall curvature tampered the following pattern transfer. Opening up for fluoride-based etching on the ICP would make it interesting to use it for transferring the nano-sized patterns from the ZEP520a into a SiO_2 or Si_3N_4 hard mask allowing for much deeper etching. The selectivity of Si_3N_4:GaAs was found to be better than 1:10 for etching in the ICP.

3.3.2 ZEP mask

In order to overcome the limitations of the RIE etching of Si_3N_4, efforts were made to use ZEP520a directly on GaAs as enabled by ICP etching. The higher etch rates enabled by the high radicals density in ICP at lower platen power allowed ZEP520a to be used to transfer the pattern. The GaAs etch-rate was 300 nm/min with the etch-rate of the grating patterns being 160 nm/min and the ZEP520a:GaAs selectivity being 1:1. Due to the poor adhesion of ZEP520a on GaAs a thin SiO_2 adhesion layer was deposited before

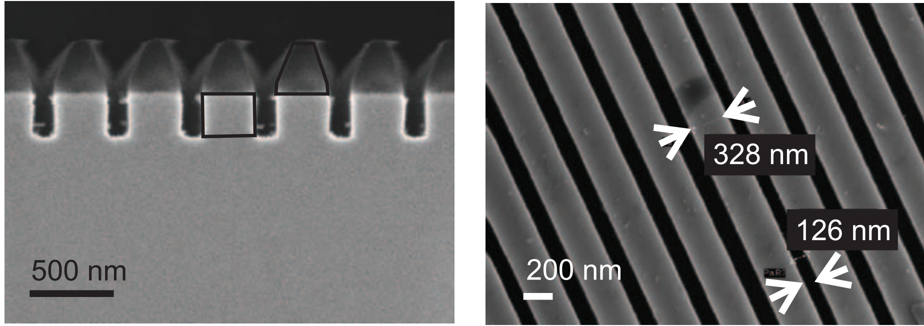

Figure 3.9: Scanning electron micrographs of the nano patterning **left:** before the positive electron beam resist (ZEP520a) has been removed and **right:** after the resist has been removed on the full epi-structure.

spinning ZEP520a. Fig. 3.9 shows the cross-section of part of the HCG before and after removal of the ZEP520a mask. In the left scanning electron micrograph (SEM) mask erosion of the ZEP520a is clearly visible. Before dry etching the ZEP520a sidewalls are vertical, but after dry etching they are slanted[4]. This is believed to be due to the strong physical component of the etch. The right picture in Fig. 3.9 shows the a topview of the HCG after the sacrificial etching. The GaAs sidewalls are perfectly vertical and the line edge rougness is very low. For too long etch duration it was seen that mask erosion would be transferred into the resist. This hindered long over-etching to ensure that the InAlP was reached. The selectivity between GaAs and InAlP was 1:3 - the lower etch rate of InAlP likely due to the low volatility of $InCl_3$ at the etch temperature of 20°. The InAlP is later fully removed, why overetching is not a problem in that regard. In order to increase the etch depth of GaAs, the selectivity should be improved by optimizing the etch in terms of pressure, platen and coil power. Another possibly simpler route is to simply decrease the platen temperature in order to reduce the heating of the ZEP resist[5].

[4]This is partly an artefact of SEM imaging. The heating induced will make the ZEP contract, which was confirmed by changing the exposure time in cross-sectional imaging. The kink in the resist is though believed to be related to the dry etch

[5]Heat transport from the sample to the carrier substrate was found to be very important and to that aim Crystal Bond™ was used to improve heat transfer. Applying Crystal Bond™ meant the difference between fully burned

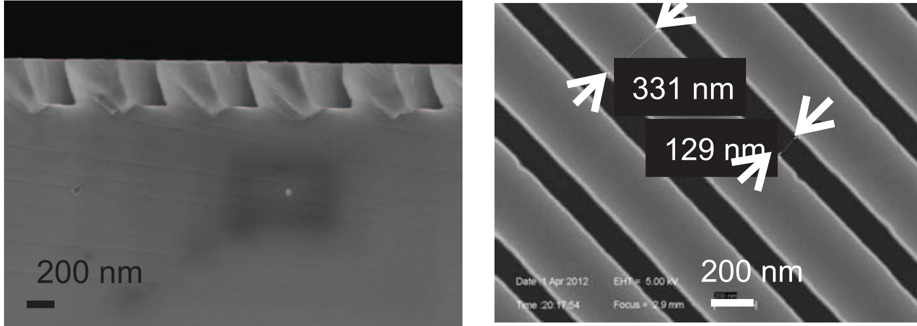

Figure 3.10: Scanning electron micrographs of the nano patterning after the negative electron beam resist (XR1541) has been removed **left:** in cross-section **right:** from above.

3.3.3 HSQ mask

For the HCG-VCSELs it was decided to use the negative e-beam resist hydrogen silsesqouioxane (HSQ). The negative resist HSQ can be cured into SiO_2 and thus should show good etch resistance during pattern transfer. Furthermore it is generally found that a hard mask, in the form of an oxide or nitride, yield a lower line-edge roughness compared to e.g. metals or photoresists. The smaller dimensions of the HCG both required better alignment of the grating to the mirror and allowed for shorter writing times. The big metal pads was written with a high current of 64 nA which was overlaid the grating pattern written by 10 nA. The selectivity of GaAs:HSQ was expected to be better than 1:10 but was found to be less than 1:7. A lower etch resistance of HSQ than SiO_2 is also what is reported elsewhere [103]. The selectivity is still much better than that of ZEP:GaAs and it should be adquate with a 100-nm HSQ mask in order to etch 350 nm GaAs. The results of etching GaAs with a 180 ± 10 nm HSQ mask is seen in Fig. 3.10. Smooth sidewalls result and the design duty cycle of 0.72 was achieved. Mask erosion was found to be a problem in obtaining smooth sidewalls, resulting in sidewall roughness on the order of 5-20 nm. The mask erosion was found to both depend on the HSQ exposure dose and development conditions. It has been observed that thick HSQ is necessary to avoid mask erosion being transferred to the substrate

ZEP (and thus failed dry etch process) or successfull pattern transfer.

in etching GaAs[103]. Increasing the resist thickness presents a trade-off since as the etch rate decreases the mask will be exposed to the same amount of erosion given the longer etching time that will be necessary to reach the same depth. Increasing the resist contrast by decreasing the soft bake temperature was found to decrease the mask erosion and this can be attributed to better curing of the resist (e.g. easier removal of non-cured resist).

3.4 HCG Fabry-Pérot filter

The starting epitaxial substrate for the HCG Fabry-Pérot filter fabrication consist of an n-doped DBR, $Al_{0.49}In_{0.51}P$ sacrificial layer and an n-doped GaAs HCG layer. Following the HCG pattern definition, the full mirror structure with bonding pads was transferred into the GaAs layer using positive AZ5214E resist lithography exposed by ultra-violet (UV) light. The alignment accuracy was within 1 μm on a quarter 2 inch sample. The top metal NiGeAu n-contact was patterned by lift-off lithography using a bi-layer resist scheme with 600-nm AZ5206 on 500-nm LOR5B. The LOR lift-off resist is stated not to scum, but a descum for 1 min in an oxygen plasma was found to be required [6]. The backside of the substrate was then polished using Chemlox (sodium hypochlorite) with a Chemcloth polishing pad in order to achieve a smooth surface, hence reducing light scattering at the interface. The backside was further coated with an anti-reflective coating (ARC) - either SiO_2 or SiO_2/TiO_2. The backside must be protected with photoresist during sacrificial release, since it was found that the ARC disintegrate. The NiGeAu n-contact was alloyed using rapid thermal annealing at 420 °C for 10 seconds[104]. The last step was the sacrificial etching of the InAlP to define the air-gap with critical point drying to avoid stiction.

3.5 VCSEL processing

Standard oxide confined VCSELs with n- and p-doped DBRs were processed in order to benchmark the InGaAs MQW. In the first

[6] Scum refers to insoluble resist left after development. This is often removed with O_2 plasma ashing, which is also referred to as descumming.

photolithographic step AZ5214E is used as a hard-baked mask to wet etch the oxidation mesas using $1H_3PO_4$:$4H_2O_2$:$45H_2O$. In order to improve the adhesion of the photoresist, a 100 nm thick SiO_2 layer is first deposited by PECVD in order to take advantage of the superior adhesion of AZ5214E to HMDS treated SiO_2. After the mesa etching the $Al_{0.98}Ga_{0.02}As$ oxidation layer is oxidized by 440°C wet oxidation. The aim was to oxidize to a 5-μm oxide aperture. The oxidation process requires very good uniformity and composition control of the AlGaAs layer which was not established at the time of writing. This means that the oxidation rate varies widely across the wafer due to differences in Al-content [84]. Just before oxidation the oxide adhesion layer is wet etched in buffered hydroflouric acid (BHF) in order to avoid it covering the oxidation layer. After wet oxidation the surface is coated with SiO_2 and planarized using BCB. The BCB is etched back, after hard-curing, using O_2/CHF_3 based RIE at an etch rate of 140 nm/min. End-point detection is used to stop at the SiO_2 which functions as the isolator beneath the top diode contact. An opening is made in the SiO_2 on the mesa by BHF wet etching and a Ti/Pt/Au metal stack patterned by lift-off using a bi-layer resist scheme. In order to improve the formation of an ohmic contact deoxidation of the surface is done using HCl:H_2O. In the same manner the backside is deoxidized and degreased in NH_4OH:$10H_2O$, with the frontside being covered by hard-baked AZ5214E photoresist[7]. This is then followed by blanket deposition of an Ni/Ge/Au metal stack. The last step is a rapid thermal alloying at 420°C for 10 s to form ohmic contacts.

3.6 HCG-VCSEL processing

The starting substrate for the HCG-VCSEL processing is covered in Sec. 3.1.2. Due to the much smaller mirror dimension for the HCG-VCSEL the HCG and mirror layout, including contact pad, was patterned in a single step using the negative resist HSQ. Figure 3.11 shows SEM of HCG before sacrificial etching. The left SEM shows that good pattern fidelity has been achieved. The right SEM

[7]This step is not necessary in the case that the sample is lapped down in AlO_x

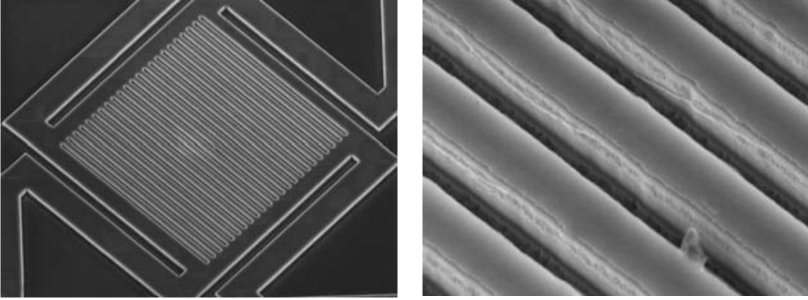

Figure 3.11: SEM of the **left:** HCG of the VCSEL and **right:** close-up on the HCG grating. The wafer is tilted 15° to show the sidewall roughness. The HSQ mask has not been fully removed and is seen as a thin layer on top of the grating bars.

shows a tilted view of the grating with the HSQ still on top. Limited sidewalls roughness is seen. The exact same parameters as in Fig. 3.10 was used and the difference in sidewall roughness shows that the process is not completely stable. In the next step the p-doped GaAs is reached by wet etching using positive UV lithography (the resist protecting the HCG). This is then followed by pattern definition of the oxidation mesa using wet etching - again with positive UV lithography. This step also defines the contact mesa for the p-contact. To confine the current to the same area as the HCG and to ensure single-mode lasing, an oxide aperture is defined by oxidation of an $Al_{0.98}GaAs$ layer in a steam ambient furnace at 440°C. Figure 3.12 shows the PL peak and FWHM of the fourth quater after the wet oxidation. The median peak wavelength is 1048 nm with a 19 nm FWHM. This is a 10 nm blue-shift relative to the test MQW growth. An explanation of this blue-shift (apart from simple reactor drift) could be quantum well intermixing during the growth of the AlGaAs oxidation layers, which is done at 720°. The PdGeTiPtAu top contact is patterned using lift-off with image reversal of AZ5214E after which the NiGeAu backside contact is deposited. In order to simplify the contact lithography the same metal stack has been used for both the top MEMS n-type and laser diode p-type layers [105]. The contacts are alloyed in a single step rapid thermal annealing at 420°C for 15 s. After alloying the contacts the air-gap is defined by sacrificial etching of the InAlP using critical point drying to avoid stiction.

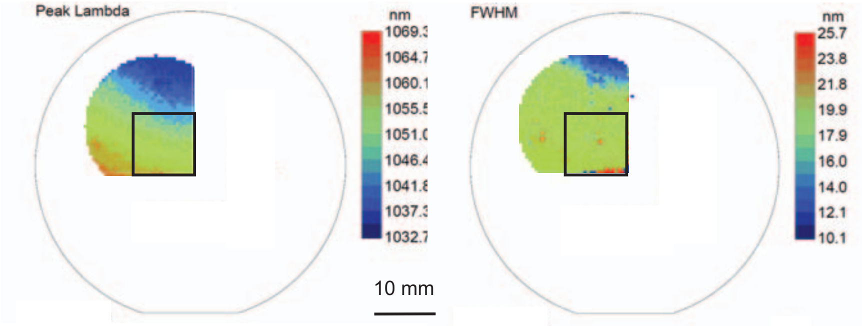

Figure 3.12: Plot of the PL peak and FWHM of the processed HCG-VCSEL after wet oxidation.

3.7 Summary

Process flows for the realization of electro-static tunable HCG Fabry-Pérot filters and HCG VCSELs have been developed. This has involved work on all aspects of the process, from epitaxial growth to sacrificial wet etching. MOVPE growth of 1060 nm MQW $In_{0.3}Ga_{0.7}As$ active material with strain balancing has been developed. Good material quality has been achieved with the InGaAs/GaAsP MQW showing well-defined x-ray diffraction superlattice peaks with 120" FWHM and photoluminesence with 20 nm FWHM. Furthermore growth of lattice matched InAlP has been characterized together with the crystallographic dependence of the etchrate in diluted HCl. Based on the MOVPE grown laser material standard oxide apertured VCSEL with 25/35 top/bottom DBR pairs have been fabricated and tested. A large part of the process development has also been the investigation of different mask and dry etch techniques to transfer nanometer patterns defined in e-beam resist. The best results have been achieved by transferring the pattern of the e-beam resist HSQ directly to GaAs by ICP etching. In general it is noted that mask erosion is an issue in transfering patterns with a critical dimension < 100 nm. Based on the InAlP sacrificial etch and nanopatterning, HCG VCSEL have been fabricated and tested.

Chapter 4

Fabry-Pérot filter results

In this chapter the results on the Fabry-Pérot filters are presented. Fabry-Pérot filters based on AlGaAs/GaAs epitaxy was demonstrated in 1995 with a relative tuning range of 7.5% at moderate voltages [57, 106]. Large-signal modulation at frequencies up to 150 kHz have been demonstrated using a DBR pillar as the top mirror, which decouples the reflectivity from the mechanical design [70]. Few examples exist in literature on Fabry-Pérot filters with high-index contrast subwavelength gratings. From a conceptual point of view the ideal structure would consist of a Fabry-Pérot cavity with two HCG mirrors. This would ensure a high finesse, low transmission loss Fabry-Pérot filter. HCG Fabry-Pérot filters has been demonstrated in the AlGaAs/GaAs system with a Q-factor of 40 for an air-gap cavity [107]. Similar finesse has been demonstrated in the AlGaAs/GaAs system with a top HCG mirror and bottom DBR mirror sandwiching an oxide cavity [108]. A Q-factor of 1047 has been demonstrated in the InP/InGaAs system with a top HCG mirror and bottom InP/air DBR with an air-gap cavity [109]. The latter work demonstrates that high finesse can be achieved with a HCG-DBR Fabry-Pérot filter. The structure pursued here is similar to that of [109] et. al. with the difference that a solid bottom DBR is used.

4.1 Transmission measurements

The filters are intented for use as transmissive filter and has been tested as such. The characterization of the filter was done by using

a white-light source and a Optical Spectrum Analyzer (OSA) to look at the transmission spectrum. The HCG is highly polarization dependent and therefore the polarization state of the input light was made linearly polarized.

4.1.1 Fiber-based setup

The transmission measurement setup consists of the following: a SuperK™ white-light source, a Glan-Thompson polarizer prism, a Neutral Density (ND) filter, a Polarization Maintaining (PM) fiber and a multimode (MM) fiber. The spectrum was measured using an OSA. The SuperK supercontinuum laser light source covers the full range of interest with the major drawback that the light is generated by a 1064 nm laser, which thus shows up as an artefact in the spectrum. The extinction ratio of the polarizer prism was found to be 13 dB measured by a power meter. The stress-rods of the fiber were misaligned $\sim 45°$ to the turn key, which has been accounted for in reading off the polarization angle from the polarizer prism. A 10 dB ND filter was used to lower the high output power from the light source (100 mW) which would otherwise melt GaAs[1]. The PM fiber was a photonic crystal fiber (PCF) with a large mode diameter of 9 μm. Assuming a Gaussian beam, the beam waist would be 13 μm for a propagation distance of 250 μm, which is smaller than the minimum mirror sidelength of 20 μm. In order to provide an absolute measure of the transmission, a reference measurement was done each time at the same distance between the 62.5 μm MM and 9μm PM fibers, as for the device measurements. Hence, the free-space loss due to the beam divergence is accounted for in the results as presented here. In order to align the PM fiber to the HCG, two microscopes were used. The sample was placed vertical to allow for easy coupling to the two fibers. One microscope allowed for a sideview of the sample, the slight tilting of which allowed to see the top metal contact. In this way the fiber could be aligned in one direction. For the other direction a microscope was placed to see the sample surface at an angle. In this way the spot could be seen on the sample.

[1]Luckily the amount of arsine that could escape is minute, but the device will nevertheless not survive

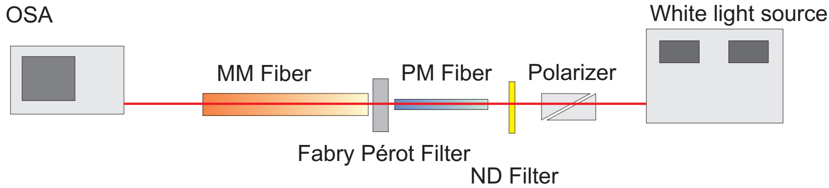

Figure 4.1: Sketch of the experimental setup used to characterize the Fabry-Pérot filter transmission. A polarizer controls the polarization state of the light which is coupled into a polarization maintaining fiber after attenuation.

4.1.2 Filter transmission

Fig. 4.2 shows the measured transmission spectrum of a Fabry-Pérot filter with 20 μm grating area for both TE and TM polarization (with respect to the grating direction). The spectrum for TE polarized light compares well qualitatively to the 30 pair n-DBR transmittance spectrum. The minimum transmittance of -30 dB is higher than the theoretically expected -34 dB assuming 5 cm^{-1} loss at a Si doping concentration of 10^{18}cm^{-3}. In order to match the measured transmittance the loss should be 20 cm^{-1} or equivalently a Si doping concentration of 4×10^{18}cm^{-3}. The measured transmission is close to the noise floor of the OSA why this is subject to some uncertainty. For TM polarization a peak transmission is seen inside the DBR stopband at 1027 nm with a FWHM of 4.4 nm. This makes the Q-factor of the filter 233. The difference between the transmission of the TM and TE polarized light is seen to be around 10 dB. A higher ratio would be expected, but to resolve this a polariser prism with a larger extinction ratio must be used. The reduction in transmission can arise from a high HCG reflectance, absorption loss or diffraction into higher order modes than the zeroth.

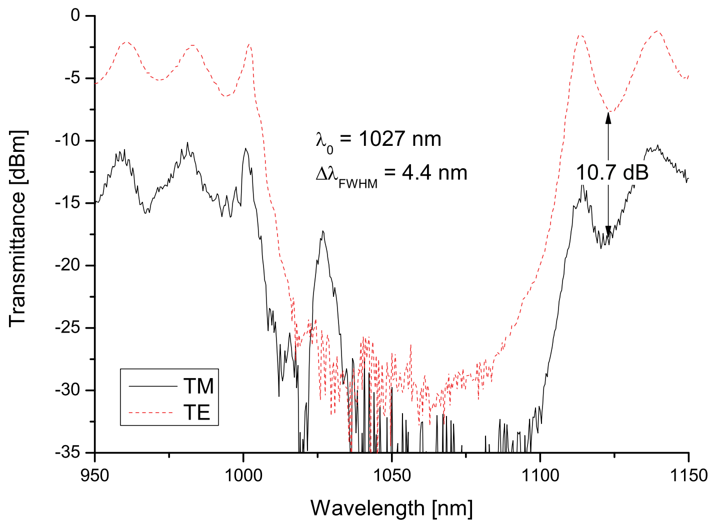

Figure 4.2: Plot of the filter transmission spectrum for a 20 μm HCG grating filter.

4.2 Discussion

HCG Fabry-Pérot filters have been fabricated and their transmission spectrum measured. Q-factor of around 200 has been measured, far short of the 15000 expected for such high-reflectivity mirrors. An explanation to the mismatch between the measured and expected Q-factor can be found in the analysis of Sec. 2.3 from which it was found that both the filter linewidth and transmission loss increases with decreasing mirror reflectance. Another source of optical loss, which would also degrade the Q-factor, would be beam walk-off. This beam walk-off effect on the optical Q-factor will depend on the mirror reflectance. An simpler method of measurering the HCG reflectance is warranted, e.g. measuring the reflectance of an oxide-gap HCG.

Chapter 5

VCSEL results

In this chapter we report on the results of the fabrication of 1060 nm VCSELs, which is presented in Sec. 5.2. A standard VCSEL structure with a semiconductor λ_0 cavity, top and bottom DBRs was made in order to test the gain material grown. Section 5.3 describes the characterization of a HCG VCSEL with a $\lambda_0/2$ air-gap and an air-clad HCG. Light-Current-Voltage (LIV) characterization was done for both VCSELs, and for the HCG VCSEL the MOEMS tuning was further tested. The measurements are the first for a HCG VCSEL with no p-doped top DBR mirrors.

5.1 Experimental setup

In order to measure the opto-electrical characteristics of the VCSELs a standard probe station setup was used. Needle probes were used

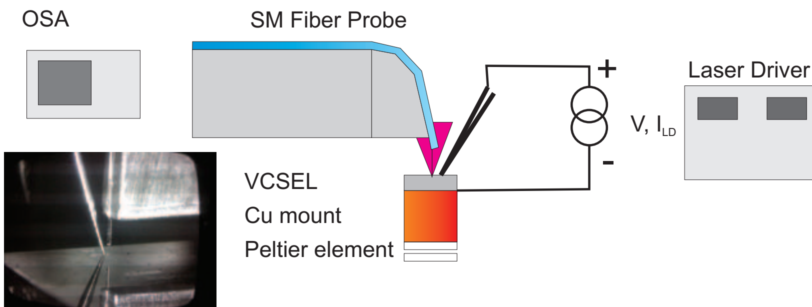

Figure 5.1: Sketch of the experimental setup used to characterize the VCSELs

for making electrical contact to the MEMS contact pad and the VCSEL p-contact pad. The VCSEL forward current was controlled by a laser driver (ILX LDC-3724) at constant current. The p-contact was used as the MEMS gnd contact to apply a positive floating potential difference to the MEMS contact using a DC Source Measurement Unit (HP6632A) or a Keithley High Current Source Measure Unit (238). For dynamic operation a Arbitrary Function Generator (HP33120a) was used with a +/- 15V amplifier and bias tee to set a DC offset to the AC signal. The output power was measured using a large-area Si photodiode (Thorlabs FDS1010) with a responsivity $\mathcal{R}$ of 0.6-0.2 A/W at 1000-1100 nm. The output power stated here are calculated using the responsivity data given by the manufacturer[1]. The uncertainty on the output power is $< 15\%$. The optical spectrum of the VCSELs was measured using a standard Single Mode (SM) telecom fiber (SMF-28) to collect the light. A peltier element together with a standard thermistor was used for temperature control of the sample holder. A sketch of the setup is seen in Fig. 5.1. The fiber probe was placed in close viscinity to the VCSEL using a power meter for optimizing the signal and a monitor to visually control the distance of the fiber to the sample.

5.2 VCSEL

5.2.1 Device structure

The epitaxial structure was designed as a λ_0 cavity with 25 and 35 pair top and bottom DBRs. The mirrors were doped to a constant level of approximately $2 \times 10^{18}\text{cm}^{-3}$. In the first layer of the top DBR, the Al-content was increased to 98% such as to be oxidized to be the current aperture later on. The λ_0-cavity consisted of undoped GaAs cladding on both sides of the 3 MQW $In_{0.3}Ga_{0.7}As/GaAs_{0.8}P_{0.2}$. In order to be able to make ohmic contact to the top DBR the temperature was decreased to 580°C during the growth of the top GaAs layer. This should increase the doping concentration to $4 \times 10^{19}\text{cm}^{-3}$ allowing thermionic current transport.

[1] http://www.thorlabs.com/images/TabImages/FDS1010-CAL_xls.xls

Layer	Material	Periods #	Thickness [nm]	nL λ_0	Function
12	GaAs:C	1	76.0	0.250	DBR/Contact
11	$Al_{0.9}$GaAs:C	24	88.0	0.250	DBR low
10	GaAs:C	24	75.9	0.250	DBR high
9	$AlO_x/Al_{0.98}$GaAs:C	1	89.0	0.250	Oxide aperture
8	GaAs	1	109.3	0.360	Cladding
7	$GaAsP_{0.2}$	3	11.0	0.035	Barrier
6	$In_{0.3}$GaAs	3	8.0	0.026	QW
5	$GaAsP_{0.2}$	3	11.0	0.035	Barrier
4	GaAs	1	33.4	0.110	Cladding
3	GaAs:Si	35	75.9	1.670	DBR high
2	$Al_{0.9}$GaAs:Si	35	88.1		DBR low
1	GaAs:Si	1			Substrate

Table 5.1: Device structure of the VCSEL.

5.2.2 Laser characterization

The fabricated VCSELs were tested in terms of their optical spectrum and LIV characteristics. Fig. 5.2 shows the optical spectrum of a SM VCSEL at 1.5 to 3 times the threshold current of $I_{th} = 4$ mA. The optical spectrum was measured using a SM fiber to collect the light. The SMSR is 24 dB at $1.5I_{th}$ and remains 13 dB up to 20 mA. The lasing wavelength of 1056.5 nm is very close to the center photoluminescence wavelength of 1063 nm from the calibration epitaxial MQW growth (see Fig. 3.2). This indicates very good control of the cavity growth. The wavelength dependence on driving current is 0.25 nm/mA. The laser linewidth was more narrow than the limit of 0.1 Å on the spectrometer. Fig. 5.3 shows the LIV characteristic of a SM VCSEL. From Fig. 5.3 it is seen that the differential quantum efficiency is very low, around 1%. For the given design with 35 pair bottom DBRs and only 25 top DBRs all the power will be coupled out the top mirror, but due to the high loss of the p-doped top mirror only 43% will be coupled out. The mirror transmission loss can be estimated from TMM to be 19 cm^{-1} when the loss of the mirror is included in the total cavity loss $\langle\alpha_i\rangle$. Then assuming a quantum efficieny, η_i, of 0.8 the total

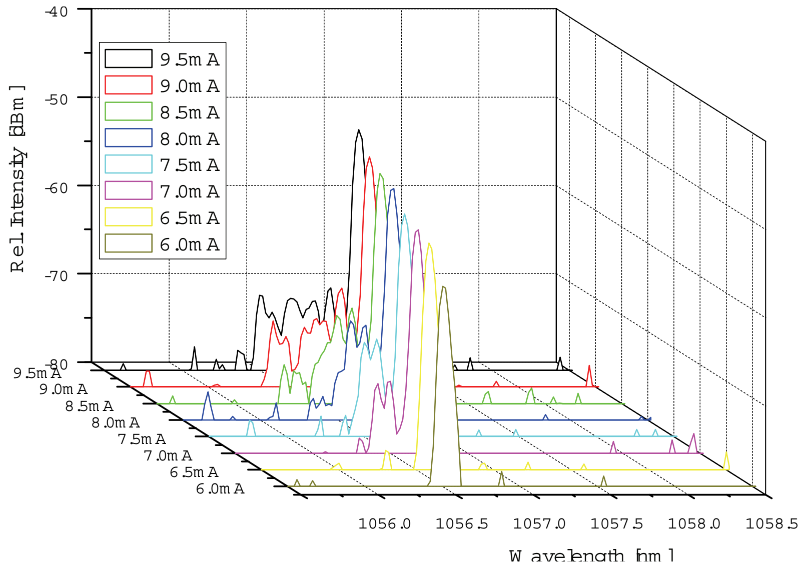

Figure 5.2: Plot of the optical spectrum of a oxide confined 1060 nm VCSEL (OSA resolution 0.05 nm).

internal loss can be estimated to be

$$\langle \alpha_i \rangle = \frac{(F_1 \eta_i - \eta_{d,1})\, \alpha_m}{\eta_{d,1}} = 46.4 \text{ cm}^{-1}. \tag{5.1}$$

For a VCSEL the transverse confinement factor is close to unity since the optical field and the electrons are both confined by the oxide aperture. The axial confinement factor for this epi-design is $\Gamma_z = 0.0347$ and thus the threshold gain can be estimated to be 1888 cm^{-1}. Assuming that the optical loss of the top p-doped DBR is 30/cm the reflectance would be 99.8%. Fig. 5.4 shows LI curves for a MM device at different substrate temperatures. The VCSEL substrate temperature was controlled through a peltier thermoelectric cooler. The characteristic temperature is 200 K.

5.2.3 Discussion

The fabrication and characterization of the 1060 nm VCSELs show that single-mode laser can be fabricated based on the $In_{0.3}Ga_{0.7}As/GaAs_{0.8}P_{0.2}$ active material. The treshold current is high compared to the state-of-the-art [77]. The high threshold current could be due to optical absorption loss in the p-DBR. The low turn-on voltage and diode

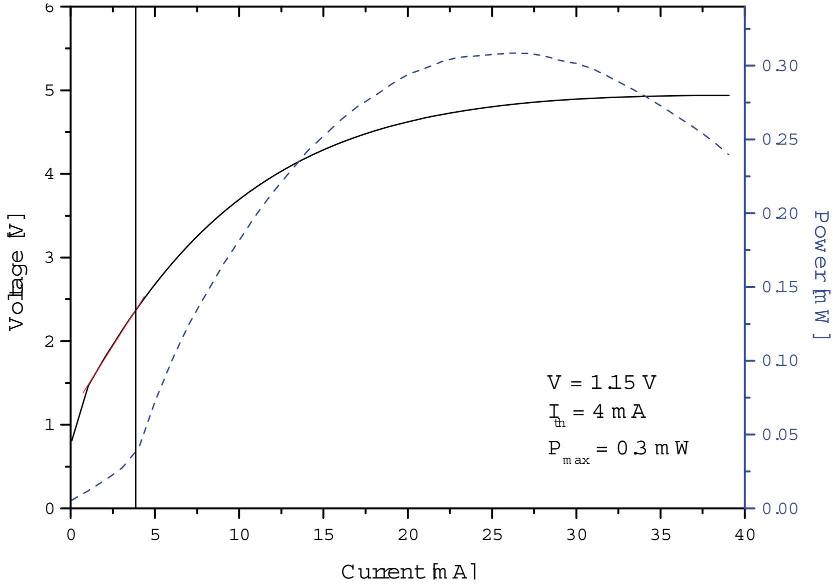

Figure 5.3: Plot of the LIV characteristics of the 1060 nm oxide confined VCSEL.

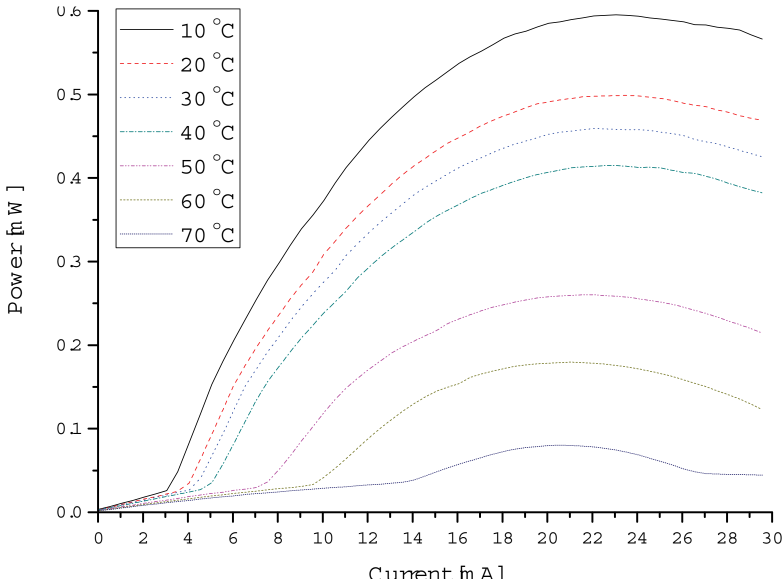

Figure 5.4: Plot of the light-current characteristics at different temperatures of the thermo-electric cooler controlling the VCSEL substrate temperature.

IV-characteristics indicate that the problem is not the DBR series resistance. Reducing the optical absorption loss, higher output powers and lower threshold currents would be expected.

5.3 HCG VCSEL

Since the HCG VCSEL was introduced by Huang et. al it has recieved increasing attention [19]. The major advantage of the HCG is that the requirements to epitaxial growth is relaxed. The first use of a HCG as part of a VCSEL demonstrated its use in reducing the number of top p-doped DBR mirror pairs [19]. Later demonstrations has shown that a HCG suspended on an oxide can fully replace the top p-doped DBR [49, 110]. We present for the first time that the ultra-high reflectivities ($> 99.5\%$) required for lasing in a VCSEL can be achieved using an air-cladded HCG. Hence this is the first demonstration where the top reflector has been replaced by a single HCG. The major challenges in achieving lasing HCG VCSELs has been to achieve ultra-high reflectivity of the top HCG mirror and reducing optical loss due to the oxide aperture area exceeding that of the top HCG mirror.

5.3.1 Device structure

The HCG VCSEL was designed to have an extended cavity using an anti-reflecting coating between the air-gap and semiconductor cavity. The device design is seen in Tab. 5.2 which shows the different material layers, their number of repetitions, thickness, optical thickness and function. The materials are read left to right and the dopants are written after a colon (:). The number of periods should be understood such that the layers with the same number are grown subsequently and the whole sequency repeated # times. The effective optical thickness are written for all layers that are part of the optical cavity. The cavity is designed as an extended cavity by supressing the reflections at the semiconductor-air interface. The bottom DBR has been doped to a Si concentration of 1×10^{18} cm^{-3} in order to lower the resistance. Since top emission is desired a high number of bottom mirror pairs have been chosen. The number of pairs could be further increased, but the reflectance will not increase much further due to free-carrier absorption. In order to limit non-radiative recombination, the cladding is undoped. The InGaAs MQW has been aligned to the fundamental of the mode field anti-node as seen in Fig. 5.5. The electric field profile has been calculated by CAMFR as covered in Sec. 2.4. The

Layer	Material	Periods #	Thickness [nm]	nL λ_0	Function
13	GaAs:Si	1	280.0	0.552	HCG
12	$In_{0.48}AlP$/Air	1	484.9	0.457	Tuning gap
11	AlO_x	1	171.0	0.250	AR-coating
10	GaAs:C	1	201.3	0.971	Current spreading
9	$AlO_x/Al_{0.98}$GaAs:C	1	55.0	0.154	Oxide aperture
8	GaAs	1	159.0	0.524	Cladding
7	$GaAsP_{0.2}$	3	11.0	0.035	Barrier
6	$In_{0.3}$GaAs	3	8.0	0.026	QW
5	$GaAsP_{0.2}$	3	11.0	0.035	Barrier
4	GaAs	1	43.9	0.145	Cladding
3	GaAs:Si	35	75.9	1.670	DBR high
2	$Al_{0.9}$GaAs:Si	35	88.1		DBR low
1	GaAs:Si	1			Substrate

Table 5.2: Device structure of the HCG VCSEL.

oxide aperture has been placed at a field anti-node in order to minimize the threshold material gain. From 3D FDTD simulation the HCG VCSEL is found to be single-mode for an oxide aperture of 8 μm. The confinement factor for this design is $\Gamma = 3.15\%$ and the threshold material gain $g_{th} = 531$ cm^{-1}. The FSR is 109 nm and the electro-static tuning range is found to be 30 nm at a tuning efficiency of 0.183 found from CAMFR simulations (the tuning efficiency from Eq. (2.31) is 0.209). The simulations are done for a $\lambda_0/2$-cavity as seen in Tab. 5.2. As the air-gap only makes up a small part of the total effective cavity length of $4.85\lambda_0$ the decrease in tuning efficiency will be negligible, while the electro-mechanical tuning range will double from increasing the air-gap to λ_0. The electro-static force on the other hand will decrease by one fourth, why a larger voltage will be required to cover the full tuning range.

5.3.2 Laser characterization

The fabricated HCG VCSELs were tested in terms of their LIV characteristics and their optical spectrum as a function of both temperature and laser forward current. Here we show results for a single-mode HCG VCSEL with a 8.5 μm aperture. Fig. 5.6 shows

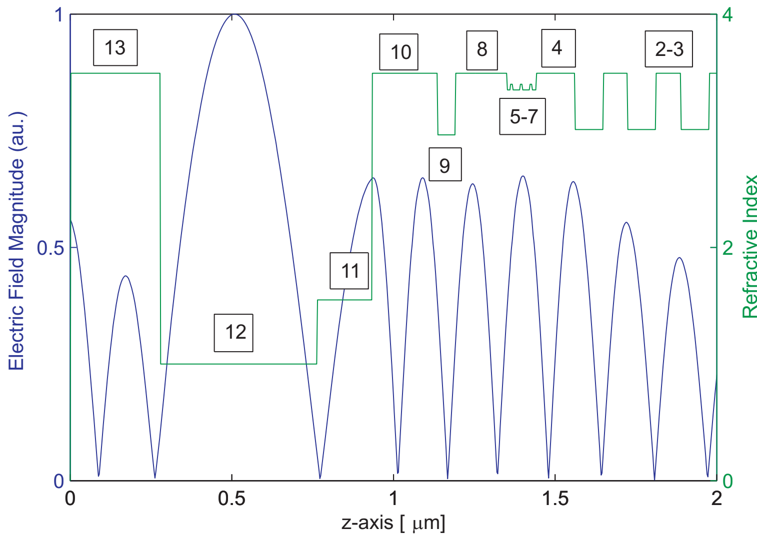

Figure 5.5: Plot of the electric field magnitude and refractive index of the HCG VCSEL. Details on the layers can be found in Tab. 5.2.

LIV characteristics of a HCG VCSEL. The turn-on voltage, V_{on}, is 1.8 V and the series resistance 210 Ω. The threshold current, I_{th}, of the device is 0.65 mA and the slope efficiency 0.15W/A. This is equivalent to a differential quantum efficiency of 13%. The maximum output power at 25°C is 0.74 mW with a laser forward current of 9.5 mA. The laser was not cooled to more than 15° due to the risk of water condensation, which would cause stiction of the HCG. From Fig. 5.6 it is seen that the threshold current continues to decrease when lowering the temperature. The median photoluminescene of the MQW is around 1045 nm and thus the cavity peak of the VCSEL in Fig. 5.6 is detuned by 23 nm from the gain peak.

Fig. 5.7 shows the spectrum of a HCG VCSEL versus current. The HCG VCSEL shows a high SMSR of over 40 dB across from 3 mA to 9 mA. Hence the laser remains single-mode up until the maximum output power. The wavelength dependence on current and temperature was found to be 0.33 nm/mA and 0.07 nm/K, respectively. From this it follows that the heating of the active region is 4.7 K/mA.

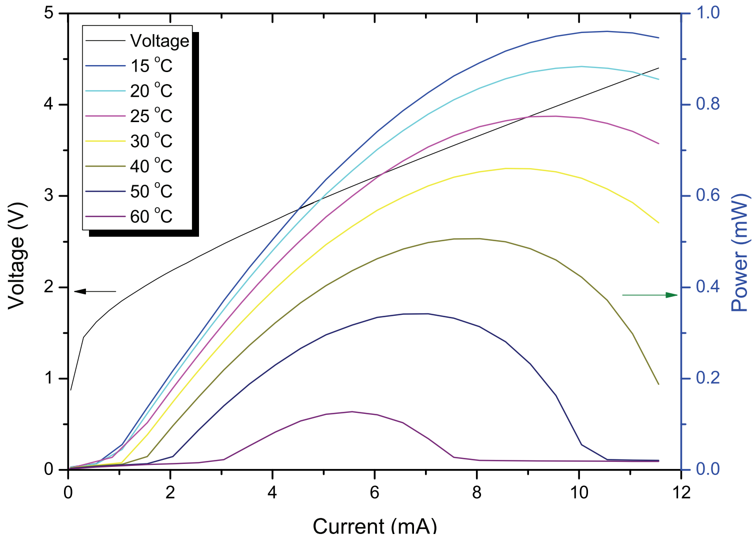

Figure 5.6: Plot of the LIV characteristics of a SM HCG-VCSEL. The peak wavelength is $\lambda_p = 1068$ nm.

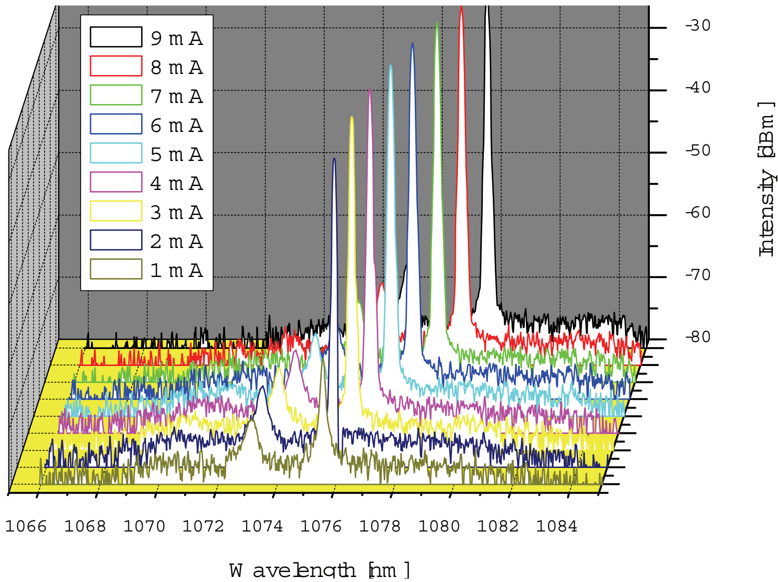

Figure 5.7: Plot of the optical spectrum of a SM HCG VCSEL. The SMSR remains more than 40 dB from 3 to 9 mA laser forward current.

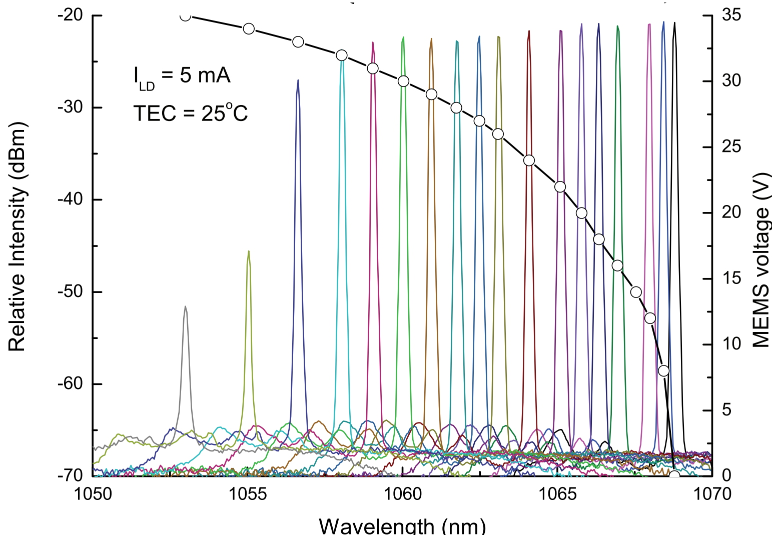

Figure 5.8: Plot of the optical spectrum (left axis) and MEMS voltage (right axis) versus wavelength.

5.3.3 Static wavelength tuning

The static tuning range was tested by applying a electrical potential, v_{DC}, between the contact to the HCG layer and the laser diode p-contact. The optical spectrum has been measured using, an optical spectrum analyzer, by coupling the VCSEL output into a single-mode fiber. Fig. 5.8 shows a plot of the optical spectrum (left axis) for different voltages (right axis, open circles). The wavelength changes from an initial value of 1069 nm at 0V to 1053 nm at 35V, which is a total change of 16 nm. The change in peak intensity from 1069 nm to 1058 nm is less than 3dB, at which points it decreases abruptly. Hence the 3dB tuning range is 11 nm. Further electro-static tuning is limited by the pull-in instability and for this HCG VCSEL the pull-in voltage is close to $V_{\mathrm{PI}} = 35$V. The ARC protects the pin-junction from the high MEMS voltages and thus the laser should be robust against pull-in. For a HCG VCSEL with an initial emission wavelength of 1070 nm we observe lasing at 1060 nm in the pull-in state with a 5 dB higher peak intensity.

5.3.4 Swept wavelength tuning

The dynamic tuning range was tested by applying an alternating voltage v with a constant potential difference offset of v_{DC} overlaid with a sinusoidal with a peak-to-peak voltage of V_{pp}. Hence the MEMS voltage is of the form

$$v(t) = v_{\mathrm{DC}} + v_{\mathrm{AC}} \cos(\omega t) , \tag{5.2}$$

where ω is the angular frequency. In Fig. 5.9 the tuning amplitude is plotted versus excitation frequency $f = 2\pi\omega$ for $v_{\mathrm{DC}} = 6\mathrm{V}$ and $v_{\mathrm{AC}} = 1.5\mathrm{V}$. The plot shows that the HCG VCSEL tuning rate is limited by low-pass behavior - as was shown in Eq. (2.49). The amplitude peaks at 850 kHz and the quality factor Q of the mechanical resonator is found to be 4. The low quality factor is due to squezed film damping. Because the excitation force, F_{el}, of the mechanical resonator depends on the square of the voltage as given in Eq. (5.2) it follows that

$$F_{\mathrm{el}} \propto v^2 = v_{\mathrm{DC}}^2 + \frac{v_{\mathrm{AC}}^2}{2} + \frac{v_{\mathrm{AC}}^2}{2} \cos(2\omega t)) + 2 v_{\mathrm{DC}} v_{\mathrm{AC}} \cos(\omega t) . \tag{5.3}$$

Hence as seen in Eq. (5.3) when driving the HCG VCSEL with an offset alternating voltage it is in fact seeing a constant term $v_{\mathrm{DC}}^2 + \frac{v_{\mathrm{AC}}^2}{2}$, an excitation at the angular frequency ω of the alternating voltage and a third term which will be referred to as the second harmonic excitation at 2ω. In order to suppress the second harmonic excitation $v_{\mathrm{DC}} >> v_{\mathrm{AC}}$. Fig. 5.10 shows the optical spectrum without excitation (solid) and for a resonant excitation with constant offset $v_{\mathrm{DC}} = 10\mathrm{V}$ and $v_{\mathrm{AC}} = 5\mathrm{V}$ (dashed) and $v_{\mathrm{AC}} = 3.5\mathrm{V}$ (dotted). The optical spectrum of the swept HCG VCSEL is an integration of the instantenous peak intensity as the OSA acquisition time is much shorter than the tuning rate. The shape of the optical spectrum is characteristics for a sinusoidal displacement for which we expect the spectral density to diverge at the edges of the tuning range [72]. Since the electro-static actuator is driven as a forced mechanical oscillator the tuning can extend to both sides of the initial peak wavelength. This enables a tuning range that is potentially twice that of the static tuning range. From Fig. 5.8 the static 3dB tuning range was found to be 11 nm compared to the resonant tuning range of 23 nm.

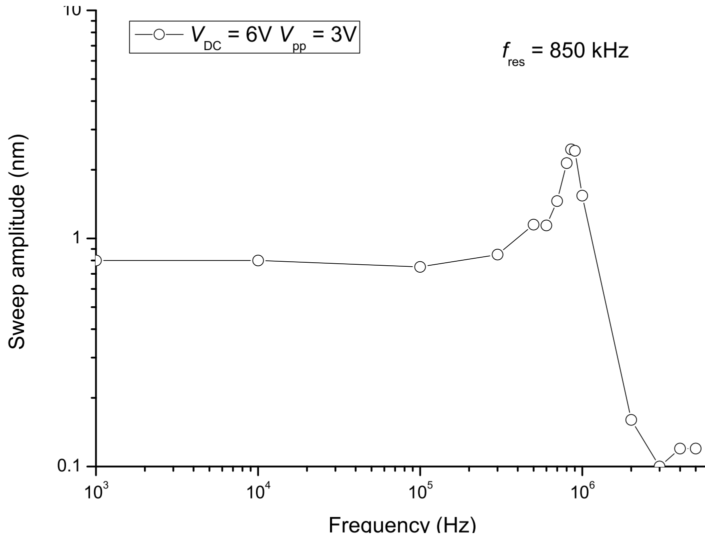

Figure 5.9: Plot of the sweep amplitude (peak wavelength envelope) versus frequency.

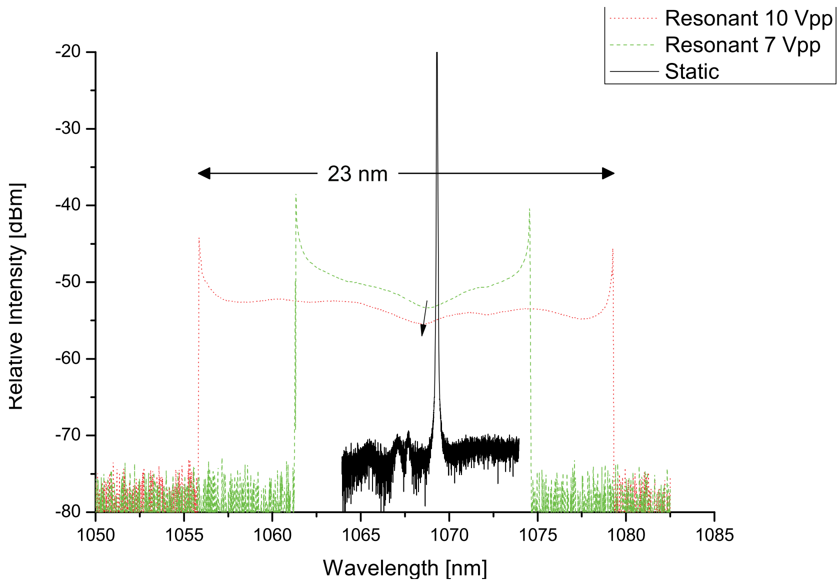

Figure 5.10: Plot of peak wavelength envelope at $V_{DC} = 0V$ (dashed) and at a small-signal tuning at a DC-offset of $V_{DC} = 6V$ and peak-to-peak voltage of $V_{pp} = 3V$ for increasing modulation frequency (solid). OSA resolution 0.1 nm.

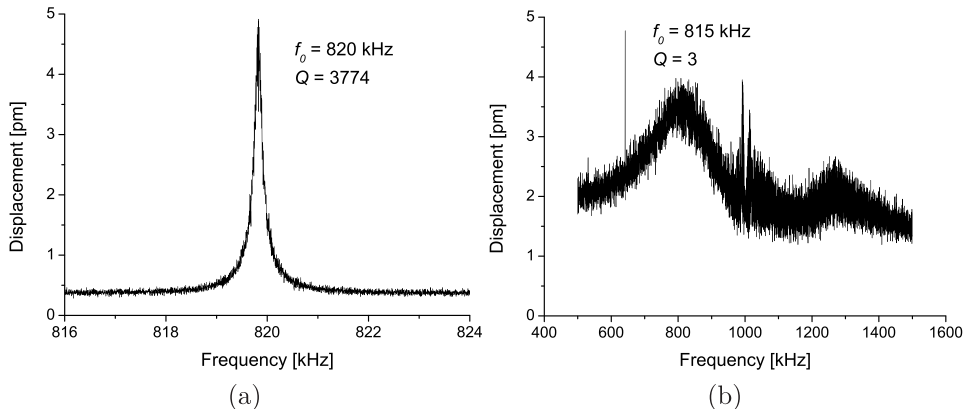

Figure 5.11: Plot of the displacement spectrum of the (a) thermal noise oscillation (b) forced oscillation with $v_{\mathrm{DC}} = 2\mathrm{V}$ and $v_{\mathrm{AC}} = 2\mathrm{V}$.

5.3.5 Mechanical characterization

The mechanical spectrum was measured using a laser Doppler vibrometer (Polytec MSA-500). Figure 5.11a shows the mechanical spectrum, measured in partial vacuum with no applied excitation, from which the resonance frequency is determined to be 820 kHz and the mechanical Q-factor 3774. Since there is no external force applied and the mechanical frequency is far from any naturally occuring vibrations it must be due to thermal vibration. By scanning the laser beam across the HCG and spring suspension, while the HCG VCSEL is subjected to piezoelectric wideband actuation, the mode shape was confirmed to be that of the fundamental mode (see Fig. 2.20). Figure 5.11b shows the mechanical spectrum measured with a forced oscillation with an excitation of $v_{\mathrm{DC}} = 2\mathrm{V}$ and $v_{\mathrm{AC}} = 2\mathrm{V}$ at atmospheric pressure. The resonance frequency is determined to be 815 kHz and the mechanical Q-factor 3.2. This compares to the dynamic measurements done using an optical spectrum analyzer.

5.3.6 Discussion

Characterization of the HCG VCSEL show single-mode operation for current up to thermal roll-over with a minimum of 40 dB SMSR. A 3 dB tuning range of 10 nm has been demonstrated in static mode

and more than 20 nm in resonant mode. The resonance frequency of the HCG VCSELs is around 850 kHz which sets the upper limit on the tuning rate. The tuning range is limited by increasing threshold current at the edge of the tuning range. In static operation the HCG VCSEL continues to lase at pull-in. This confirms that the ARC protect the VCSEL from junction breakdown and furthermore shows that high performance HCG VCSELs with oxide gap can be manufactured based on the developed process platform.

Chapter 6

Conclusion

The main result of the thesis work has been the establishment of a III-V MOEMS platform for the fabrication of vertical-cavity micro-opto-electro-mechanical systems. This has been used to make Fabry-Pérot filters and tunable VCSELs. For making tunable VCSELs at 1060 nm growth of InAlP sacrificial materials and active gain material has been done.

The wet etching properties of InAlP in diluted hydrochloric acid have been examined. The etch rate has been found to be highly anisotropic with the etch-rate being limited by the (111) plane to 0.5μm/min. The selectivity of the etch to other materials has been investigated and it has been found that the etch is selective to GaAs, AlGaAs and Al_2O_3. For GaAs we show that the selectivity is finite, and much lower that the complete selectivity that is generally stated in literature.

The sacrificial material has been used to fabricate monolithic Fabry-Pérot cavities. The Fabry-Pérot filters have been fabricated with a polarization selective top HCG mirror and bottom DBR mirror. The characterization of the filters show that a quality factor of around 200 at 1030 nm is achieved.

The gain material, $In_{0.3}Ga_{0.7}As/GaAs_{0.8}P_{0.2}$ multiple quantum wells has been used to fabricate both standard VCSELs and HCG VCSELs. The gain material shows bright photoluminescence up to 1110 nm, with FWHM down to 20 nm. Gain material with up to 5 quantum wells has been demonstrated.

The VCSELs fabricated show single-mode lasing at 1060 nm and are operating up to 60°C. This, we believe, is the first demonstra-

tion of a HCG VCSEL where an air-clad HCG fully replaces the top DBR. The HCG VCSELs show 0.9 mA threshold current and mW output power at room temperature. The full replacement of the top p-DBR with a HCG will allow optimization of the current spreading layer for better performance in terms of temperature operating range and modulation bandwidth.
Static and dynamic tuning is demonstrated for the HCG VCSEL with 1% and 2.1% relative tuning range, respectively. It is demonstrated how resonant tuning can be used to extend the tuning range of the VCSEL. This relax the trade-off between tuning range and tuning rate and will allow widely tunable VCSELs to be operated at MHz frequencies.

Outlook

Fabry-Pérot filters with a high polarization extinction ratio have applications in implementation where SOAs are used. The polarization selectivity of a Fabry-Pérot filters has been shown using a subwavelength grating. Due to the high index-contrast between the subwavelength grating and the surrounding cladding, the grating provides ultra-high reflectivity. This could enable narrow linewidth filters. Future work should focus on matching the reflectivity of the top HCG mirror to the bottom DBR mirror of the Fabry-Pérot cavity. Measurements with collimated fibers should be done to test the limits to the transmission and linewidth obtainable with such filters.
The advantage of VCSELs with highly polarized output is similar to that in Fabry-Pérot filters. The linearly polarized HCG VCSEL will allow higher final power levels to be reached with better stability. The VCSELs are the first fabricated at The Technical University of Denmark for which the epitaxial substrate has been grown inhouse. This enables tailoring of the optical properties of the gain material. The wavelength could be blueshifted with the current InGaAs MQW to the 850 nm wavelength which holds several interesting application. Furthermore experiments should be done to redshift the photoluminescense. This could enable 1300 nm VCSEL with improved single-mode output power level at the high modulation speeds used in telecommunication. In all cases continuing the

work on VCSEL, the oxidation of the AlGaAs forming the oxide aperture should be further investigated. This both involves experiments with ion implantation and optimization of the growth and wet oxidation of AlGaAs. Further work is needed on the growth of p-doped DBRs to improve the performance of the VCSELs. With further optimization of the free-carrier absorption of the epitaxial design it is believed that the threshold current could be reduced for the DBR VCSEL.

Appendix A

Fabry-Pérot Interferometer

In the following the Fabry-Pérot filter transmission function is derived (see schematic drawing in Fig. 2.7). The incoming light beam, a plane wave

$$\vec{E} = E_0 \exp\{-i\omega t)\}\hat{z}$$

will

1. Experience external reflection at **A** with a field reflection coefficient r_1 and transmission with a transmissioncoefficient t_1.

2. The transmitted wave will at **B** either (a) experience reflection with field reflection coefficient r_2 or (b) transmission with transmission coefficient t_2. The wave will further more have experienced a phaseshift of $\phi = \frac{\delta}{2}$ where δ is the phase difference between succesive transmitted waves.

3. The reflected wave (a) will then at **A** either (c) experience internal reflection with field reflection coefficient r_1 or (d) transmission with transmission coefficient t_1.

4. The reflected wave (c) will then transmit at **B** having experienced a further phase shift δ or it will reflect looping from the previous step.

The filter is to be used as a transmissive filter and from the above argumentation the transmitted wavefront can be written as

an infinite sum of the transmitted waves

$$
\begin{aligned}
E_t &= t_1 t_2 E_i \exp\{i\phi\} + t_1 t_2 r_1 r_2 \exp\{i\delta\} E_i \exp\{i\phi\} \\
&\quad + t_1 t_2 (r_1 r_2)^2 \exp\{2i\delta\} E_i \exp\{i\phi\} + ... \\
&= E_i \exp\{i\phi\} \Big[t_1 t_2 + t_1 t_2 r_1 r_2 \exp\{i\delta\} + t_1 t_2 (r_1 r_2)^2 \exp\{2i\delta\} + ... \Big] \\
&= E_i \exp\{i\phi\} t_1 t_2 \Big[1 + r_1 r_2 \exp\{i\delta\} + (r_1 r_2 \exp\{i\delta\})^2 + ... \Big] \\
&= E_i \exp\{i\phi\} t_1 t_2 \frac{1}{1 - r_1 r_2 \exp\{i\delta\}} \\
&= E_i \exp\{i\phi\} \frac{t_1 t_2}{1 - r_1 r_2 \exp\{i\delta\}} \qquad \text{(A.1)}
\end{aligned}
$$

where subscript 1 and 2 refers to the HCG and DBR mirror respectively. The transmission can be found from Eq. (A.1) as the ratio of the transmitted, $\frac{1}{2}|E_t|^2$, to the incident intensity, $\frac{1}{2}|E_i|^2$

$$
\begin{aligned}
T_I &= \frac{|E_t|^2}{|E_i|^2} = \exp\{i\phi\} \frac{t_1 t_2}{1 - r_1 r_2 \exp\{i\delta\}} \exp\{-i\phi\} \frac{t_1^* t_2^*}{1 - r_1^* r_2^* \exp\{-i\delta\}} \\
&= \frac{|t_1|^2 |t_2|^2}{1 - r_1 r_2 \exp\{i\delta\} - r_1^* r_2^* \exp\{-i\delta\} + |r_1|^2 ||r_2|^2} \\
&= \frac{|t_1|^2 |t_2|^2}{1 - |r_1||r_2| \exp\{i(\delta - \theta_1 - \theta_2)\} - |r_1||r_2| \exp\{-i(\delta - \theta_1 - \theta_2)\} + |r_1|^2 ||r_2|^2} \\
&= \frac{|t_1|^2 |t_2|^2}{1 - 2|r_1||r_2| \cos(\delta') + |r_1|^2 ||r_2|^2} \\
&= \frac{|t_1|^2 |t_2|^2}{1 + 4|r_1||r_2| \sin^2(\delta'/2) - 2|r_1||r_2| + (|r_1||r_2|)^2} \\
&= \frac{|t_1|^2 |t_2|^2}{(1 - |r_1||r_2|)^2 + 4|r_1||r_2| \sin^2(\delta'/2)} \qquad \text{(A.2}
\end{aligned}
$$

where the field reflection coefficient in general is a complex number that can be written as a

$$
r = |r| \exp\{-i\theta\}
$$

where θ will be referred to as the reflection phase ($\theta \in [-\pi; \pi]$). In this nomenclature the phase difference then includes the Fresnel reflection phases of the two mirrors

$$
\delta' = \delta - \theta_1 - \theta_2 \qquad \text{(A.3)}
$$

with the phase difference between two succesive waves being

$$\delta = \frac{4\pi n_0 g}{\lambda} \tag{A.4}$$

in case the light is surface normal. Here g is the gap distance, n_0 the refractive index of the gap medium and λ the wavelength.

Appendix B

Fabry-Pérot Filter Process

In the following the mask set and process flow for the fabrication of the HCG Fabry-Pérot Filter is presented. The sidelength of the mirror was varied from 10 μm to 50 μm to see how large mirrors it was possible to make. The larger the mirror the larger the beam spot and thus the smaller the beam divergence. This is important to avoid lateral out-coupling of light. On the other hand a larger mirror will have a lower mechanical resonance frequency. In order for the filter to have a low optical loss (2-3 dB) the backside of the filter is anti-reflection coated.

The process consist of 3 lithography steps. First the HCG mirror is defined by e-beam lithography and then the MEMS is defined by UV lithography - both using dry etching to transfer the pattern. Lastly the metal pads are patterned using a bi-layer lift-off resist process (alternative image reversal can be used or a negative resist, both easier to control). This is then followed by deposition of an anti-reflection coating on the backside and sacrificial release of the MEMS.

Mask

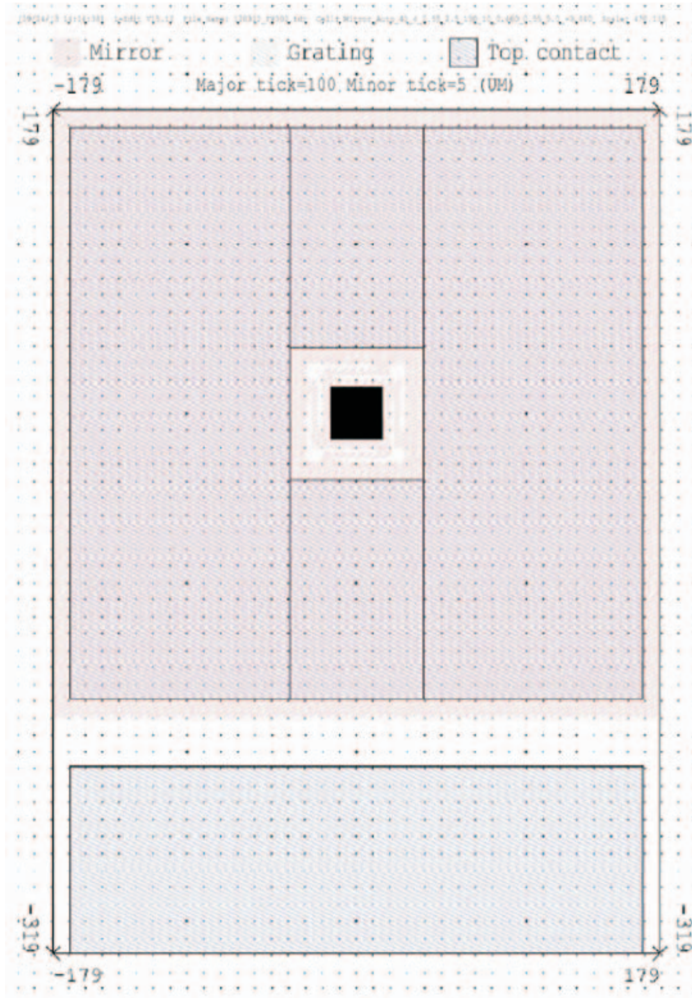

Process Flow

1. PL-Mapper Measurement of DBR-map (save complete spectra as ASCII).
2. PECVD2 10 nm PECVD2 SiO2 deposition, recipe: SIO2ky, time = 00:00:05.
3. Spin coat ZEP520A, 11 % anisole @ 2000 RPM for 60 sec (thickness 600 nm ± 3). Spin coat test on 2" silicon test piece (measure film thickness on Filmtek 4000).

4. Remove resist on backside with anisole. Softbake for 5 min @ 170 °C. Setpoint 180 °C.
5. JEOL E-beam writer. Load wafer on "2" holder", align to major flat. Mask "'Grating"'. Dose 225 μC/cm2, Current 10 nA, Aperture 7, Voltage 100 kV. Check height map (10 μm deviation is acceptable). Pattern bias 40 nm (dry etch ≈ 20 nm, wet etch ≈ 20 nm). Proximity corrected.
6. Develop 2 min in ZED-50 (shake continuously). Rinse 30 sec in Isopropanol (IPA).
7. Plasma descum for 15 sec @ 40 W (40%) with pressure set to 0.2 mbar O2.
8. Cleave into quarters.
9. III-V ICP preconditioning 10 min, recipe: GaAs PBG Etch – Cl2. Check that recipe: Chamber Clean – O2 has been run (√).
10. Heat Si carrier to 60 °C, apply a small spot of CrystalBond 555 and glue quarter to 4" Si-carrier.
11. III-V ICP dry etch, recipe: GaAs PBG Etch – Cl2. Time 02:00 mm:ss, Cl2 flow 4 sccm, Ar flow 12 sccm. Process pressure 6 mTorr, Platen Power 80 W, Chamber Power 700 W. Temperature 10 °C. Note rate 5.0 nm/s. Rate 150 nm/min in GaAs grating structures (loading factor 2).

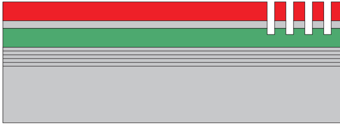

12. Heat carrier to 60 oC, release quarter, rinse in DIW 1 min (running water, backside).
13. Remove the ZEP by putting the sample upside down for 2 hours in a heated Microposit Remover 1165 bath @ 60 °C + ultrasound 5. Rinse in Acetone 5 min, IPA 1 min.
14. Dektak 3ST Measure the step height.
15. Dehydration bake @ 200 °C for 5 min on hotplate (setpoint 210°C).
16. Place in HMDS vapour for >15 min and leave in free air for >5 min.
17. Spin coat AZ5214E @ 4000 RPM for 30 sec (thickness 2.2 μm).
18. Remove resist on backside with acetone. Softbake for 90 sec

@ 90 °C.

19. MA1006 prg 1: SOFT, 20, 5 mW/cm2, Expose (EBR $\frac{1}{4}$ 2”) for 60 sec. Humidity, temperature, power.
20. Develop 60 sec in 1 AZ351B : 5 H2O.
21. MA1006 prg 3: VACUUM 20 10 10, 5 mW/cm2, Expose (UV-M1 "‘Mirror"’) for 10 sec. Humidity, temperature, power. Alignment accuracy better than 5 μm.
22. Develop 60 sec in 1 AZ351B : 5 H2O. Rinse in DIW.
23. Microscopy Inspect e-beam pattern transfer.
24. Hard bake 2 min @ 120 °C.
25. Plasma descum for 60 sec @ 40 W (40%) with pressure set to 0.2 mbar O2. Rate 50 nm/min.
26. III-V ICP preconditioning, recipe: GaAs PBG Etch – Cl2. Check that recipe: Chamber Clean – O2 has been run ($\surd$).
27. Heat Si carrier to 60 °C, apply a small spot of CrystalBond 555 and glue quarter to 4” Si-carrier.
28. III-V ICP dry etch, recipe: GaAs PBG Etch – Cl2. Time 01:15 mm:ss, Cl2 flow 4 sccm, Ar flow 12 sccm. Process pressure 6 mTorr, Platen Power 80 W, Chamber Power 700 W. Align laser interferometer to empty area. Rate 500 nm/min in GaAs, AlInP:GaAs 1:4. It takes 20 s to etch through the SiO2 adhesion layer.

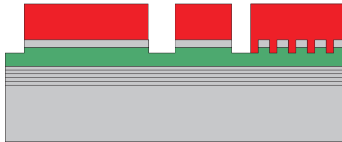

29. Heat carrier to 60 °C, release quarter, rinse in DIW 1 min (running water, backside).
30. InAlP stripping in HCl (37%):2H2O 45 sec. Rinse in DIW 3 min.
31. AZ stripping in Acetone 5 min, Ethanol 2 min and DI-water 1 min.
32. Microscopy Inspect that the mirror suspension are not under-cut.
33. Dehydration bake @ 170 °C for 5 min on hotplate (setpoint 180°C).
34. Spin coat LOR5B 700 nm @ 2000 RPM for 45 sec.
35. Edge bead removal using EBR PG (or SU-8 developer / PG-MEA). Softbake 5 min @ 170 °C. Setpoint 180 °C.

36. Spin coat AZ5206E 800 nm @ 4000 RPM for 30 sec.
37. Edge bead removal using EBR PG (or PGMEA). Softbake 90 sec @ 90 °C.
38. MA1006 prg 3: VACUUM 20 10 10, 5 mW/cm2, Expose (UV-M2 "‘Top contact"’) for 8 sec. Humidity, temperature, power.
39. Develop 1 min in 1 AZ351B : 5 H2O. Rinse in DIW.
40. Microscopy Inspect lift-off resist lithography.
41. Plasma descum for 60 sec @ 40 W (40%) with pressure set to 0.2 mbar O2. Rate 50 nm/min.
42. Wet etch SiO2 adhesion layer in 5% HF 20 sec. Etch rate 90 nm/min.
43. Deoxidation using HCl (37%):2H2O for 30 sec. Rinse in DIW. This should remove the remaining InAlP.
44. Physimeca e-beam evaporation Ni = 80 nm, Ge = 100 nm, Au = 250 nm using program ‘Ni80Ge100Au250’.

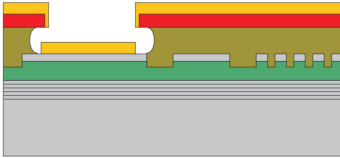

45. Immerse vertical in Remover 1165 @ 60 oC for 20 min with ultrasound 5 US + 10 min in fresh Remover 1165 @ 60 °C with ultrasound 5 US.
46. Ethanol 2 min, DIW 1 min, N2 dry (metals can be blown off).
47. Jipelec RTP rapid thermal alloying. Recipe: N-alloy for 10 sec @ 420 °C. Note logname. Place with substrate side down on METAL1-dedicated carrier
48. Remove SiO2 adhesion layer using BHF for 20 sec.
49. Wax the wafers to the glass wafer holder @ 70 °C.
50. Measure the thickness.
51. Polish 10 min with Chemlox and Chemcloth pad @ 30 RPM, pressure 2 threads. Note down etch rate and check that surface has mirror finish.
52. Measure the thickness.
53. Release the wafer from the glass plate by heating to 70 °C.
54. Ecoclear @ > 65 °C for 15-20 min, Ethanol 1 min, DIW 1 min, N2 dry.
55. Microscopy Document the surface roughness using differential interference contrast (DIC).
56. IBSD of 179 nm SiO2. Place on 2” silicon test piece. Clean

the sample with O2 sputtering.

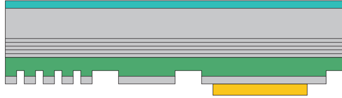

57. Filmtek 4000 measure thickness and refractive index.
58. Surface cleaning in Acetone 5 min, Ethanol 2 min and DI-water 1 min.
59. Plasma descum for 5 min @ 100 W with pressure set to 0.2 mbar O2. Rate 150 nm/s.
60. Dice quarter into 10x10 mm2 pieces.
61. InAlP wet etching using 1 HCl (37%): 2H2O for 10 min. Solution temperature 22 °C. Rinse in DIW for 5 min. Etch rate >5 μm/min [100 direction], 1 nm/min etch rate in GaAs.
62. Dilution in IPA. Transfer to 3 DIW:IPA -> DIW:IPA ->DIW:5IPA->IPA. Leave 15 min. Place a dummy piece in first slot to protect the sample from the in-jected liquid CO2 flow.
63. Critical Point Dryer. Press Vent. Fill the CPD chamber with IPA such that the sample will be covered. Press Cool and set purge time 35. Press Fill when the temperature has reached 10 °C, Pressure >700 PSI. Alarm: All lamps blinking Cause: pressure did not exceed 1072 PSI.
64. Microscopy and SEM Inspect and document stiction. Measure grating slit linewidth.

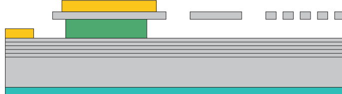

Appendix C

HCG-VCSEL Process

In the following the mask set and process flow of the HCG VCSEL is presented. The oxidation mesa diameter was varied since this it is generally difficult to control the oxidation rate as it relies exponentially on both temperature and aluminum content. The laser anode and MEMS pads are both electrically isolated by the oxidation of the high aluminum content AlGaAs layers beneath. The extra oxidation mesa is important since it allows visual inspection of the oxidation length, which is otherwise obscured by the HCG. The laser anode metallization extends around the circumference of the MEMS mesa in order to allow good current spreading and thus low resistance (and therefore low Joules heating). Furthermore room is made for undercut compensation structures (for the sacrifical release), but this was never successfull and the mask "‘Protection"’ is meant to be used in order to mask MEMS mesa from being undercut (here an oxide layer is deposited, but alternatively photoresist could be used - patterned just before the etch).

The process consists of 5 lithography steps. First the HCG, MEMS and MEMS pad is defined by e-beam litography using a two current exposure to reduce the total exposure time. The e-beam resist HSQ can be used directly as an etch mask to transfer the pattern by dry etching. Next UV-lithography is used to expose the laser anode contact layer by wet etching. Following this the oxidation mesa and laser anode pad is patterned by UV lithography and wet etching. It was a recurring issue that the resist adhesion was not good enough during the wet etching which would result in ragged edges of the oxidation mesa. After oxidation of the aperture

and anti-reflection layers metal contacts was patterned by lift-off. Lastly the MEMS was released by wet etching the sacrificial material.

Mask

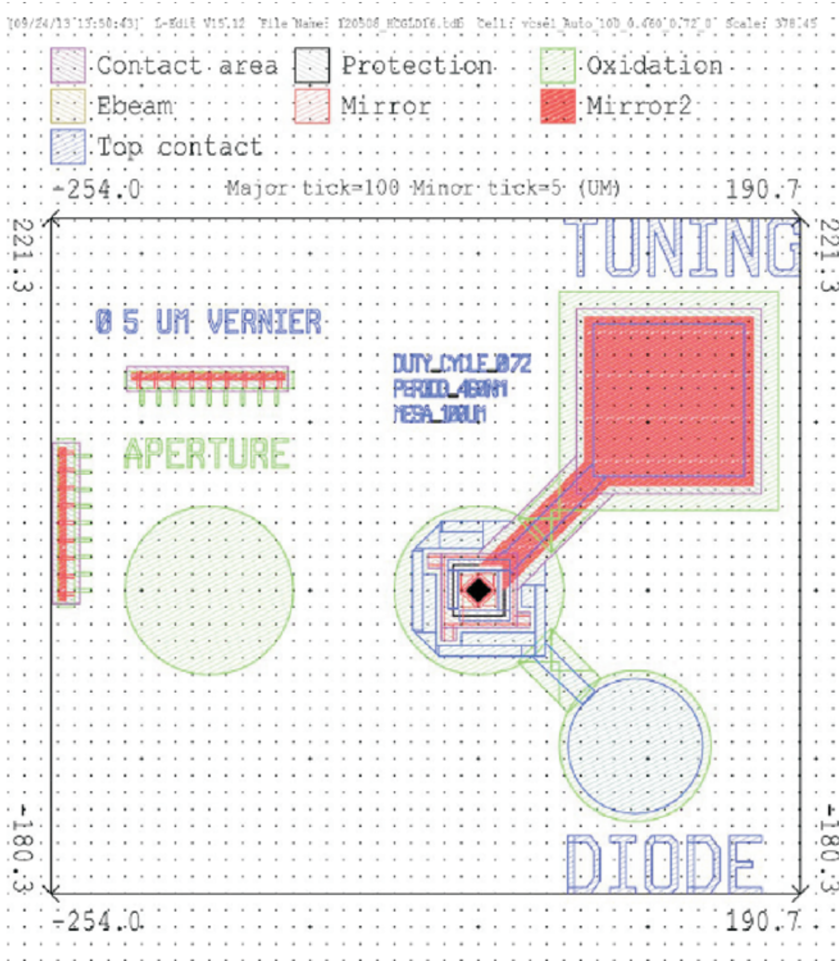

Process Flow

1. PL-Mapper Measurement of DBR-map and photoluminescence (save complete spectra as ASCII). The DBR bandwidth center is 1060 nm and the PL peak is 1060 nm.
2. Hotplate dehydration @ 150 °C for 2 min + 10 s cooldown.

3. Spin coat 6% XR-1541:MIBK @ 1000 RPM for 60 sec (thickness 180 nm). Exposure should be done the same day as spinning. Pour the XR-1541 into a small plastic container the day before (place in fridge). Avoid water. Spin coat test on 2" silicon test piece (measure film thickness on Filmtek 4000).
4. Softbake for 2 min @ 150 °C. Setpoint 160 °C.
5. Wait minimum 1 hr before exposure! JEOL E-beam writer. Load wafer on "2" holder, 2A". Dose 3000 μC/cm2, M1A "'Mirror"' : Current 10 nA, M1B "'Mirror2"' : Current 64 nA. Aperture 7, Voltage 100 kV. Use proximity correction. Numerical PSF = HSQ180nm.xrz. Beam FWHM 50 nm. Include short range effects ($\surd$).
6. Develop 1 min in 1:3 AZ400K:H2O (shake continuously). Rinse 30 sec in DIW.
7. Cleave into quarters.
8. III-V ICP preconditioning 15 min, recipe: GaAs PBG Etch – Cl2. Check that recipe: Chamber Clean – O2 has been run ($\surd$).
9. Heat Si carrier to 60 °C, apply a small spot of CrystalBond 555 and glue quarter to 4" Si-carrier.
10. III-V ICP dry etch, recipe: GaAs PBG Etch – Cl2. Time 02:00 mm:ss, Cl2 flow 4 sccm, Ar flow 12 sccm. Process pressure 6 mTorr, Platen Power 80 W, Chamber Power 700 W. Align laser interferometer to GaAs area. Note GaAs Etch rate 5.0 nm/s and AlInP Etch rate 2.0 nm/s. Overetch time 70 s. HCG Etchrate 160 nm/min (loading factor = 2), HSQ Etch rate 30 nm/min.

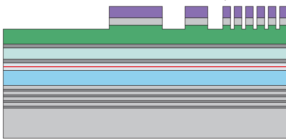

11. Heat carrier to 60 °C, release quarter, rinse in DIW 1 min (running water, backside).
12. Remove the HSQ in 1% HF for 00:30 mm:ss. Rinse in DIW, N2 blow dry.
13. 15 nm PECVD2 SiO2 deposition, recipe: SIO2ky2, time = 00:00:10 hh :mm :ss. Rate 90 nm/min.
14. Place in HMDS vapour for 15 min and leave in free air for 5

min.

15. Spin coat AZ5214E @ 4000 RPM for 30 sec (thickness 1.3 μm).
16. Remove resist on backside with acetone. Softbake for 90 sec @ 90 °C.
17. MA1006 prg 3: VACUUM 20 10 10, 5 mW/cm2, Expose (UV-M2 "'Contact area"') for 10 sec. Note humidity, temperature, power. Alignment A.
18. Develop 60 sec in 1 AZ351B : 5 H2O. Rinse in DIW.
19. Hard bake 2 min @ 120 °C.
20. Plasma descum for 60 sec @ 40 W (40%) with pressure set to 0.2 mbar O2. Rate 50 nm/min.
21. Dektak 3ST profilometer step height resist 17000 Å.
22. Wet etch SiO2 adhesion layer in BHF 15 sec. DIW rinse. PECVD1 SiO2 Etch rate 147 nm/min.
23. Wet etch 566 nm AlInP layer in HCl:5H2O for 80 sec. Temp 22 °C. DIW rinse. Etch rate 0.6 μm/min (Lothian, 1992). Reaction-rate control. Part of the AlInP has been dry etched, see 1.10. Real AlInP thickness = $t_{epi,AlInP}$ - overetch time * v_{AlInP}.
24. Wet etch GaAs capping layer in 90 g C6H8O7 : 90 g H2O : 6 mL H2O2 for 20 sec (volume ratio 25:25:1). Use magnetic stirrer for mixing citric acid. Wait 15 min after mixing. DIW rinse. GaAs Etch rate 1.2 nm/s (DeSalvo, 1992). Reaction-rate control.

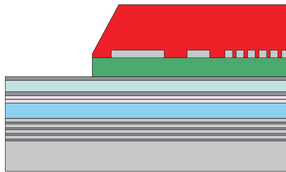

25. Dektak 3ST profilometer step height Å excl. resist. Check with 2.11 - OK ($\surd$).
26. Strip photoresist in Acetone 5 min, Ethanol 1 min, DIW rinse.
27. Strip SiO2 adhesion and AlGaAs anti-reflection layer in 5 H2O : 5% HF 20 sec. The etch stops at the GaAs current spreading layer. DIW rinse. N2 blow dry. $Al_0.98Ga_0.02As$ Etch rate 0.3 mum/min (Kumar 2007). PECVD1 SiO2 Etch rate 20 nm/min.
28. Plasma asher for 5 min @ 100 W (100%) with pressure set to

0.2 mbar O2. Rate 150 nm/s.

29. Dektak 3ST VCSEL step height 10290 Å.
30. 15 nm PECVD2 SiO2 deposition, recipe: SIO2ky2, time = 00:00:10. Rate 90 nm/min.
31. Place in HMDS vapour for >15 min and leave in free air for >5 min.
32. Spin coat AZ5214E @ 4000 RPM for 30 sec (thickness 1.3 μm).
33. Remove resist on backside with acetone. Softbake for 90 sec @ 90 °C.
34. MA1006 prg 3: VACUUM 20 10 10, 5 mW/cm2, Expose (UV-M3 "'Oxidation"') for 10 sec. Note humidity, temperature, power. Alignment B, tolerance 1 μm.
35. Develop 60 sec in 1 AZ351B : 5 H2O. Rinse in DIW.
36. Hard bake 2 min @ 120 °C.
37. Plasma descum for 60 sec @ 40 W (40%) with pressure set to 0.2 mbar O2. Rate 50 nm/min.
38. Dektak 3ST profilometer step height resist 17000 Å.
39. Wet etch SiO2 adhesion layer in BHF 15 sec. DIW rinse. PECVD1 SiO2 Etch rate 147 nm/min.
40. Wet etch 201 nm GaAs layer in 4 C6H8O7 : 4 H2O : H2O2 for 60 sec. Use magnetic stirrer for mixing citric acid. Wait 15 min after mixing. DIW rinse. GaAs Etch rate 6 $\pm$ 2 nm/s (Tong, 1992). Selectivity to AlAs > 700. Reaction-rate control. Resist etch rate 0.2 μm/min.

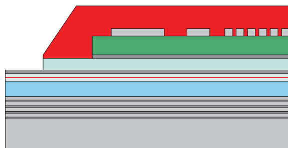

41. Dektak 3ST profilometer step height 2390 Å excl. resist. OK ($\surd$).
42. Strip photoresist in Acetone 5 min, Ethanol 1 min, DIW rinse.
43. Dektak 3ST VCSEL step height 12690 Å. Profilometer 2390 Å.
44. Plasma asher for 5 min @ 100 W (100%) with pressure set to 0.2 mbar O2.
45. Wet etch AlGaAs oxidation layer in BHF 30 sec. Etch should stop at the GaAs. DIW rinse 2 min. N2 blow dry.This should be done im-mediately before oxidation – to give reproducible

results.You cannot see the AlGaAs being removed before it is dried.

46. Oxidation 01:46 hh:mm @ 440 °C with 900 sccm N2 through H2O-bubbler @ 95 °C. Oxide aperture 8 μm. Start program FLOW440 & turn on bubbler 1.5 hr before. Make test oxidation to establish rate. Lateral oxidation Rate 0.51 μm/min.

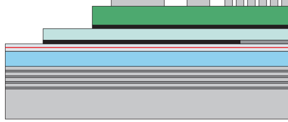

47. Differential Interference Contrast Microscopy, measure oxidation length.
48. Dektak 3ST VCSEL step height 12990 Å.
49. PL-Mapper wafer photoluminescence peak.
50. 75 nm PECVD2 SiO2 deposition, recipe: SIO2ky2, time = 00:00:50. Rate 90 nm/min.
51. Place in HMDS vapour for 15 min and leave in free air for 5 min.
52. Spin coat AZ5214E @ 4000 RPM for 30 sec (thickness 1.3 μm).
53. Remove resist on backside with acetone. Softbake for 90 sec @ 90 °C.
54. MA1006 prg 3: VACUUM 20 10 10, 5 mW/cm2, Expose (UV-M4 "‘Protection"’) for 8 sec. Note humidity, temperatire, power.
55. Develop 60 sec in 1 AZ351B : 5 H2O. Rinse in DIW.
56. Hard bake 2 min @ 120 °C.
57. Plasma descum for 60 sec @ 40 W (40%) with pressure set to 0.2 mbar O2. Rate 50 nm/min.
58. Oxide wet etching using BHF 45 sec. DIW rinse. SiO2 Etch rate 147 nm/min.
59. 20 nm PECVD2 SiO2 deposition, recipe: SIO2ky, time = 00:00:15. Rate 90 nm/min.
60. Place in HMDS vapour for >15 min and leave in free air for >5 min.
61. Spin coat AZ5214E @ 1500 RPM for 30 sec (thickness 2.3 μm). The pattern step height is 1.165 μm.
62. Remove resist on backside with acetone. Softbake for 90 sec @ 90 °C.

63. MA1006 prg 1: VACUUM 20 10 10, 5 mW/cm2, Expose (UV-M5 "‘Top contact"’) for 4 sec. Note humidity, temperature, power.
64. Reversal bake 2 min @ 120 °C. Setpoint 130 °C.
65. MA1006 prg 6: FLOOD, 5 mW/cm2, Flood expose full wafer 40 sec. Note humidity, temperature, power.
66. Develop 70 sec in 1 AZ351B : 5 H2O.
67. Plasma descum for 60 sec @ 40 W (40%) with pressure set to 0.2 mbar O2. Rate 50 nm/min.
68. Deoxidation using BHF for 45 s and HCl : 2H2O for 15 s. Also strips SiO2.
69. Physimeca e-beam evaporation Pd = 20 nm, Ge = 40 nm, Ti = 40 nm, Pt = 30 nm, Au = 200 nm using program ‘Pd20Ge40Ti40Pt30Au250’. Same metal stack for both MEMS and LASER contact (n- and p-type). (Han 1993)
70. Immerse in Acetone 20 min with ultrasound 5 US or until lift-off is complete.
71. Ethanol 2 min, DIW 1 min, N2 dry.
72. Prebake 60 sec @ 120 °C. Setpoint 130 °C.
73. Front protection Spin coat AZ5214E @ 4000 RPM for 30 sec (thickness 1.7 μm). Hardbake @ 120 °C for 2 min.
74. Wet etch native oxide NH4OH:10H2O 30 sec with magnetic stirrer. DIW rinse. Degrease backside and remove native oxide. (Ashby)
75. Backside Physimeca e-beam evaporation Ni = 80 nm, Ge = 100 nm, Au = 250 nm using program ‘Ni80Ge100Au250’.

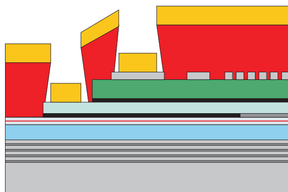

76. Strip photoresist in Acetone 5 min, Ethanol 2 min, DIW rinse.
77. Plasma asher for 5 min @ 100 W (100%) with pressure set to 0.2 mbar O2. Rate 150 nm/s.
78. RTP rapid thermal alloying. Recipe: nalloy for 15 s @ 420 oC. Note logname. Place with substrate side down on gold-dedicated carrier.
79. Strip SiO2 adhesion layer and wet etch aluminum oxide (on AlInP) in BHF 20 sec. DIW rinse. The oxide aperture and

AlGaAs of the DBR will also etch. Remaining SiO2 adhesion layer will also be removed. SiO2 Etch rate 147 nm/min.

80. InAlP wet etching using 1 HCl (37%): 5 H2O for 180 sec. Solution temperature 22 oC. Etch rate 0.5 μm/min in the [110] direction and >5 μm/min in the [100], 2 nm/min etch rate in GaAs. Reaction-rate control. Rinse in DIW for 5 min.
81. Dilution in IPA. Transfer to 3 DIW:IPA -> DIW:IPA ->DIW:5IPA->IPA. Leave 15 min. Place a dummy piece in first slot to protect the sample from the in-jected liquid CO2 flow.
82. Critical Point Dryer. Press Vent. Fill the CPD chamber with IPA such that the sample will be covered. Press Cool and set purge time 35. Press Fill when the temperature has reached 10 °C, Pressure >700 PSI. Alarm: All lamps blinking, Cause: pressure did not exceed 1072 PSI.

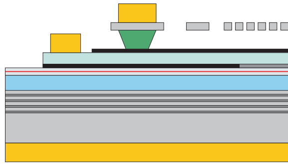

83. Microscopy & SEM-Zeiss Inspect.

Acronyms

ARC anti-reflective coating

ARDE aspect-ratio dependent etching

ASE Amplified Stimulated Emission

CMOS complementary metal-oxide-semiconductor

CW Continous Wave

DBR Distributed Bragg Reflector

DSP Digital Signal Processing

ECL External Cavity Laser

FDTD Finite-Difference Time-Domain

FDML Fourier Domain Mode-Locked

FSR Free Spectral Range

FWHM Full-Width at Half-Maximum

GMR Guided-Mode Resonance

GIRO GIant Reflectivity to zero Order

HCG High-index Contrast subwavelength Grating

ICP Inductively Coupled Plasma

laser Light Amplification by Stimulated Emission of Radiation

LIV Light-Current-Voltage

MM multimode

ND Neutral Density

maser Microwave Amplification by Stimulated Emission of Radiation

MEMS Micro-Electro-Mechanical Systems

MOEMS Micro-Opto-Electro-Mechanical Systems

MOVPE Metal-Organic Vapour Phase Epitaxy

MQW Multiple Quantum Well

OCT Optical Coherence Tomography

OSA Optical Spectrum Analyzer

PCF photonic crystal fiber

PL Photoluminescence

PM Polarization Maintaining

QW Quantum Well

RCLED Resonant-Cavity Light Emitting Diode

RCWA Rigorously Coupled Wave Analysis

RIE Reactive Ion Etching

SD-OCT Spectral-Domain OCT

SGDBR Sampled Grating DBR

SM Single Mode

SOA Semiconductor Optical Amplifier

SS-OCT Swept Source OCT

SMSR Side-Mode Suppression Ratio

TE Transverse Electric

TM Transverse Magnetic

TMM Transmission Matrix Method

VCSEL Vertical-Cavity Surface-Emitting Laser

XRD X-Ray Diffraction

ZNS Zero Net Strain

WDM Wavelength Division Multiplexing

Chemical compounds

HSQ hydrogen silsesqouioxane

CBr_4 carbon tetrabromide

CHF_3 flouroform

CH_4 methane

TMAl trimethylaluminum

Si_2H_6 disilane

Si_3N_4 silicon nitride

SiO_2 silicon oxide

PH_3 phosphine

TBP tributhylphosphine

TMGa trimethylgalium

AsH_3 arsine

TMIn trimethylindium

BHF buffered hydroflouric acid

VOC Volatile Organic Compound

List of publications

The following is a list of the publications to which the author has contributed that has been published or submitted during the duration of the PhD (Nov 2008 – August 2012). Between the publication (August 2012) and book printing (October 2013) 3 additional papers has been published why the publication details has been corrected here. Publications marked with $\notin$ are based on earlier work. Non peer-reviewed articles are markeed with †.

Published

I † T. Ansbæk, C. H. Nielsen N. B. Larsen, I. S. Chung, D. Larsson and K. Yvind. Time-resolved measurement of the light-current characteristic of a coated VCSEL diode in acetone vapour. *International Nano-Optoelectronics Workshop*, Berlin-Stockholm, 2009.

II † T. Ansbæk, C. H. Nielsen, N. B. Larsen, S. Dohn, A. Boisen, I.S. Chung, D. Larsson and K. Yvind. Acetone vapor sensing using a vertical cavity surface emitting laser diode coated with polystyrene. *Annual Conference on Commercialization of Micro and Nano Systems* 14, Copenhagen, 2009.

III $\notin$ T. Ansbæk, D.H. Petersen, O. Hansen, J. B. Larsen, T. M. Hansen P. Bøggild. Fundamental size limitations of micro four-point probes. *Microelectronic Engineering* 4-6 (86) pp. 987–990, 2009.

IV $\notin$ G. Fragiacomo, T. Ansbæk, T. Pedersen, O. Hansen and E. V. Thomsen. Analysis of small deflection touch mode behavior in capacitive pressure sensors. *Sensors and Actuators*

A: Physical 1 (161) pp. 114–119, 2010.

V † T. Ansbæk, C. H. Nielsen, N. B. Larsen, S. Dohn, A. Boisen, I. S. Chung, D. Larsson and K. Yvind. Polymer-coated vertical-cavity surface-emitting laser diode vapor sensor. Proceedings of SPIE (7615) pp. 76150A, 2010.

VI ∉ G. Fragiacomo, E. V. Thomsen and T. Ansbæk. Validation of an analytical model for contact mode plate deflection of touch mode capacitive pressure sensors. *Sensing Technology (ICST), 2011 Fifth International Conference on*, New Zeeland, pp. 634–638, 2011.

VII T. Ansbæk, C. H. Nielsen, S. Dohn, I.S. Chung, D. Larsson and K. Yvind. Vertical-cavity surface-emitting laser vapor sensor using swelling polymer reflection modulation. *Applied Physics Letters* 101 (14) pp. 143505–143505, 2012.

VIII T. Ansbæk, E. Semenova, O. Hansen and K. Yvind. Crystallographic dependence of the lateral undercut wet etch rate of Al 0.5 In 0.5 P in diluted HCl for III-V sacrificial release. *Journal of Vacuum Science & Technology B: Microelectronics and Nanometer Structures* 31 (1) pp. 011209-011209, 2013.

IX T. Ansbæk, I. S. Chung and K. Yvind. 1060 nm Tunable Monolithic High Index Contrast Subwavelength Grating Vertical-Cavity Surface-Emitting Laser. *IEEE Photonics Technology Letters* 25 (4) pp. 365–367, 2013.

X T. Ansbæk, I. S. Chung and K. Yvind. Resonant MEMS Tunable VCSEL. *IEEE Journal of Selected Topics in Quantum Electronics* 19 (4) pp. 1702306, 2013.

Bibliography

[1] S. Marschall, B. Sander, M. Mogensen, T. M. Jø rgensen, and P. E. Andersen, "Optical coherence tomography-current technology and applications in clinical and biomedical research." *Analytical and Bioanalytical Chemistry*, vol. 400, no. 9, pp. 2699–720, Jul. 2011.

[2] B. Potsaid, B. Baumann, D. Huang, S. Barry, A. E. Cable, J. S. Schuman, J. S. Duker, and J. G. Fujimoto, "Ultrahigh speed 1050nm swept source/Fourier domain OCT retinal and anterior segment imaging at 100,000 to 400,000 axial scans per second." *Optics Express*, vol. 18, no. 19, pp. 20 029–48, Sep. 2010.

[3] C. V. Regatieri, L. Branchini, and J. S. Duker, "The Role of Spectral-Domain OCT in the Diagnosis and Management of Neovascular Age-Related Macular Degeneration," *Ophthalmic Surgery, Lasers & Imaging*, vol. 42, no. 4, pp. 56–66, 2011.

[4] A. Einstein, "Zur quantentheorie der strahlung," *Physikalische Zeitschrift*, vol. 18, pp. 121–128, 1917.

[5] J. P. Gordon, H. J. Zeiger, and C. H. Townes, "The maser - new type of microwave amplifier, frequency standard, and spectrometer," *Physical Review Letters*, vol. 99, no. 4, pp. 1264–1274, 1955.

[6] "Technology," *Science News*, vol. 132, no. 22, p. 349, 1987.

[7] R. N. Hall, G. E. Fenner, J. D. Kingsley, T. J. Soltys, and R. O. Carlson, "Coherent Light Emission From GaAs Junc-

tions," *Physical Review Letters*, vol. 9, no. 9, pp. 366–368, 1962.

[8] N. Holonyak and S. F. Bevacqua, "Coherent (visible) light emission from Ga(As1-xPx) junctions," *Applied Physics Letters*, vol. 1, no. 4, pp. 82–83, 1962.

[9] T. Skettrup, *Laserteknik*, 5th ed. Polyteknisk Forlag, 1993.

[10] K. Liu and M. G. Littman, "Novel geometry for single-mode scanning of tunable lasers," *Optics Letters*, vol. 6, no. 3, p. 117, Mar. 1981.

[11] A. Q. Liu, X. M. Zhanga, J. Li, and C. Lu, "Single-/multi-mode tunable lasers using MEMS mirror and grating," *Sensors and Actuators A: Physical*, vol. 108, no. 1-3, pp. 49–54, 2003.

[12] J. Berger, Y. Zhang, J. D. Grade, H. Lee, S. Hrinya, and H. Jerman, "Widely tunable external cavity diode laser based on a MEMS electrostatic rotary actuator," in *Optical Fiber Communication Conference.* Optical Society of America, Mar. 2001, p. TuJ2.

[13] A. Morosawa, C. Chong, T. Sakai, and O. Nenjozaka, "Wide tuning range wavelength-swept laser with single semiconductor optical amplifier for OCT," *European Conferences on Biomedical Optics*, vol. 6627, pp. 2–7, Jun. 2007.

[14] S. M. R. Motaghian Nezam, "High-speed polygon-scanner-based wavelength- swept laser source in the telescope-less configurations with application in optical coherence tomography," *Optics Letters*, vol. 33, no. 15, p. 1741, Jul. 2008.

[15] M. Kuznetsov, W. Atia, B. Johnson, and D. Flanders, "Compact ultrafast reflective Fabry-Perot tunable lasers for OCT imaging applications," *Biomedicine*, vol. 7554, pp. 75 541F–75 541F–6, 2010.

[16] M. P. Minneman, J. Ensher, M. Crawford, and D. Derickson, "All-semiconductor high-speed akinetic swept-source for OCT," in *Proceedings of SPIE 8311*, vol. 8311, 2011, pp. 831 116–831 116–10.

[17] L. Coldren, "Monolithic tunable diode lasers," *IEEE Journal of Selected Topics in Quantum Electronics*, vol. 6, no. 6, pp. 988–999, 2000.

[18] D. Derickson, M. Bernacil, A. DeKelaita, B. Maher, S. O'Connor, M. Sysak, and L. Johanssen, "SGDBR single-chip wavelength tunable lasers for swept source OCT," in *Proceedings of SPIE*, vol. 6847, 2008.

[19] M. C. Y. Huang, Y. Zhou, and C. J. Chang-Hasnain, "A nanoelectromechanical tunable laser," *Nature Photonics*, vol. 2, no. 3, pp. 180–184, Feb. 2008.

[20] V. Jayaraman, J. Jiang, B. Potsaid, G. Cole, J. Fujimoto, and A. Cable, "Design and performance of broadly tunable, narrow line-width, high repetition rate 1310nm vcsels for swept source optical coherence tomography," in *Proceedings of SPIE*, 2012, pp. 82 760D–82 760D–11.

[21] H. C. Nathanson, W. E. Newell, R. A. Wickstrom, and J. R. Davis, "The resonant gate transistor," *IEEE Transactions on Electron Devices*, vol. 14, no. 3, pp. 117–133, Mar. 1967.

[22] I. Melngailis, "Longitudinal Injection-Plasma Laser of InSb," *Applied Physics Letters*, vol. 6, no. 3, pp. 59–60, 1965.

[23] H. Soda, K.-i. Iga, C. Kitahara, and Y. Suematsu, "GaInAsP/InP Surface Emitting Injection Lasers," *Japanese Journal of Applied Physics*, vol. 18, no. 12, pp. 2329–2330, Dec. 1979.

[24] F. Koyama, S. Kinoshita, and K. Iga, "Room-temperature continuous wave lasing characteristics of a GaAs vertical cavity surface-emitting laser," *Applied Physics Letters*, vol. 55, no. 3, p. 221, Jul. 1989.

[25] M. S. Wu, E. C. Vail, G. S. Li, W. Yuen, and C. J. Chang-Hasnain, "Tunable micromachined vertical cavity surface emitting laser," *Electronics Letters*, vol. 31, no. 19, p. 1671, 1995.

[26] E. C. Vail, G. Li, W. Yuen, and C. J. Chang-Hasnain, "High Performance and Novel Effects of Micromechanical Tunable Vertical-Cavity Lasers," *IEEE Journal of Selected Topics in Quantum Electronics*, vol. 3, no. 2, pp. 691–697, 1997.

[27] F. Sugihwo, M. C. Larson, and J. S. Harris, "Low threshold continuously tunable vertical-cavity surface-emitting lasers with 19.1 nm wavelength range," *Applied Physics Letters*, vol. 70, no. 5, p. 547, 1997.

[28] C. Gierl, T. Gruendl, P. Debernardi, and K. Zogal, "Surface micromachined tunable 1.55 um-VCSEL with 102 nm continuous single-mode tuning," *Optics Express*, vol. 19, no. 18, pp. 272–277, 2011.

[29] Y. Zhou, M. C. Huang, and C. J. Chang-Hasnain, "Tunable VCSEL with ultra-thin high contrast grating for high-speed tuning." *Optics Express*, vol. 16, no. 18, pp. 14 221–14 226, 2008.

[30] T. Yano, H. Saitou, N. Kanbara, R. Noda, S.-i. Tezuka, and N. Fujimura, "Wavelength Modulation Over 500 kHz of Micromechanically Tunable InP-Based VCSELs," *IEEE Journal of Selected Topics in Quantum Electronics*, vol. 15, no. 3, pp. 528–534, 2009.

[31] C. Gierl, T. Grüdl, K. Zogal, H. A. Davani, C. Grasse, G. Böhm, F. KuÌˆppers, P. Meissner, and M.-C. Amann, "Surface micromachined MEMS-tunable VCSELs with wide and fast wavelength tuning," *Electronics Letters*, vol. 47, no. 22, p. 1243, 2011.

[32] F. Riemenschneider, M. Maute, H. Halbritter, G. Boehm, M.-C. Amann, and P. Meissner, "Continuously Tunable Long-Wavelength MEMS-VCSEL With Over 40-nm Tuning Range," *IEEE Photonics Technology Letters*, vol. 16, no. 10, pp. 2212–2214, Oct. 2004.

[33] M. C. Y. Huang, K. B. Cheng, Y. Zhou, A. P. Pisano, and C. J. Chang-Hasnain, "Monolithic Integrated Piezoelectric MEMS-Tunable VCSEL," *IEEE Journal of Selected Topics in Quantum Electronics*, vol. 13, no. 2, pp. 374–380, 2007.

[34] G. D. Cole, E. Behymer, T. C. Bond, and L. L. Goddard, "Short-wavelength MEMS-tunable VCSELs." *Optics Express*, vol. 16, no. 20, pp. 16 093–103, Sep. 2008.

[35] H. A. Davani, C. Grasse, P. Westbergh, C. Gierl, K. Zogal, S. Jatta, P. Meissner, B. Kogel, G. Bohm, T. Grundl, A. Larsson, and M.-C. Amann, "Widely tunable high-speed bulk-micromachined short-wavelength MEMS-VCSEL," in *Semiconductor Laser Conference (ISLC), 2010 22nd IEEE International.* IEEE, Sep. 2010, pp. 9–10.

[36] I.-S. Chung, V. Iakovlev, A. Sirbu, A. Mereuta, A. Caliman, E. Kapon, and J. Mø rk, "Broadband MEMS-Tunable High-Index-Contrast Subwavelength Grating Long-Wavelength VCSEL," *Quantum Electronics IEEE Journal of*, vol. 46, no. 9, pp. 1245–1253, 2010.

[37] H. Soda, "GaInAsP/InP surface emitting injection lasers with short cavity length," *IEEE Journal of Quantum Electronics*, vol. 19, pp. 1035–1041, 1983.

[38] C. F. R. Mateus, M. C. Y. Huang, Y. Deng, A. R. Neureuther, and C. J. Chang-Hasnain, "Ultrabroadband Mirror Using Low-Index Cladded Subwavelength Grating," *IEEE Photonics Technology Letters*, vol. 16, no. 2, pp. 518–520, Feb. 2004.

[39] R. Magnusson and S. S. Wang, "New principle for optical filters," *Applied Physics Letters*, vol. 61, no. 9, p. 1022, Aug. 1992.

[40] R. Baets, B. Demeulenaere, B. Dhoedt, and S. Goeman, "Optical system with a dielectric subwavelength structure having high reflectivity and polarization selectivity," U.S. Patent 6 191 890, 2001.

[41] S. Goeman and S. Boons, "First demonstration of highly reflective and highly polarization selective diffraction gratings (GIRO-gratings) for long-wavelength VCSELs," *IEEE Photonics Technology Letters*, vol. 10, no. 9, pp. 1205–1207, 1998.

[42] S. Goeman and B. Dhoedt, "Experimental demonstration of high TM reflectivity in GaAs based GIRO-gratings in the

wavelength region of 9-11 μm," *LEOS 1997 Annual Meeting, Conference Proc.*, vol. 1, pp. 13–14, 1997.

[43] F. L. Pedrotti and L. S. Pedrotti, *Introduction to Optics*. Prentice Hall, 1993, vol. 28.

[44] M. G. Moharam, D. a. Pommet, E. B. Grann, and T. K. Gaylord, "Formulation for stable and efficient implementation of the rigorous coupled-wave analysis of binary gratings," *Journal of the Optical Society of America A*, vol. 12, no. 5, p. 1068, May 1995.

[45] B. Dhoedt, D. Delbeke, L. Vanholme, and P. Bienstman, *RODIS user manual*, 1st ed., Ghent University.

[46] V. Karagodsky, F. G. Sedgwick, and C. J. Chang-Hasnain, "Theoretical analysis of subwavelength high contrast grating reflectors." *Optics Express*, vol. 18, no. 16, pp. 16 973–88, Aug. 2010.

[47] M. C. Huang, Y. Zhou, and C. J. Chang-Hasnain, "A surface-emitting laser incorporating a high-index-contrast subwavelength grating," *Nature Photonics*, vol. 1, no. 2, pp. 119–122, Feb. 2007.

[48] Y. Zhou, M. C. Y. Huang, and C. J. Chang-Hasnain, "Large Fabrication Tolerance for VCSELs Using High-Contrast Grating," *IEEE Photonics Technology Letters*, vol. 20, no. 6, pp. 434–436, Mar. 2008.

[49] W. Hofmann, C. Chase, M. Muller, C. Grasse, G. Bohm, M.-C. Amann, and C. J. Chang-Hasnain, "Long-Wavelength High-Contrast Grating Vertical-Cavity Surface-Emitting Laser," *IEEE Photonics Journal*, vol. 2, no. 3, pp. 415–422, Jun. 2010.

[50] M. Wu, G. Li, W. Yuen, and C. Chang-Hasnain, "Widely tunable 1.5 um micromechanical optical filter using AlOx/AlGaAs DBR," *Electronics Letters*, vol. 33, no. 20, p. 1702, Sep. 1997.

[51] M. H. MacDougal, P. D. Dapkus, A. E. Bond, and J. Geske, “Design and fabrication of VCSELs with AlxOy-GaAs DBRs,” *IEEE Journal of Selected Topics in Quantum Electronics*, vol. 3, no. 3, pp. 905–915, Jun. 1997.

[52] J. Daleiden, V. Rangelov, S. Irmer, and E. Romer, “Record tuning range of InP-based multiple air-gap MOEMS filter,” *Electronics Letters*, vol. 38, no. 21, pp. 1270–1271, 2002.

[53] R. Magnusson and M. Shokooh-Saremi, “Physical basis for wideband resonant reflectors,” *Optics Express*, vol. 16, no. 5, p. 3456, Mar. 2008.

[54] L. A. Coldren, *Diode lasers and photonic integrated circuits.* Wiley, 1995.

[55] E. F. Schubert and N. E. J. Hunt, “Enhancement of Spontaneous Emission in Microcavities,” in *Vertical-Cavity Surface-Emitting Lasers*, C. W. Wilmsen, H. Temkin, and L. A. Coldren, Eds. Cambridge University Press, 1999, pp. 68–107.

[56] P. Tayebati, P. D. Wang, D. Vakhshoori, and R. N. Sacks, “Widely tunable Fabry-Perot filter using Ga(Al)As-AlOx deformable mirrors,” *IEEE Photonics Technology Letters*, vol. 10, no. 3, pp. 394–396, Mar. 1998.

[57] E. C. Vail, M. S. Wu, G. S. Li, L. Eng, and C. J. Chang-Hasnain, “GaAs micromachined widely tunable Fabry-Perot filters,” *Electronics Letters*, vol. 31, no. 3, p. 228, Feb. 1995.

[58] R. L. Thornton, R. D. Burnham, and W. Streifer, “High reflectivity GaAs-AlGaAs mirrors fabricated by metalorganic chemical vapor deposition,” *Applied Physics Letters*, vol. 45, no. 10, p. 1028, Nov. 1984.

[59] E. Bisaillon, D. Tan, B. Faraji, A. Kirk, L. Chrowstowski, and D. V. Plant, “High reflectivity air-bridge subwavelength grating reflector and Fabry-Perot cavity in AlGaAs/GaAs.” *Optics Express*, vol. 14, no. 7, pp. 2573–82, Apr. 2006.

[60] Y. Rao, C. Chase, M. C. Y. Huang, S. Khaleghi, M. R. Chitgarha, M. Ziyadi, D. P. Worland, A. E. Willner, and C. J.

Chang-Hasnain, “Continuous Tunable 1550-nm High Contrast Grating VCSEL,” in *CLEO: Science and Innovations*, 2012, p. CTh5C.3.

[61] F. Sugihwo, M. Larson, and J. Harris Jr, “Micromachined widely tunable vertical cavity laser diodes,” *Microelectromechanical Systems, Journal of*, vol. 7, no. 1, pp. 48–55, 1998.

[62] K. D. Choquette, R. P. Schneider, K. L. Lear, and K. M. Geib, “Low threshold voltage vertical-cavity lasers fabricated by selective oxidation,” *Electronics Letters*, vol. 30, no. 24, p. 2043, Nov. 1994.

[63] D. L. Huffaker, D. G. Deppe, K. Kumar, and T. J. Rogers, “Native-oxide defined ring contact for low threshold vertical-cavity lasers,” *Applied Physics Letters*, vol. 65, no. 1, p. 97, Jul. 1994.

[64] P. Bienstman and R. Baets, “Rigorous and efficient optical VCSEL model based on vectorial eigenmode expansion and perfectly matched layers,” in *Optoelectronics, IEE Proceedings*, vol. 149, no. 4. IET, 2002, pp. 161–165.

[65] P. Bienstman, R. Baets, J. Vukusic, A. Larsson, M. Noble, M. Brunner, K. Gulden, P. Debernardi, L. Fratta, G. Bava, and Others, “Comparison of optical VCSEL models on the simulation of oxide-confined devices,” *Quantum Electronics, IEEE Journal of*, vol. 37, no. 12, pp. 1618–1631, 2001.

[66] P. Bienstman, *CAMFR manual*, 1st ed., September 2007. [Online]. Available: http://camfr.sourceforge.net

[67] Bienstman, P., “Rigorous and efficient modelling of wavelength scale photonic components,” Ph.D. dissertation, University of Gent, 2001.

[68] M. C. Larson, “Microelectromechanical wavelength-tunable vertical-cavity light-emitters and lasers,” PhD dissertation, Stanford University, 1996.

[69] S. D. Senturia, *Microsystem design.* Springer, 2001.

[70] G. D. Cole, J. E. Bowers, and K. L. Turner, “Dynamic characterization of MEMS-tunable vertical-cavity SOAs,” *IEEE/LEOS International Conference on Optical MEMS and Their Applications*, pp. 15–16, 2005.

[71] G. Woan, *The Cambridge handbook of physics formulas.* Cambridge University Press, 2003.

[72] O. Hansen, “Private communication,” 2012.

[73] T. K. Sharma, M. Zorn, U. Zeimer, H. Kissel, F. Bugge, and M. Weyers, “Highly strained InGaAs/GaAs quantum wells emitting beyond 1.2 \mu m,” *Crystal Research and Technology*, vol. 40, no. 9, pp. 877–881, Sep. 2005.

[74] P. Sundgren, J. Berggren, P. Goldman, and M. Hammar, “Highly strained InGaAs/GaAs multiple quantum-wells for laser applications in the 1200-1300 nm wavelength regime,” *Applied Physics Letters*, vol. 87, no. 7, p. 071104, 2005.

[75] Y. K. Su, W. C. Chen, C. T. Wan, H. C. Yu, R. W. Chuang, M. C. Tsai, K. Y. Cheng, C. Hu, and S. Tsau, “Optimization of the highly strained InGaAs/GaAs quantum well lasers grown by MOVPE,” *Journal of Crystal Growth*, vol. 310, no. 15, pp. 3615–3620, Jul. 2008.

[76] D. Schlenker, T. Miyamoto, Z. Chen, F. Koyama, and K. Iga, “Growth of highly strained GaInAs/GaAs quantum wells for 1.2 \mu m wavelength lasers,” *Journal of Crystal Growth*, vol. 209, no. 1, pp. 27–36, Jan. 2000.

[77] H. Q. Hou, K. D. Choquette, K. M. Geib, and B. E. Hammons, “High-performance 1.06-um selectively oxidized vertical-cavity surface-emitting lasers with InGaAs-GaAsP strain-compensated quantum wells,” *Photonics Technology Letters, IEEE*, vol. 9, no. 8, pp. 1057–1059, 1997.

[78] G. B. Stringfellow, *Organometallic Vapor-Phase Epitaxy: Theory and Practice.* Academic Press, 1998.

[79] J. W. Matthews and A. E. Blakeslee, “Defects in epitaxial multilayers: I. Misfit dislocations,” *Journal of Crystal Growth*, vol. 27, pp. 118–125, 1974.

[80] R. People and J. C. Bean, "Calculation of critical layer thickness versus lattice mismatch for GeSi/si strained-layer heterostructures," *Applied Physics Letters*, vol. 47, no. 3, pp. 322–324, 1985.

[81] F. Bugge, U. Zeimer, M. Sato, M. Weyers, and G. Tränkle, "MOVPE growth of highly strained InGaAs/GaAs quantum wells," *Journal of crystal growth*, vol. 183, no. 4, pp. 511–518, 1998.

[82] G. B. Stringfellow, "Miscibility gaps in quaternary III/V alloys," *Journal of Crystal Growth*, vol. 58, no. 1, pp. 194–202, 1982.

[83] K. Yvind, "Semiconductor Mode-Locked Lasers for Optical Communication Systems," Ph.D. dissertation, Technical University of Denmark, 2003.

[84] K. Choquette, K. Geib, C. Ashby, R. Twesten, O. Blum, H. Hou, D. Follstaedt, B. Hammons, D. Mathes, and R. Hull, "Advances in selective wet oxidation of AlGaAs alloys," *IEEE Journal of Selected Topics in Quantum Electronics*, vol. 3, no. 3, pp. 916–926, Jun. 1997.

[85] Y. Ohba and M. Ishikawa, "Growth of high-quality InGaAIP epilayers by MOCVD using methyl metalorganics and their application to visible semiconductors lasers," *Journal of Crystal Growth*, vol. 77, no. 1-3, pp. 374–379, 1986.

[86] S. Adachi, "GaAs, AlAs, and AlxGa1-xAs material parameters for use in research and device applications," *Journal of Applied Physics*, vol. 58, no. 3, pp. R1–R29, 1985.

[87] Hjort, Klas, "Sacrificial etching of III-V compounds for micromechanical devices," *Journal of Micromechanics and Microengineering*, vol. 6, p. 370, 1996.

[88] E. Yablonovitch, T. Gmitter, J. P. Harbison, and R. Bhat, "Extreme selectivity in the lift-off of epitaxial GaAs films," *Applied Physics Letters*, vol. 51, no. 26, pp. 2222–2224, 1987.

[89] M. J. Cich, J. A. Johnson, G. M. Peake, and O. B. Spahn, “Crystallographic dependence of the lateral undercut wet etching rate of InGaP in HCl,” *Applied Physics Letters*, vol. 82, no. 4, p. 651, 2003.

[90] J. R. Lothian, J. M. Kuo, and W. S. Hobson, “Wet and dry etching characteristics of Al0.5In0.5P,” *Journal of Vacuum Science and Technology*, vol. 10, no. 3, pp. 1061–1065, 1992.

[91] J. W. Lee, S. J. Pearton, C. R. Abernathy, W. S. Hobson, F. Ren, and C. S. Wu, “Wet Chemical Etching of AlInP,” *Journal of the Electrochemical Society*, vol. 142, no. 6, p. L100, 1995.

[92] J. R. Lothian, J. M. Kuo, F. Ren, S. J. Pearton, and M. Hill, “Plasma and Wet Chemical Etching of In0.5Ga0.5P,” *Journal of electronic materials*, vol. 21, no. 4, pp. 441–445, 1992.

[93] T. Kitano, S. Izumi, H. Minami, T. Ishikawa, K. Sato, T. Sonoda, and M. Otsubo, “Selective wet etching for highly uniform GaAs/Al0.15Ga0.85As heterostructure field effect transistors,” *Journal of Vacuum Science & Technology B: Microelectronics and Nanometer Structures*, vol. 15, no. 1, pp. 167–170, Aug. 1997.

[94] G. C. DeSalvo, “Etch Rates and Selectivities of Citric Acid/Hydrogen Peroxide on GaAs, Al0.3Ga0.7As, In0.2Ga0.8As, In0.53Ga0.47As, InAlAs, and InP,” *Journal of The Electrochemical Society*, vol. 139, no. 3, p. 831, 1992.

[95] J. H. Kim, “Selective etching of AlGaAs/GaAs structures using the solutions of citric acid/H2O2 and de-ionized H2O/buffered oxide etch,” *Journal of Vacuum Science and Technology B: Microelectronics and Nanometer Structures*, vol. 16, no. 2, pp. 558–560, 1998.

[96] M. Tong, D. G. Ballegeer, A. Ketterson, E. J. Roan, K. Y. Cheng, and I. Adesida, “A comparative study of wet and dry selective etching processes for GaAs/AIGaAs/lnGaAs pseudomorphic MODFETs,” *Journal of Electronic Materials*, vol. 21, no. 1, pp. 9–15, 1992.

[97] W. P. Dumke, J. M. Woodall, and V. L. Rideout, "GaAs—GaAlAs heterojunction transistor for high frequency operation," *Solid-State Electronics*, vol. 15, pp. 1339–1343, 1972.

[98] P. Kumar, S. Kanakaraju, and D. DeVoe, "Sacrificial etching of AlxGa1-xAs for III-V MEMS surface micromachining," *Applied Physics A*, vol. 88, no. 4, pp. 711–714, May 2007.

[99] Y. Uenishi, H. Tanaka, and H. Ukita, "Characterization of AlGaAs microstructure fabricated by AlGaAs/GaAs micromachining," *IEEE Transactions on Electron Devices*, vol. 41, pp. 1778–1783, 1994.

[100] H.-H. Wang, C.-J. Huang, Y.-H. Wang, and M.-P. Houng, "Liquid Phase Chemical-Enhanced Oxidation for GaAs Operated Near Room Temperature," *Japanese Journal of Applied Physics*, vol. 37, pp. L67–L70, Jan. 1998.

[101] M. Schubert, "Coupled Photonic Crystal Cavity Array Laser," Ph.D. dissertation, Technical University of Denmark, 2011.

[102] D. Larsson, "Fabrication and Characterisation of Low-noise Monolithic Mode-locked Lasers," Ph.D. dissertation, Technical University of Denmark, 2007.

[103] D. Lauvernier, S. Garidel, C. Legrand, and J. Vilcot, "Realization of sub-micron patterns on GaAs using a HSQ etching mask," *Microelectronic Engineering*, vol. 77, no. 3-4, pp. 210–216, 2005.

[104] C. I. H. Ashby and A. G. Baca, *Fabrication of GaAs devices*, 1st ed. The Institution of Electrical Engineers, September 2005.

[105] W. Y. Han, Y. Lu, H. S. Lee, M. W. Cole, L. M. Casas, A. Deanni, K. A. Jones, and L. W. Yang, "Shallow ohmic contact to both n- and p-GaAs," *Journal of Applied Physics*, vol. 74, no. 1, pp. 754–756, 1993.

[106] M. C. Larson, B. Pezeshki, and J. S. Harris, "Vertical coupled-cavity microinterferometer on GaAs with

deformable-membrane top mirror," *IEEE Photonics Technology Letters*, vol. 7, no. 4, pp. 382–384, Apr. 1995.

[107] T. Stomeo, M. Grande, G. Rainò, A. Passaseo, A. D'Orazio, R. Cingolani, A. Locatelli, D. Modotto, C. De Angelis, and M. De Vittorio, "Optical filter based on two coupled PhC GaAs-membranes." *Optics letters*, vol. 35, no. 3, pp. 411–3, Feb. 2010.

[108] E. Bisaillon, D. T. H. Tan, B. Faraji, Y. Zeng, C. Ostafew, R. Krishna-Prasad, L. Chrowstowski, and D. V. Plant, "Resonant Grating Based Fabry-Perot Cavity in AlGaAs/GaAs," in *Lasers and Electro-Optics Society (LEOS) 2006. 19th Annual Meeting of the IEEE*, 2006, pp. 817–818.

[109] S. Boutami, B. Ben Bakir, J.-L. Leclercq, X. Letartre, P. Rojo-Romeo, M. Garrigues, P. Viktorovitch, I. Sagnes, L. Legratiet, and M. Strassner, "Highly selective and compact tunable MOEMS photonic crystal Fabry-Perot filter." *Optics Express*, vol. 14, no. 8, pp. 3129–37, Apr. 2006.

[110] P. Gilet, N. Olivier, P. Grosse, K. Gilbert, A. Chelnokov, I.-S. Chung, and J. Mø rk, "High-index-contrast subwavelength grating VCSEL," in *Proceedings of SPIE*, vol. 7615, 2010, pp. 76 150J–76 150J–8.

DTU

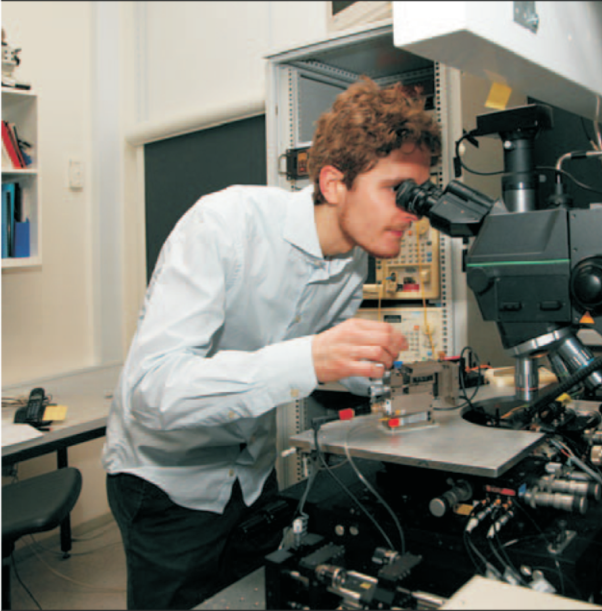

Copyright: Thor Ansbæk
and DTU Fotonik
All rights reserved
ISBN: 978-87-93089-09-9

Published by:
DTU Fotonik
Department of Photonics Engineering
Technical University of Denmark
Ørsteds Plads, building 343
DK-2800 Kgs. Lyngby

Thor Ansbæk received his M.Sc. Eng. in 2008 and Ph.D. in 2012 at The Technical University of Denmark (DTU). During his undergraduate studies he took part in research on Micro-Electro-Mechanical Systems (MEMS) at DTU Nanotech under the supervision of Erik V. Thomsen and Ole Hansen. During his graduate studies at DTU Fotonik he worked on vertical-cavity surface-emitting lasers (VCSELs) for medical diagnostics under the supervision of Kresten Yvind. The study was focused on III-V semiconductor technology and resulted in the fabrication of MEMS Fabry-Pérot filters and VCSELs.